

Use Authorization

In presenting this dissertation in partial fulfillment of the requirements for an advanced degree at Idaho State University, I agree that the Library shall make it freely available for inspection. I further state that permission to download and/or print my dissertation for scholarly purposes may be granted by the Dean of the Graduate School, Dean of my academic division, or by the University Librarian. It is understood that any copying or publication of this dissertation for financial gain shall not be allowed without my written permission.

Signature:

Date:

TriMeV Radiography: The effects of diode parameters on dose
and source spot size

by

David Housley

A thesis

submitted in partial fulfillment

of the requirements for the degree of

Master of Science in the Department of Physics, Nuclear, & Electrical Engineering

Idaho State University

December 2018

Copyright ©2018 David Housley

All rights reserved. No part of this thesis may be reproduced in any form or by any electronic or mechanical means, including information storage and retrieval systems, without written permission from the author or as granted by the Dean of the Graduate School, Dean of my academic division, or by the University Librarian.

To the Graduate Faculty:

The members of the committee appointed to examine the thesis of David Housley find it satisfactory and recommend that it be accepted.

Dr. Rick SPIELMAN,
Major Advisor

Dr. George IMEL,
Committee Member

Dr. DeWayne DERRYBERRY,
Graduate Faculty Representative

To my patient wife Evva

and

*to my most enthusiastic supporters
Lauren and Rachel.*

My profound thanks to:

Dr. Rick SPIELMAN

who has been not only generous and encouraging but very kind,

Dr. George IMEL

for his insight and prudence which he has so graciously shared,

All at the Idaho Accelerator Center

for their stamina in support of the TriMeV system,

and

Sandia National Labs

in offering their kind and benevolent support.

Table of Contents

List of Figures	x
List of Tables	xiii
Abbreviations	xiv
Physical Constants	xv
Symbols	xvi
Abstract	xvii
1 Introduction	1
1.1 Flash radiography overview	1
1.1.1 History	1
1.1.2 applications	2
1.2 TriMeV anatomy	2
1.3 Theory	3
1.3.1 Diode concepts	4
1.3.1.1 Background	4
1.4 Operational descriptions	5
1.4.1 Shot variation and qualification	5
1.4.2 Simulation	5
1.5 System pathologies	5
1.6 Methods	5
1.7 Cathode sleeve	6
1.8 Anode shroud	6
1.9 Anode field enhancements	6
1.10 Objectives	7
2 TriMeV Anatomy	8
2.1 System layout	8
2.1.1 Trigger system	9
2.1.2 Marx generator	9
2.1.3 Pulse-forming line	10
2.1.4 Output switch	10
2.1.5 Output transmission line	10
2.1.6 Sharpening switch	11
2.1.7 Oil transmission line	11
2.1.8 Water wedge	11
2.1.9 Vacuum insulator	11
2.1.10 Vacuum transmission line	12
3 Theory	13
3.1 Electric charges and interactions	13

3.1.1	Bremsstrahlung radiation	13
3.1.2	Photon Attenuation and Transmission	15
3.1.3	Lorentz force law	16
3.1.4	Bennett equilibrium	18
3.2	Figure of merit	21
3.3	Component characterization	22
3.3.1	Impedance	22
4	Operational description	25
4.1	Circuit simulation	25
4.2	Circuitry modeling	26
4.2.1	Screamer model	26
5	Pathologies	29
5.1	A-K gap variations	29
5.2	TriMeV installations	29
5.3	Missing parts	31
5.3.1	Data acquisition system	31
5.3.2	Pump pallet	31
5.3.3	Hydraulic system support tray	31
5.4	TG 80 discharge	31
5.5	Output resistor	32
5.6	Insulator tracking	32
5.7	Log book centralization	33
5.8	Converter mounting	33
5.9	System Trigger	33
5.10	Marx resistor replacements	34
5.11	Oil fouling	34
5.12	Grading ring creep	35
5.13	Trigger timing	35
5.14	Output Switch D-dot	36
5.15	Scope trigger and timing	36
5.16	Landauer OSLD system	36
5.16.1	Condition of the dosimeters	37
5.16.2	Calibration of the OSLD system	37
5.16.3	Repeated readings and fade over time	38
5.17	Denoptix QST scanner	38
5.17.1	Data preconditioning	38
5.17.2	Drivers	39
5.18	Anode ablation and cathode tip wear	39
5.18.1	Cathode tip preconditioning	39
6	Methods	41
6.1	Spot size measurement	41
6.1.1	Tungsten rolled edge	41
6.1.2	Face plate contact film	43
6.2	Dose measurements	43

Table of Contents

6.2.1	Optically Stimulated Luminescence (OSL)	43
6.2.2	PIN diode	44
6.2.2.1	Calibration of PIN diodes	44
6.3	X-ray spectrum	46
6.4	Current diagnostics	47
6.4.1	B-dot	47
6.5	Electron beam diode voltage	47
6.5.1	D-dot	47
7	Cathode sleeve experiment	49
7.1	Cathode sleeve effects on the electron beam	50
7.2	Cathode sleeve effects on the spot size	50
7.3	Conclusions on the spot diameter as a function of reveal	52
7.4	Dose effects	53
7.5	Effect on figure of merit	55
8	Anode shroud experiment	57
8.1	Anode shroud effects on the electron beam	57
8.2	Planar anode shroud experiments	58
8.2.1	Effect on the spot size	58
8.2.2	Suggestions from the spot diameter	58
8.2.3	Planar shroud dose effects	60
8.2.4	Effect on figure of merit	61
9	Anode field enhancements	63
9.1	Anode field enhancement effects on the electron beam	63
9.2	Anode field enhancement experiments	64
9.2.1	Effect on the spot size	64
9.2.2	Suggestions from the spot diameter	64
9.2.3	Anode field enhancement dose effects	65
9.2.4	Effect on figure of merit	65
10	Conclusion	69
10.1	Performance Summary	69
10.2	Future work	70
10.2.1	Sleeve and shroud combined diode	70
10.2.2	Cathode sleeve effects	70
10.2.3	Anode field enhancements	71
10.2.4	Silicon diode arrays	71
10.2.5	Perpendicular rolled edges	72
10.2.6	Flat field radiographs	72
10.2.6.1	Flat fielding method	72
10.2.6.2	Radiographic source collimator	72
10.2.6.3	Shielding	73
10.2.7	Rogowski coils	73
10.2.8	Transmission line gas switching	73
10.2.9	Plasma diagnostics	74
10.2.10	Spectrum determination	74

10.2.10.1 Dose depth profile	74
10.2.10.2 Laser Compton scattering	74
10.2.10.3 Geant4 simulations	74
10.2.10.4 Diode voltage and current estimations	75
10.2.10.5 Aluminum test wedge	75
10.2.11 Summary	75
Bibliography	76
A Screamer	80
A.1 Introduction	80
A.2 Motivation	81
A.3 Installation notes	81
A.3.1 Windows	82
A.3.2 Linux	82
A.4 Code	84
A.4.1 Run Deck For Simplified TriMeV Screamer Simulation	84
B OSL calibration	88
B.1 Introduction	88
B.1.1 Dosimeter preparation	91
B.2 Calibration Procedure	93
B.3 Validation	94
C Solid state diode calibration	95
C.1 Introduction	95
C.2 Method	95
C.3 Signal Processing	96
D Stella	97
D.1 Introduction	97
D.2 Motivation	97
D.3 Installation notes	97
D.4 Macros	98
E BAS 1800 II	99
E.1 Introduction	99
E.2 Installation notes	99
E.3 Operation notes	99
E.3.1 Procedural description for BAS-1800 II scanner	99
F Denoptix	102
F.1 Introduction	102
F.2 Installation notes	102
F.3 Operational notes	102

List of Figures

1.1	This figure diagrams the canonical flash x-radiography experimental setup. From left to right the conversion of electrons results in an x-ray pulse which is cast upon a French test object (FTO). Those photons transmitted are detected on the right. The FTO contains a tungsten shell (inner radius = 1 cm and outer radius = 4.5 cm) inside a copper shell (outer radius = 6.5 cm) inside a foam shell (outer radius = 22.5 cm). Note, the sharpness of shadow edges cast upon the detector are limited by both the finite extent of the x-ray source and the inherent spacial precision with which the detector can sense photons[1].	3
1.2	Schematic diagramming Bremsstrahlung conversion of a beam electron to an x-ray photon.	4
2.1	Horizontal cross section of TriMeV accelerator showing locations of B-dot and D-dot monitors (not to scale).	8
3.1	Charge Q in the presence of a current carrying wire in the lab frame (left) and the charge Q frame (right). Notice the concentration of the negative charge carriers in the charge Q frame due to length contraction.	16
3.2	Plasma z-pinch geometry	18
4.1	Data from shot 194 for all the voltage and current diagnostic channels along the pulse line of the TriMeV system showing leaders.	25
4.2	Data from shot 194 and simulation results of voltage at the output switch.	27
4.3	Data from shot 194 and simulation results of voltage at the sharpening switch.	27
4.4	Simplified TriMeV circuit model showing the quantified components with the TriMeV parts labeled.	28
5.1	TriMeV layouts	30
6.1	Schematic diagramming rolled edge set up.	41
6.2	Radiographs showing rolled edge images from Shot 154 using FujiFilm BAS 1800II (left) and Denoptix QST (right) phosphor screen imaging systems.	42
6.3	Voltage (measured), current (measured), and impedance (calculated from voltage and current) of the diode for the duration of shot 87.	44
6.4	Silicon PIN diode signal evolution throughout the calibration process (shot 87 shown).	45
6.5	Scematic of the PIN diode set up to ensure operating voltage.	45
6.6	Stella macro detail for PIN diode data processing.	46
7.1	Sketch of expected electron and ion plasma for a SMP diode late in the shot after the diode has shorted out from the ion plume closing the A-K gap. The general shape of the electron beam is patterned from current distributions from PIC simulations in literature [2].	49

7.2	Sketch of hypothesized electron beam and plasmas for a SMP diode with a negative-reveal sleeve early in the shot before the plasma has shorted the diode.	51
7.3	Spot size and cathode sleeve reveal by shot number.	51
7.4	Dose and cathode sleeve reveal vs shot number.	54
7.5	Figure of merit as calculated from OSL measured dose (squares) and from PIN T signal (open circles) and cathode sleeve reveal (triangles) by shot number. Here FOM is read from the left scale and the reveal from the right.	56
8.1	Sketch of planar anode shroud showing electron beam and expanding plasma for a 1 inch aluminum ring diode.	57
8.2	Spot size and shroud aperture diameter vs shot number.	58
8.3	Dose and anode shroud aperture diameter as a function of shot number.	60
8.4	Figure of merit as calculated from OSL measured dose (squares), PIN 43 signal (circles), and PIN 44 output (down pointing triangles) with the planar anode shroud bore diameter (up pointing triangles) by shot number. I have used the LSF FWHM description of the spot size and FOM is read from the left scale and the shroud bore diameter from the right.	61
9.1	Sketch of the diode featuring an anode pin to induce field enhancements at the anode.	64
9.2	Spot size as a function of shot number for the anode field enhancement shots.	65
9.3	Dose with respect to shot number for the anode field enhancement experiments.	66
9.4	Figure of merit as calculated from OSL measured dose with anode field enhancements by shot number. The LSF FWHM description of the spot size was used.	66
9.5	Diode current by shot as measured by a B-dot embedded in the vacuum chamber wall. Shot 141 included for comparison.	67
9.6	Diode voltage by shot as measured by a D-dot embedded in the vacuum chamber wall. Shot 141 included for comparison.	68
A.1	Two screamer elements connected in series [3].	80
B.1	Landauer's dot adapter cassette and dot dosimeter (with Al ₂ O ₃ :C embedded disk concealed and exposed).	88
B.2	The OSL mechanisms that enable the measurement of exposure. Exposure involves the separation and promotion of the electron to the conduction band where it moves freely throughout the crystal until being captured by a crystal defect leaving the electron in a higher energy state (a). The long lifetime of the captured electrons allows a "memory" of the exposure (b). Optical stimulation of the electron promotes the electron back to the conduction band where there exists a probability that the electron will recombine with the hole left during exposure (c).	89
B.3	20 Ci Shepherd source documentation.	91

E.1	Lifted lid of the BAS-1800II image plate reader exposing the solenoids that actuate the stimulation laser baffle.	100
E.2	Splash screen for Image Reader software.	101

List of Tables

7.1	Statistics calculated on the LSF FWHM spot diameter vs reveal (P) for the cathode sleeve experiments.	52
7.2	Statistics calculated on the dose measured on axis at 1 meter from the source, as inferred from PIN 43, as a function of reveal (P) for the cathode sleeve experiments.	54
7.3	Statistics calculated on the FOM calculated from dose, as inferred from PIN 43, and the LSF FWHM spot diameter for the cathode sleeve experiments.	56
8.1	Statistics calculated on the LSF FWHM spot diameter for the anode shroud experiments.	59
8.2	Statistics calculated on the dose measured on axis at 1 meter from the source for the planar anode shroud experiments. Shot 102 PIN diode measurements classified as outliers (O) and not included in statistics. . . .	61
8.3	Statistics calculated on the FOM for the anode shroud experiments. The PIN diode determined dose data from shot 102 is a suspect outlier (O). To exclude it from the mean and standard deviation calculations only the OSL based data has been used.	62
9.1	Shot and A-K gap width for anode field enhancement experiments. . . .	67
B.1	Activities of the 20 Ci source based upon the numbers reported by Shepherd and associates.	92
B.2	Dosimeter sets prepared for calibration of MicroStar reader.	93
B.3	Calibrate readings for validation of the microStar reader.	94

Abbreviations

A-K	Anode - cathode
CD	Compact Disk
CPU	Central Processing Unit
FOM	Figure Of Merit
GB	Giga Bytes
IAC	Idaho Accelerator Center
IP	Image Plate
ISU	Idaho State University
OSLD	Optically Stimulated Luminescence Dosimeter
OSL	Optically Stimulated Luminescence
PC	Personal Computer
PFL	Pulse Forming Line
PIN	P-type Intrinsic N-type
RAM	Random Access Memory
RL	Radio Luminescence
SF6	Sulfer hexaFloride
SMP	Self Magnetically Pinched
TL	Thermo Luminescence
TL	Transmission Line
USB	Universal Serial Buss
FTO	French Test Object
IAC	Idaho Accelerator Center
SLIA	Spiral Line Induction Accelerator
CERN	Conseil Européen pour la Recherche Nucléaire
LSF	Line Spread Function
EMF	Electo Motive Force
FWHM	Full Width Half Maximum
ESF	Edge Spread Function
EDM	Electric Discharge Machining
TL	Transmission Line

Physical Constants

Speed of Light	c	$=$	$2.997 \times 10^8 \text{ ms}^{-1}$
Elementary Charge	e	$=$	$1.6022 \times 10^{-19} \text{ C}$
Permeability of Free Space	μ_0	$=$	$4\pi \times 10^{-7} \text{ Hm}^{-1}$
Permittivity of Free Space	ϵ_0	$=$	$8.8542 \times 10^{-12} \text{ Fm}^{-1}$

Symbols

S	Poynting vector	Wm^{-2}
E	electric field	N/C (V/m)
B	magnetic field	T
n	normal unit vector	
<i>P</i>	power	$\text{W (Js}^{-1}\text{)}$
<i>P</i>	probability	
<i>P</i>	pressure	Nm^{-2}
v	velocity vector	ms^{-1}
<i>A</i>	area	m^2
<i>I</i>	current	A
F	force vector	N
<i>q</i> or <i>Q</i>	charge	C
J	current density	Am^{-2}
<i>D</i>	dose	rad in air
<i>Z</i>	impedance	Ω
<i>V</i>	voltage	V
<i>U</i>	energy	joule

TriMeV Radiography: The effects of diode parameters on dose
and source spot size

Thesis Abstract - Idaho State University (2018)

Flash radiography continues to be valuable in investigating compression under explosive force where brightness, small source size, and short time duration must be maintained. The TriMeV pulsed electron accelerator delivers 30 kA at 3 MV over a 20 ns time window. In order to maximize brightness and minimize source size the treatment of the electron beam must be considered. Emitted from a cathode tip, the electrons accelerate across the anode-cathode (A-K) gap while ion plumes and electric and magnetic fields focus the beam onto a converter where Bremsstrahlung is produced.

A description of the system and a model for TriMeV circuitry is presented including a comparison of simulation and experimental measurements. Multiple methods for spot size and dose are described and recommendations made to improve and expand the characterization of this radiography source. The figure of merit (FOM) is calculated and represents a gauge of the potential of the system to produce a quality radiograph.

The presence of a cathode sleeve and anode shroud tune the focus of the beam by perturbing fields and conditioning ion plumes in the A-K gap. The cathode sleeve appears to collimate the beam and produces more reliable spot sizes shot to shot but reduces the FOM from 15.8 ± 0.8 rad @ $1\text{m}/\text{mm}^2$ for shots without a cathode sleeve to 5.4 ± 0.2 rad @ $1\text{m}/\text{mm}^2$ with a sleeve. With an anode shroud we noted a 2/3 reduction in output dose but little change in dose for a smaller shroud aperture. Compared to source spots observed without a shroud, the diameter was reduced to 1/3 for similar anode shroud bore/cathode tip diameters and to 1/4 when the anode shroud bore diameter was half that of the cathode tip. The FOM improved from 4.58 ± 0.26 rad @ $1\text{m}/\text{mm}^2$ for no shroud shots to 5.42 ± 0.37 rad @ $1\text{m}/\text{mm}^2$ for 25.4 mm shroud bore and further to 13.7 ± 1.32 rad @ $1\text{m}/\text{mm}^2$ for shots with shroud bore of 12.7 mm. Additionally, with the anode field enhancements we noted an average spot diameter of 0.73 mm \pm 0.1 mm and an average FOM of 114 rad @ 1 m/ mm^2 (std. deviation: 86.7 rad @ 1 m/ mm^2).

Key words: flash radiography, TriMeV, pulsed power, electron beam diode, figure of merit

Chapter 1

Introduction

1.1 Flash radiography overview

1.1.1 History

During the Manhattan Project it was theorized that plutonium (Pu) would give a more efficient explosion than uranium (U). In addition, plutonium has a larger cross section for prompt neutrons and a higher neutron yield per fission equating to a smaller critical mass. Reactor-produced plutonium generated a byproduct isotope that resulted in a high neutron background. The gun type designs used for uranium fueled devices could not bring the plutonium fuel together quickly enough given the elevated neutron background since the background would cause initiation of the nuclear cascade too early and blow the fuel apart prematurely for optimal energy yield. Only a radial implosion was fast enough to assemble the plutonium mass, so it was crucial to understand methods of radial implosion sufficient to execute it successfully. They needed a way to observe exactly what was happening during the detonation of the explosives driving the radial implosion to be certain the compression would provide optimal yield.

For the project Oppenheimer procured a betatron capable of 1-ms-long pulses of 15 MeV electrons. These pulses of electrons were incident upon a high-Z target, and the resulting high-energy photons effectively penetrated that high explosive portion of the device but were significantly attenuated by the core of the surrogate mock-up they were testing. So in the radiograph a "shadow" resulting from the core was observed, and the outer contour could be readily defined allowing quantification of the implosion given the appropriate timing of the flash.

John von Neumann's idea was that a solid core under sufficient implosion force (high explosives) would behave in a fluid manner, not as a solid material. With this assumption partial differential equations describe the implosion enabling an estimate of the velocity of implosion. Flash radiography provides a diagnostic that allows an investigator to quantify the elements of the partial differential equations needed to describe the implosion. The development of implosion had many challenges, particularly due to the shock waves of explosives combining, creating instabilities which resulted in uneven compression of the core. It was suspected that this focusing of compression caused jets to flare from the core. These jets were confirmed by flash radiography techniques. Instead of using conventional explosions, they developed a way to make explosive "lenses",

which shaped the compression waves so as to minimize pressure inconsistencies. Also by flash radiography techniques they found that the homogeneous nature of density in the explosives was crucial as well as the timing of all detonations [1].

1.1.2 applications

Flash radiography uses x rays in the same manner that photography uses strobe lights. The purpose is to take stop-action pictures of subjects, which due to their motion, allow only blurred images when using conventional radiographic illumination. This means a flash radiography source must be discrete in the time domain (18 ns in this case) so as to minimize the motional blur in the radiograph. Among the quintessential subjects in flash radiography is an object under explosive compression[1, 4, 5], see figure 1.1 for a similar experimental mockup. For instance, scientists can study the effects on fuel compression if a redesign of a component is necessary and certify the change will not alter the reliability of the device. In this way flash radiography is crucial to ensure the reliability of these devices into the future. This requires x-raying the effects of implosion on a mock/surrogate core. Such implosions are driven by conventional explosives whose action can only be observed on the time scale of 10's of nanoseconds. Thus, flash radiography allows the stewards of the stockpile to obtain information requisite to certification of re-manufactured parts and maintaining the stockpile without a underground testing of nuclear weapons.

1.2 TriMeV anatomy

TriMeV is a Marx generator driven pulsed-power electron accelerator and is designed to deliver a 3-MV peak-voltage pulse having a rise time of 3 ns and a duration of 18 ns and a 30-kA peak current [6–8]. The machine consists of a Marx generator fed transmission line which includes pulse conditioning switches and feeds through a water wedge that separates oil-bathed and vacuum environments. The electron beam diode hardware and the time isolation pulse line exist in the vacuum environment. The diode hardware that terminates the vacuum transmission line is designed to promote electron emission. Electrons are ejected from the cathode and are accelerated in the A-K gap. Emitted electrons are accelerated by the voltage differential toward the grounded plane where a high-Z converter is mounted to the grounded frame and the electrons are deflected by the high-Z nuclei. This acceleration/deflection results in a reduction of kinetic energy in the electrons, and emitted photons carry away the balance of the energy possessed by the originally accelerated electrons. This deflection that results in the loss of electron kinetic energy has been coined as Bremsstrahlung or "braking radiation" (see figure 1.2).

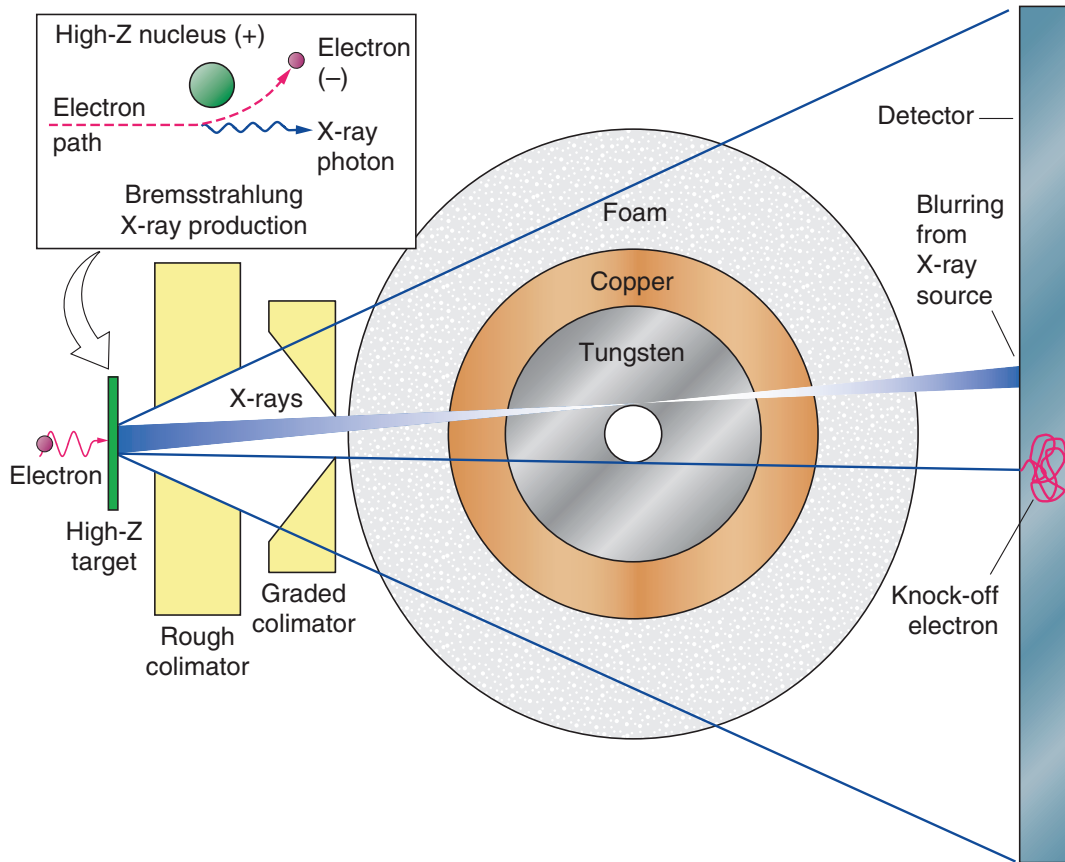


FIGURE 1.1: This figure diagrams the canonical flash x-radiography experimental setup. From left to right the conversion of electrons results in an x-ray pulse which is cast upon a French test object (FTO). Those photons transmitted are detected on the right. The FTO contains a tungsten shell (inner radius = 1 cm and outer radius = 4.5 cm) inside a copper shell (outer radius = 6.5 cm) inside a foam shell (outer radius = 22.5 cm). Note, the sharpness of shadow edges cast upon the detector are limited by both the finite extent of the x-ray source and the inherent spacial precision with which the detector can sense photons[1].

In the system the path of the electrons from cathode to anode is bridged by diode hardware. The design of this hardware will condition the electron beam and thereby affect the radiographic source where the beam interacts with the converter.

1.3 Theory

For the operation of an electron beam diode one must consider the charged particles involved and how they interact with their environment. The fact that you can get a photon by changing the acceleration of an electron is how TriMeV can be configured as a radiographic source. With this configuration the diode produces an electron beam incident on a converter so by Brehmsstrahlung the electron beam is converted into a

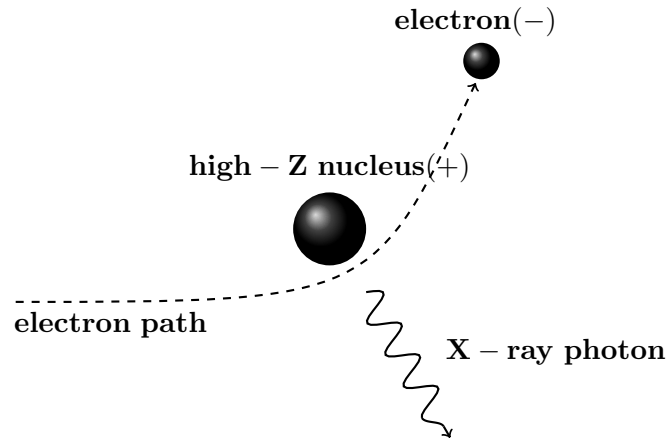


FIGURE 1.2: Schematic diagramming Bremsstrahlung conversion of a beam electron to an x-ray photon.

radiographic source. To understand the radiographic image it is important to consider the way a radiographic subject will attenuate the x-ray photons. The focus of the electron beam within the diode bears upon the size of the radiographic spot. This focus can be influenced by the presence of ions in the A-K gap and is subject to forces described by the Lorentz force law as exhibited in the Bennett equilibrium. Our motivation is to increase the quality of radiographs that the TriMeV system can produce. One way to judge quality is through the figure of merit and our approach focuses on reducing the radiographic spot size to increase the figure of merit and thus the image quality potential of the system.

1.3.1 Diode concepts

The varied design parameters throughout experiments in this thesis were chosen based upon their expected effect on the shape of the electron beam by influencing electric field geometries in the space between the anode and cathode (A-K gap) and/or the shape of the ion plume in the gap.

1.3.1.1 Background

Literature suggests [9–15] that the electron beam in the A-K gap will generate a plasma that expands from the anode and cathode surfaces. The formation of these two plasmas appear to be unavoidable. The plasma is thought to affect the electron beam in the A-K gap by increasing the current in the diode and by reducing the number of high energy electrons incident on the anode. When ions are introduced into the gap they accelerate across the gap due to the voltage differential and their charge.

1.4 Operational descriptions

1.4.1 Shot variation and qualification

We observe variations between shots with the TriMeV system which makes it difficult to make clear comparisons from one shot to another. One reason for the variable nature of shots are the self-closing switches that vary in impedance, inductance and timing with each closure.

The qualification of shots can be judged in different ways. When possible, dose and spot size measurements will be used to qualify the shots. Alternatively, literature suggests[16] that impedance of the e-beam diode can be influenced by the focus and wandering character of the electron beam over the life of the shot and thereby indicate quality in terms of spot size.

1.4.2 Simulation

I attempt to quantify the noise of the system by collecting data without any signal. Next I compute the R^2 value between the noise collected and a flat base line in an effort to predict the R^2 value for a perfect fit of the signal. Then I present a model for TriMeV and simulate that model in Screamer and compare the simulation result to experimental diagnostic signals.

1.5 System pathologies

Due to the complexity and number of the subsystems of TriMeV, there is an increased probability and possibility of failure pathways. The pathologies chapter in this thesis will attempt to catalog the most salient difficulties, along with actual and suggested remedies.

1.6 Methods

Spot size measurements were critical to this thesis. Spot sizes were measured using a pin-hole camera, a tungsten rolled edge, or a Rolland hole. For the pin-hole camera we define the spot diameter as the full width half maximum of the distribution of the grayscale (dependent on the dose density received on the image plane) found in the radiographic image. For the tungsten rolled edge and the Rolland hole, the diameter of the

spot is defined as either the 25%-75% rise in the edge spread function or the full width half maximum of the line spread function both derived from the radiograph.

Dose at one meter on axis is measured when possible by optically stimulated luminescence dosimeters (OSLD) and silicon PIN diodes.

It is necessary to have a clear picture of the diode in terms of voltage and current in order to understand and quantify the behavior of TriMeV. The current of the TriMeV system is monitored using B-dot instruments, while the voltage is monitored by D-dot instruments within the frame of the machine.

1.7 Cathode sleeve

One purpose of the experiments with TriMeV was to see if a cathode sleeve would have a desirable effect on spot size. Although more experiments are needed to characterize shot to shot variation with the cathode sleeve, the experiments that were performed suggest that a negative reveal between 0 mm and $-9.5 \text{ mm} \pm 0.1 \text{ mm}$ effectively reduces the shot to shot variation in spot size.

Dose data suggests the sleeve acts to reduce the dose on axis overall but there is a range of reveal between 1.59 mm and $-6.38 \text{ mm} \pm 0.1 \text{ mm}$ that optimizes the dose.

1.8 Anode shroud

One intent of the experiments with TriMeV was to see if an anode shroud would have a desirable effect on spot size. As suspected placing an insulative shroud over the converter reduced the spot size. However the change in spot size is not proportionate to the change in shroud bore suggesting that the ultimate driver in electron beam constriction cannot be the size of the bore alone but rather a combination of the bore size and a plasma expanding from the surface of the shroud. The constituents of these plasmas depends upon the composition of the shroud.

1.9 Anode field enhancements

We wanted to investigate the effect of an anode pin on the source spot diameter and the dose for shots on TriMeV. We expected the pin to enhance the initial focus of the electron beam to one location on the anode (within the diameter of the anode pin). The

smallest known spot diameters observed with the TriMeV system result from this diode. The spot sizes in this experimental series range from 0.88 to 0.51 ± 0.06 mm compared to the smallest previously published spot size of 0.8 mm [6] from the TriMeV system.

1.10 Objectives

The purpose of this work is to substantiate or falsify the claim that the size of the radiographic source spot produced with the TriMeV system can be reduced by the implementation of a cathode sleeve, an anode shroud, or an anode pin in such a way as to increase the system's potential to create a better quality image. Also that the constriction of the converter arsear illuminated by the electron beam is affected not directly by the bores in the sleeve or shroud but rather by the ion plume that is blown off of these surfaces.

In support of this thesis the reader will also find:

1. Information to familiarize them with the TriMeV system holistically which will include a description of its operation both theoretically and experimentally as well as identify operational problems and suggest solutions.
2. A model and simulations of the circuitry of the system that will enable better understanding of the system, provide a test bed for future alterations to the system, and allow a comparison between theory and experiment.
3. Observations regarding how the dose and spot size are effected by changes in the electron beam diode including variations in the existence and position of a poly cathode sleeve, the shape and presence of a anode shroud, and anode field enhancements.

Chapter 2

TriMeV Anatomy

2.1 System layout

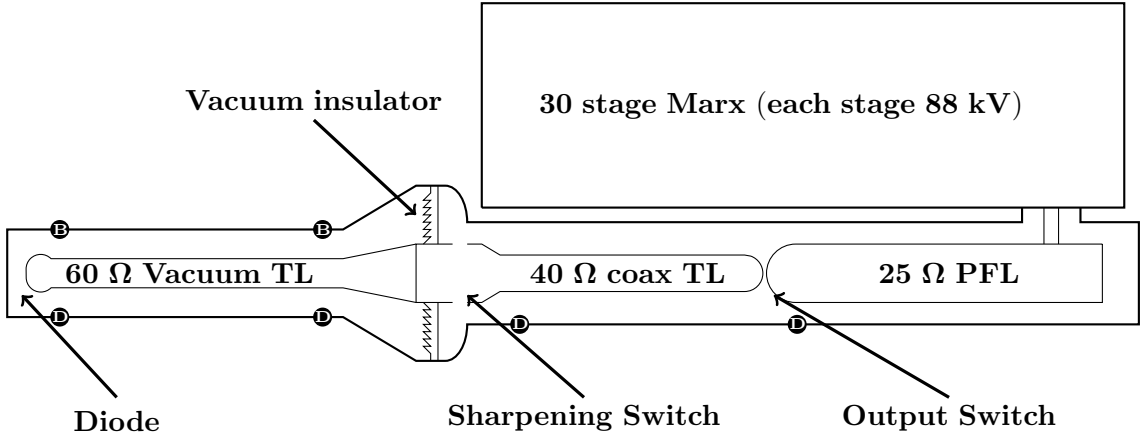


FIGURE 2.1: Horizontal cross section of TriMeV accelerator showing locations of B-dot and D-dot monitors (not to scale).

Operationally the system starts with a series of capacitors charged in parallel, all separated from a series configuration by a set of gas switches (known as the Marx generator). Once the capacitors are fully charged (44 kV), the system is triggered by operator interaction at the control panel. The depression of the fire button triggers the closure of the gas switches in the Marx generator, which erects the Marx (configures the capacitors in a series arrangement) such that the output of the Marx generator is elevated to the addition of all the voltage housed in the capacitors of the Marx system. This voltage pulse travels out of the Marx through a connecting resistor (5.5Ω) into a $25\text{-}\Omega$ pulse-forming line (PFL) charging the PFL in a time scale of 250 ns. The voltage self-breaks the output switch (an arc through oil) to the $40\text{-}\Omega$ coaxial line and is conveyed to the sharpening switch, which also self-closes (arc through oil) allowing the voltage pulse to pass through a feed which traverses a water-wedge insulator that separates the oil environment from the vacuum environment. The signal continues down the vacuum transmission line at an impedance of 60Ω . The voltage pulse then drives explosive emission of electrons from the cathode tip after it has traversed the length of the vacuum line. Electrons ejected into the gap accelerate due to voltage differential across the gap and impinge upon the configured anode (the grounded frame of the vacuum chamber).

Diagnostic monitors are positioned immediately preceding the output and sharpening switches, immediately following the taper of the vacuum transmission line, and immediately preceding the diode. Each of these monitoring positions includes a D-dot device that provides voltage information of the pulse line at that location. Additionally, the two monitoring positions in the vacuum environment (at the taper of the vacuum and preceding the diode) include B-dot monitors that provide current information at those locations.

2.1.1 Trigger system

The trigger system bridges the gap between the operator initiating the shot and the erection of the Marx generator. Additionally the trigger system arranges timing of the closure of the switches in the generator to manage the shape (rise time) of the voltage pulse out of the Marx generator.

Functionally the trigger sequence of the TriMeV system begins with the manual depression of a fire button at the operator console. This button activates an EMC100 to produce a 100-V signal which is conveyed into the box on top of the Marx tank and triggers the Pacific Atlantic Technologies PT-55 trigger generator which is charged during the charging sequence preceding the fire sequence. The output of the PT-55 is monitored as a diagnostic and triggers the TG-80. The output here is also monitored to illuminate any trigger system malfunction. The TG-80 signal is divided quadripartite and travels through four time isolated cables to trigger the switches erecting the Marx generator.

2.1.2 Marx generator

The Marx generator consists of 60 stages each containing seven 32-nF capacitors that are connected in parallel via the charging resistors which connect the capacitors to the high voltage power source that charges the capacitors during the charging sequence preceding the fire sequence. Each stage is connected in series through a collection of 29 pressurized SF6 gas switches which, when closed, arrange the capacitors in series to achieve a voltage of 2.64 MV. The Marx components are submerged in mineral oil (Shell Diala) to prevent local corona and ionization that would result in electric discharge to the grounded frame.

2.1.3 Pulse-forming line

The pulse-forming line is an aluminum tube of 30.5 cm in diameter concentrically suspended by nylon rods in a steel tube of 61 cm in diameter that is the grounded frame for this section of the machine. The pulse forming line is oil filled to prevent electric discharge to the grounded coax. The voltage pulse from the Marx generator enters the pulse forming line laterally via a sodium-thiosulfate water resistor at approximately 1/8 the total distance of the line from the terminus. The voltage pulse will propagate out from where the feed enters the pulse line in both directions along the line. The voltage pulse that travels upstream to the dead end of the pulse forming line will result in a reflection that will then travel downstream toward the switch end of the line. The portion of the voltage pulse that originally propagated toward the switch end of the pulse forming line works to close, by self-arc-ing through oil, the output switch. The dead end stub of the pulse-forming line is 0.30 m long, and the portion of the line that leads to the output switch is 1.73 m long.

2.1.4 Output switch

The output switch is simply a gap between the terminus of the pulse-forming line and the beginning of an increased-impedance pulse line. The void is filled with oil, but the behavior of the switch is determined by the shape of the termini of the two lines, both of which are full-radiused semi-spherical where they face one another. The voltage pulse from the pulse-forming line initiates ionized channels that conduct electrons through the oil, which will electrically bridge the gap and allow the voltage pulse to continue into the increased-impedance line.

2.1.5 Output transmission line

The increased-impedance pulse line is an aluminum tube with a diameter of 21 cm concentrically suspended by nylon rods downstream in the same steel tube as the pulse-forming line. The dimensions of the pulse line result in an increase in the impedance compared to the PFL thereby shortening the rise time of the voltage pulse and increasing the output voltage. This line is 1.77 m long. The upstream end of the increased-impedance line ends in a full-radiused semi-spherical termination as stated previously. The downstream end of the line mates to a similarly radiused flange with five sharpened steel pins that constitute the upstream side of the sharpening switch.

2.1.6 Sharpening switch

The sharpening switch when closed is comprised of five self-breaking oil switches from the tips of the sharpened steel pins of the terminus of the increased-impedance line to five opposing sharpened steel pins mounted upon the upstream terminus of the feed pulse line. [insert picture] The multiple channels allow for a lower switch inductance. The sharpening switch blocks voltage prepulse and can be adjusted to block the slow rise time of the voltage pulse from the PFL resulting in a sharper rise (shorter rise time).

2.1.7 Oil transmission line

The oil transmission line is an aluminum tube of the same radius as the output transmission line. This line, 0.28 m long, starts in oil at the sharpening switch and feeds through the water wedge and mates with the flared end of the vacuum line.

2.1.8 Water wedge

The water wedge acts as an interface between the oil and vacuum environments. The conducting sodium thiosulfate-water solution that makes the wedge is contained by two acrylic plates which separate it from the oil filled and vacuum sections of the grounded frame. The water wedge acts as a resistor between the feed transmission line and the grounded frame of the machine (5-10 k Ω). TriMeV needs the wedge to provide a uniform electric field grading at the insulator stack.

2.1.9 Vacuum insulator

The insulator consists of a contoured acrylic plate and embedded anodized aluminum rings. The vacuum insulator surface is designed to minimize the possibility of discharge between the transmission line and the grounded frame by a) the contours in the vacuum side of the acrylic so as to increase the length each channel must traverse to achieve discharge to ground and b) the presence of grading rings to grade the electric field in temporal directions and reduce the build up of charge for any given angle for the duration of the shot thus minimizing the probability of insulator breakdown.

The insulator is not self healing so it necessitates more frequent maintenance than the rest of the system to prevent insulator damage to and ensure proper delivery of electrical energy to the load. With use, dendritic channels will be branded into the vacuum surface of the acrylic. These channels are patterned failures of the acrylic that increase the

chances of insulator breakdown and are permanent so they must be polished out of the surface to prevent insulator flash over.

2.1.10 Vacuum transmission line

The inner vacuum transmission line is a 2.6-m-long, anodized-aluminum cathode flared on the upstream end. The cathode is 17 cm in diameter and is surrounded by an anode tube with a diameter of resulting in a 60- Ω impedance cathode.

During operation it takes the voltage pulse 9 ns to traverse the vacuum cathode line. The vacuum line pockets into a field shaper on the downstream end. The field shaper has rounded chamfered edges so as to eliminate any sharp corners that would encourage electron emission. The field shaper also enables the mounting of diode hardware to the cathode stalk. The length of the vacuum line (keep in mind it represents approximately one-half of the total length of the machine) serves to time-isolate the voltage pulse from interference of secondary pulse reflections caused by components in the machine. This gives the investigator a better understanding of the initial voltage pulse by minimizing interference from secondary pulse reflections.

Chapter 3

Theory

Herein is a description of the relevant theory relating to the production of photons and their detection in the TriMeV flash radiography system.

3.1 Electric charges and interactions

3.1.1 Bremsstrahlung radiation

Charged particles that experience an acceleration will produce radiation.

Following Jackson we start with statements of electric and magnetic field due to a charge in motion.

$$\mathbf{E} = \frac{e\mu_0}{4\pi c^2} \left[\frac{\mathbf{n} - \boldsymbol{\beta}}{\gamma^2 (1 - \boldsymbol{\beta} \cdot \mathbf{n})^3 R^2} \right]_{ret} + \frac{e\mu_0}{4\pi c^3} \left[\frac{\mathbf{n} \times ((\mathbf{n} - \boldsymbol{\beta}) \times \dot{\boldsymbol{\beta}})}{(1 - \boldsymbol{\beta} \cdot \mathbf{n})^3 R} \right]_{ret} \quad (3.1)$$

$$\mathbf{B} = \frac{1}{c} [\mathbf{n} \times \mathbf{E}]_{ret} \quad (3.2)$$

In the limit of being far away the first term in our description of the electric field becomes negligible due to it's $\frac{1}{R^2}$ dependence and when the charge is moving slowly (i.e. $\beta \ll 1$) such that the expression of the electric field further simplifies.

$$\mathbf{E} = \frac{e}{4\pi\epsilon_0 c} \left[\frac{\mathbf{n} \times (\mathbf{n} \times \dot{\boldsymbol{\beta}})}{R} \right]_{ret} \quad (3.3)$$

$$\mathbf{B} = \frac{e}{4\pi\epsilon_0 c^2} \left[\frac{\mathbf{n} \times \dot{\boldsymbol{\beta}}}{R} \right]_{ret} \quad (3.4)$$

The Poynting vector describes the instantaneous energy flux.

$$\begin{aligned}
\mathbf{S} &= \frac{1}{\mu_0} (\mathbf{E} \times \mathbf{B}) \\
\mathbf{S} &= \frac{1}{\mu_0} \left(\frac{e}{4\pi\epsilon_0} \right)^2 \frac{e^2}{c^3} \left| \frac{\mathbf{n} \times (\mathbf{n} \times \dot{\boldsymbol{\beta}})}{R} \right|^2 \mathbf{n} \\
\mathbf{S} &= \frac{1}{\epsilon_0} \left(\frac{e}{4\pi} \right)^2 \frac{e^2}{c^3} \left| \frac{\mathbf{n} \times (\mathbf{n} \times \dot{\mathbf{v}})}{R} \right|^2 \mathbf{n}
\end{aligned} \tag{3.5}$$

Here I have used $\frac{1}{\mu_0\epsilon_0} = c^2$ and $\dot{\boldsymbol{\beta}} = \frac{\dot{\mathbf{v}}}{c}$. The power radiated per solid angle can be written as the scalar product of the pointing vector and the unit vector scaled by R^2 .

$$\begin{aligned}
\frac{dP}{d\Omega} &= \mathbf{S} \cdot \mathbf{n} R^2 \\
\frac{dP}{d\Omega} &= \frac{1}{\epsilon_0} \left(\frac{e}{4\pi} \right)^2 \frac{e^2}{c^3} |\mathbf{n} \times (\mathbf{n} \times \dot{\mathbf{v}})|^2 \\
\frac{dP}{d\Omega} &= \frac{1}{\epsilon_0} \left(\frac{e}{4\pi} \right)^2 \frac{e^2}{c^3} |\dot{\mathbf{v}}|^2 \sin^2 \theta
\end{aligned} \tag{3.6}$$

When integrated over all solid angle the total radiated power is recovered.

$$\begin{aligned}
\int dP &= \frac{e^2}{16\pi^2\epsilon_0 c^3} |\dot{\mathbf{v}}|^2 \int_0^{2\pi} d\phi \int_0^\pi \sin^3 \theta d\theta \\
P &= \frac{e^2}{16\pi^2\epsilon_0 c^3} |\dot{\mathbf{v}}|^2 2\pi \int_0^\pi \sin^3 \theta d\theta \\
P &= \frac{e^2}{16\pi^2\epsilon_0 c^3} |\dot{\mathbf{v}}|^2 2\pi \left(\frac{\cos^3 \theta}{3} - \cos \theta \right) \Big|_0^\pi \\
P &= \frac{e^2}{6\pi\epsilon_0 c^3} |\dot{\mathbf{v}}|^2
\end{aligned} \tag{3.7}$$

Which is the Larmor result [17] for the non-relativistic case and expresses the power in photons that can be achieved by this method.

To be more specific the deflection of electrons impinging upon a high Z material will experience an acceleration when satisfying the cross section of the nuclei and will result in a liberation of energy in electromagnetic radiation.

3.1.2 Photon Attenuation and Transmission

Radiography is the technique of taking two-dimensional exposures with a subject providing attenuation specific to position in the image plane. The image gives information about the subject's attenuation power as a function of ray lines from the x-ray source to the detector. The transmission and attenuation of electromagnetic radiation can be described by the Beer-Lambert law.

When photons are incident on a test object the light can be absorbed, scattered or transmitted. Transmission is defined as the propagation of the incident species through a medium. Consider a piece of our test object that has an illuminated area A , thickness dx and a density of scattering/absorbing centers C . The number of centers subject to the photons in this piece of our test object is the product of the density of the centers and the volume of the piece.

$$\#centers = CA dx \quad (3.8)$$

The total effective area of the centers is the number of centers multiplied by the cross section of the centers.

$$\sigma CA dx \quad (3.9)$$

Where σ is the cross section or the probability that a photon is removed (by scattering or absorption) from the incident ray.

If we define I_x as the intensity of the beam we can write the probability a photon will be removed ($P_{removal}$) from the incident ray as the following.

$$P_{removal} = -\frac{dI_x}{I_x} = \frac{\sigma CA dx}{A} \quad (3.10)$$

Here I have use dI_x to denote the change in intensity of the beam after the effects of the test object piece. If we want to know the final intensity of the beam relative to the incident intensity after the effects of the piece of the test object we can simply integrate to find the solution to the differential equation.

$$\int_{I_0}^I \frac{dI_x}{I_x} = - \int_0^x \sigma C dx$$

$$\ln(I) - \ln(I_0) = \ln\left(\frac{I}{I_0}\right) = -\sigma C x \quad (3.11)$$

This statement can be inverted and written as an exponential expression.

$$I = I_0 e^{-\mu x} \quad (3.12)$$

Where μ is the linear attenuation coefficient and is equal to $\sigma C x$ when one assumes the scattering effects are negligible.

3.1.3 Lorentz force law

Coulombs law defines the force (\mathbf{F}_e) on a charged body as the product of the charge (q) the body is imbued with and the electric field (\mathbf{E}) the body has been subject to.

$$\mathbf{F}_e = q\mathbf{E} \quad (3.13)$$

Next, following Purcell's argument[18], consider a test charge moving parallel to a current carrying wire in the lab frame. Suppose the current and the charge are moving in parallel at the same speed as in figure 3.1. Now notice that in the frame of the charge Q the wire appears to be conveying current by the movement of negative charges. Furthermore the charges are more concentrated due to length contraction so in this frame the positive charge Q is attracted to the overall negatively charged wire in the frame of charge Q . Equivalence suggests that the upward force found in charge Q 's reference frame should also be present in the lab frame.

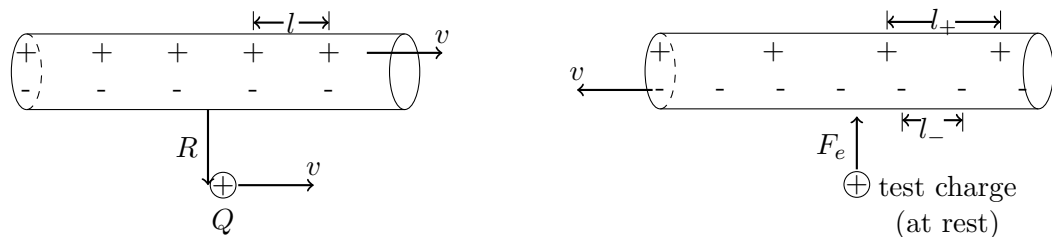


FIGURE 3.1: Charge Q in the presence of a current carrying wire in the lab frame (left) and the charge Q frame (right). Notice the concentration of the negative charge carriers in the charge Q frame due to length contraction.

Quantifying the negative charge separations in the wire in charge Q's reference frame and taking $\gamma = \frac{1}{\sqrt{1-v^2/c^2}}$ gives the following.

$$\begin{aligned} l_- &= \frac{l}{\gamma} \\ l_+ &= l\gamma \end{aligned} \tag{3.14}$$

Where l_- is the separation length of the negative charges in the wire and l_+ is the separation length of the positive charges in the wire both in the reference frame of charge Q.

Since I want to quantify the force I begin by writing the charge density of the wire in charge Q's reference frame.

$$\begin{aligned} \lambda &= \frac{q}{l_+} - \frac{q}{l_-} \\ \lambda &= \frac{q}{l} \left(\frac{1}{\gamma} - \gamma \right) \\ \lambda &\approx \frac{q}{l} \left(1 - \frac{1}{2} \left(\frac{v^2}{c^2} \right) - 1 - \frac{1}{2} \left(\frac{v^2}{c^2} \right) \right) \\ \lambda &\approx -\frac{q}{l} \left(\frac{v^2}{c^2} \right) \end{aligned} \tag{3.15}$$

Here I have assumed $v \ll c$ and used a binomial approximation so that $\gamma \approx 1 + \frac{1}{2} \left(\frac{v^2}{c^2} \right)$. Now, quantifying the electrostatic force in the reference frame of Q gives the following.

$$\begin{aligned} F_e &= QE \\ F_e &= Q \frac{\lambda}{2\pi\epsilon_0 R} \\ F_e &\approx \frac{Qqv^2}{2\pi\epsilon_0 l R c^2} \end{aligned} \tag{3.16}$$

Recall R is the distance from the test charge to the wire (normal to the wire) so with current in the lab frame as $I = \frac{qv}{l}$ and $\mu_0 = \epsilon_0 c^2$ the magnetic force in the lab frame can be written.

$$\begin{aligned}
 F_m &\approx \frac{Qv}{2\pi\mu_0 R} \\
 F_m &\approx QvB
 \end{aligned}
 \tag{3.17}$$

Here we continue to rely on the assumption that $v \ll c$ and with a careful examination of the geometry of the system and we write the Lorentz force law as the following.

$$\mathbf{F} = q (\mathbf{E} + \mathbf{v} \times \mathbf{B})
 \tag{3.18}$$

3.1.4 Bennett equilibrium

The Bennett condition is defined as the balance of two forces in a current carrying plasma in the geometry described in the graphic.

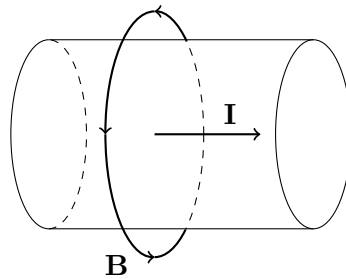


FIGURE 3.2: Plasma z-pinch geometry

The expansion force being the kinetic gas pressure due to the energy in the plasma and the magnetic confinement force that a mobile charge experiences when moving axially through a curling magnetic field. So staying true to the definition we begin with the balanced opposition of these two forces.

$$\mathbf{F}_{expansion} = -\mathbf{F}_{confinement}
 \tag{3.19}$$

The expansion force can be described in terms of kinetic gas pressure, P , of the plasma and a unit volume V and the confinement force as described by the Lorentz force.

$$\begin{aligned}
 \nabla P &= \mathbf{J} \times \mathbf{B} \\
 \frac{\partial P}{\partial r} &= -J_z B_\theta
 \end{aligned}
 \tag{3.20}$$

Where here I have used the charge and the velocity divided by a unit volume gives the current density, $\mathbf{J} = \frac{e\mathbf{v}}{V}$ and have set defined the current as being along the z axis.

For an azimuthal, fixed radius (r) path the magnetic field from a constant current will be constant and can be resolved by integrating Amperes law after working out the cross product.

$$\begin{aligned} \nabla \times \mathbf{B} &= \mu_0 \mathbf{J} \\ \begin{vmatrix} \hat{r} & \hat{\theta} & \hat{z} \\ \frac{\partial}{\partial r} & \frac{\partial}{\partial \theta} & \frac{\partial}{\partial z} \\ B_r & rB_\theta & B_z \end{vmatrix} &= \mu_0 \mathbf{J} \\ -\frac{\hat{r}}{r} \frac{\partial}{\partial z}(rB_\theta) + \frac{\hat{z}}{r} \frac{\partial}{\partial r}(rB_\theta) &= \mu_0 \mathbf{J} \\ \frac{1}{r} \frac{\partial}{\partial r}(rB_\theta) &= \mu_0 J_z \end{aligned} \quad (3.21)$$

By substitution we can write the following.

$$-\frac{1}{\mu_0} \frac{1}{r} \frac{\partial}{\partial r}(rB_\theta)B_\theta = \frac{\partial P}{\partial r} \quad (3.22)$$

If we multiply both sides by $r^2 dr$ and integrate using integration by parts ($u = r^2$ and $dv = \frac{\partial P}{\partial r} dr$) we will have this.

$$\begin{aligned} -\int_0^R \frac{1}{\mu_0} \frac{1}{r} \frac{\partial}{\partial r}(rB_\theta)B_\theta r^2 dr &= \int_0^R \frac{\partial P}{\partial r} r^2 dr \\ -\frac{1}{2\mu_0} \int_0^R \frac{\partial}{\partial r}(rB_\theta)^2 dr &= \int_0^R u dv \\ -\frac{1}{2\mu_0} (RB_\theta)^2 &= u \cdot v - \int_0^R v du \\ -\frac{1}{2\mu_0} (RB_\theta)^2 &= Pr^2 \Big|_0^R - \int_0^R P 2r dr \\ -\frac{1}{2\mu_0} (RB_\theta)^2 &= -\frac{1}{\pi} \int_0^R P 2\pi r dr \\ -\frac{1}{2\mu_0} (RB_\theta)^2 &= -\frac{kT}{\pi} \int_0^R 2\pi r n dr \\ -\frac{1}{2\mu_0} (RB_\theta)^2 &= -\frac{NkT}{\pi} \end{aligned} \quad (3.23)$$

Where I have used the ideal gas law of $P = nkT$, $\int_0^R 2\pi r n dr = N$ and the fact that pressure $P = 0$ when $r = R$. Let's pause to work out a substitution for the magnetic field B_θ from Ampere's law.

$$\begin{aligned}
 \nabla \times \mathbf{B} &= \mu_0 \mathbf{J} \\
 \int \nabla \times \mathbf{B} \cdot d\mathbf{S} &= \int \mu_0 \mathbf{J} \cdot d\mathbf{S} \\
 \int \mathbf{B} \cdot d\mathbf{l} &= \int \mu_0 \mathbf{J} \cdot d\mathbf{S} \\
 2\pi R B_\theta &= \mu_0 I
 \end{aligned} \tag{3.24}$$

So after inverting this result and substituting the relation becomes the following.

$$\begin{aligned}
 -\frac{1}{2\mu_0} \left(R \frac{\mu_0 I}{2\pi R} \right)^2 &= -\frac{NkT}{\pi} \\
 \frac{\mu_0}{4\pi} I^2 &= 2NkT
 \end{aligned} \tag{3.25}$$

This is the Bennett equilibrium condition and describes how the plasma is more forcefully confined for higher currents. For our case we are often interested in the confinement of an electron beam not a plasma so we start with a statement of the electrostatic pressure due to the charge of the electrons in the beam.

$$\begin{aligned}
 P &= \frac{U}{V} \\
 P &= \frac{1}{4\pi\epsilon_0} \frac{q^2}{Vr} \\
 P &= \frac{1}{4\pi\epsilon_0} \frac{(ne)^2 V}{r}
 \end{aligned} \tag{3.26}$$

Here I have used the charge is the product between the density of electrons, the charge of each electron, and the volume they occupy ($q = neV$). Next, repeat 3.23 but with the pressure expression for the electron beam and $V = 2\pi r^2 l$.

$$\begin{aligned}
-\int_0^R \frac{1}{\mu_0} \frac{1}{r} \frac{\partial}{\partial r} (rB_\theta) B_\theta r^2 dr &= \int_0^R \frac{\partial P}{\partial r} r^2 dr \\
-\frac{1}{2\mu_0} (RB_\theta)^2 &= -\int_0^R P 2r dr \\
-\frac{1}{2\mu_0} (RB_\theta)^2 &= -\frac{e^2}{4\pi\epsilon_0} \frac{1}{\pi} \int_0^R (2\pi r n l)^2 dr \\
-\frac{1}{2\mu_0} (RB_\theta)^2 &= -\frac{e^2}{4\pi\epsilon_0} \frac{l}{n 2\pi^2} \int_0^{n 2\pi R} \Gamma^2 d\Gamma \\
-\frac{1}{2\mu_0} (RB_\theta)^2 &= -\frac{e^2}{4\pi\epsilon_0} \frac{l}{n 2\pi^2} \frac{\Gamma^3}{3} \Big|_0^{n 2\pi R} \\
-\frac{1}{2\mu_0} (RB_\theta)^2 &= -\frac{e^2}{4\pi\epsilon_0} \frac{l n^2 4\pi R^3}{3} \\
-\frac{1}{2\mu_0} (RB_\theta)^2 &= -\frac{e^2}{4\pi\epsilon_0} \frac{l N^2}{3\pi R}
\end{aligned} \tag{3.27}$$

Where I have used the substitution $\Gamma = n 2\pi r$ and for simplicity have assumed a uniform electron density. Now the equilibrium relation for the confined electron beam can be expressed.

$$\begin{aligned}
-\frac{1}{2\mu_0} \left(R \frac{\mu_0 I}{2\pi R} \right)^2 &= -\frac{e^2}{4\pi\epsilon_0} \frac{l N^2}{3\pi R} \\
\frac{\mu_0}{4\pi} I^2 &= \frac{e^2}{4\pi\epsilon_0} \frac{l N^2}{3\pi R} \\
I^2 &= \frac{c^2 e^2}{3\pi} \frac{l N^2}{R}
\end{aligned} \tag{3.28}$$

3.2 Figure of merit

Common challenges in flash radiography include the duration of the flash, the physical extent of the radiographic source and the brightness of the source. Short duration is desirable to reduce blur in the radiograph due to the motion of the subject being imaged. The discrete extent of the radiographic source allows resolution of finer detail of the subject. Since often it is not possible to place the image plate (IP) and the subject in close proximity, the brightness of the source allows the subject and the IP to be separated by some distance yet still maintain a high enough dose at the IP to produce an image. Due to these factors Charlie Martin CBE [19] proposed the figure of

merit (FOM) as a way to compare different radiographic systems based on the possible image quality each could produce.

$$FOM = \frac{D}{s^2} \quad (3.29)$$

Where D is the dose observed (in rad) at a meter from the source and s the diameter of the x-ray source (in mm). When improvements in the radiographic quality are the objective (i.e. increases in the FOM) one seeks to decrease the spot size and increase the dose delivered.

3.3 Component characterization

The electrical characteristics of pulsed power components can be calculated based on geometry.

3.3.1 Impedance

In general the impedance (Z) is defined in this way[17].

$$Z = \frac{V}{I} \quad (3.30)$$

So when one wants to know the impedance of a component the answer is as simple as dividing the voltage (V) by the current (I) across the component.

Alternatively the geometric impedance can be calculated using the capacitance (C) and inductance (L) of a component[20]. First recognize the magnetic and electric energies (U_M and U_E) in an electromagnetic wave are equal. Then rearrange and simplify to give the impedance.

$$\begin{aligned} U_M &= U_E \\ \frac{1}{2}LI^2 &= \frac{1}{2}CV^2 \\ \sqrt{\frac{L}{C}} &= \frac{V}{I} = Z \end{aligned} \quad (3.31)$$

In the case of a coaxial line the we can find the inductance per unit length starting with a statement of the inductive energy taking into account $H = J_{enc} = \frac{I_{enc}}{2\pi r}$ as a statement of Ampere's law for this geometry.

$$\begin{aligned}
 U_H &= \frac{1}{2}LI^2 = \frac{1}{2}\mu \int H^2 dV \\
 \frac{1}{2}LI^2 &= \frac{1}{2} \int \left(\frac{1}{2\pi r}\right)^2 l2\pi r dr \\
 \frac{L}{l} &= \frac{\mu}{2\pi} \int_a^b \left(\frac{1}{r}\right) dr \\
 \frac{L}{l} &= \frac{\mu}{2\pi} \ln\left(\frac{b}{a}\right)
 \end{aligned} \tag{3.32}$$

The voltage in the capacitor is just the integral of the electric field over the gap between the plates of the capacitor. Keep in mind that Gauss's law for this geometry tells us $E = \frac{\sigma}{\epsilon} = \frac{Q}{\epsilon A} = \frac{\lambda}{\epsilon 2\pi r}$.

$$\begin{aligned}
 V &= \int_a^b E dr \\
 V &= \frac{\lambda}{\epsilon 2\pi} \int_a^b \frac{1}{r} dr \\
 V &= \frac{\lambda}{\epsilon 2\pi} \ln\left(\frac{b}{a}\right)
 \end{aligned} \tag{3.33}$$

Using the definition of capacitance we can combine these statements.

$$\begin{aligned}
 C &= \frac{Q}{V} \\
 \frac{C}{l} &= \frac{\lambda}{V} \\
 \frac{C}{l} &= \frac{\epsilon 2\pi}{\ln\left(\frac{b}{a}\right)}
 \end{aligned} \tag{3.34}$$

So we know the impedance of the coaxial line.

$$\begin{aligned} Z &= \sqrt{\frac{L}{C}} \\ Z &= \frac{1}{2\pi} \sqrt{\frac{\mu}{\epsilon}} \ln\left(\frac{b}{a}\right) \end{aligned} \tag{3.35}$$

Chapter 4

Operational description

4.1 Circuit simulation

I wanted to quantify the noise observed in the voltage diagnostic for both the output and sharpening switches as it relates to the best possible simulation recreated voltage signal. Base line voltage acquisition, prior to the signal, was collected as a description of the noise inherent in the system. This is an assumption that may not be fully true to the noise associated with the voltage signal but should describe, at least in part, the noise of the voltage diagnostics and allow an estimate on the quality of the best possible agreement between the simulation and experimental data. The deviation in the baseline data describes the stochastic distribution of the voltage data and gives a way to quantify the inherent behavior of the system (see figure 4.1). In shot 194 the diagnostic data from the output and sharpening switches begin at -332 ns and the voltage pulse begins at approximately 590 ns. The standard deviation of the leader data for the voltage at the output and sharpening switches are 38.7 and 29.8 kV respectively. This means that if we have a perfect fit or simulation of the diagnostic the smallest possible deviation between the data and the fit/simulation would be 38.7 and 29.8 kV respectively for the output and sharpening switches.

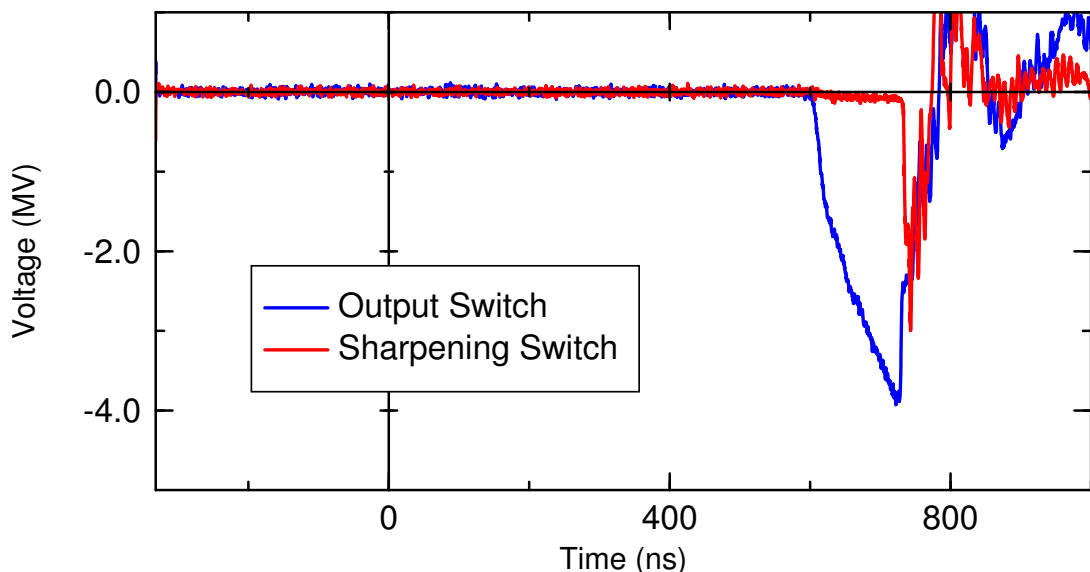


FIGURE 4.1: Data from shot 194 for all the voltage and current diagnostic channels along the pulse line of the TriMeV system showing leaders.

Additionally the R^2 values can be calculated between the simulation and data and can be interpreted as a ratio of the deviations of the fit/simulation and the experimental data from the mean. The R^2 value is defined as follows.

$$R^2 = (1 - P)^2 = \frac{\sum (y_{sim} - \bar{y})^2}{\sum (y - \bar{y})^2} = \frac{\sigma_{sim}^2}{\sigma^2} \quad (4.1)$$

Where P is the probability that there exists no correlation between the data and simulation and σ is the standard deviation.

This suggests the best possible simulation of the data would exhibit an R^2 value no greater than 1 since if we could separate the stochastic noise from the pure signal in the experimental data we would find the deviation from the mean of the experimental data would be greater than the deviation from the mean of the pure signal extracted from the experimental data. So in the case of a fit or simulation that is true to the pure signal we will expect the same behavior.

4.2 Circuitry modeling

4.2.1 Screamer model

Our simulation shown in figures 4.2 and 4.3 (see section A.4.1 for simulation coding) of the TriMeV system included the elements shown in figure 4.4 which assumes that the capacitor banks and switches in the direct voltage line of the erected Marx generator can be modeled as a single capacitor, inductor, and resistor in series.

Since the comparison of the simulation vs experimental results was not satisfactory the next step is to model the Marx generator in more detail. Of course the difference in the original simulation and the experimental diagnostic (see figure 4.2) shows variation in the slope during the rise of the voltage at the output switch monitor. The low slope observed early in the voltage rise suggests that the initial inductance of the Marx stages in our model are too high. A literature search revealed that the inductance of gas switches is indeed variable with time and that the inductance of the switch arc could triple in the first 40 ns of the switch closure [21]. Imagining the reported inductance of the gas switch to be the peak inductance and assuming a similar behavior in the TriMeV Marx gas switches as reported in Persephonis et al. a reduction in inductance is needed to offer an agreement between simulation and experimental observation in voltage at the output switch.

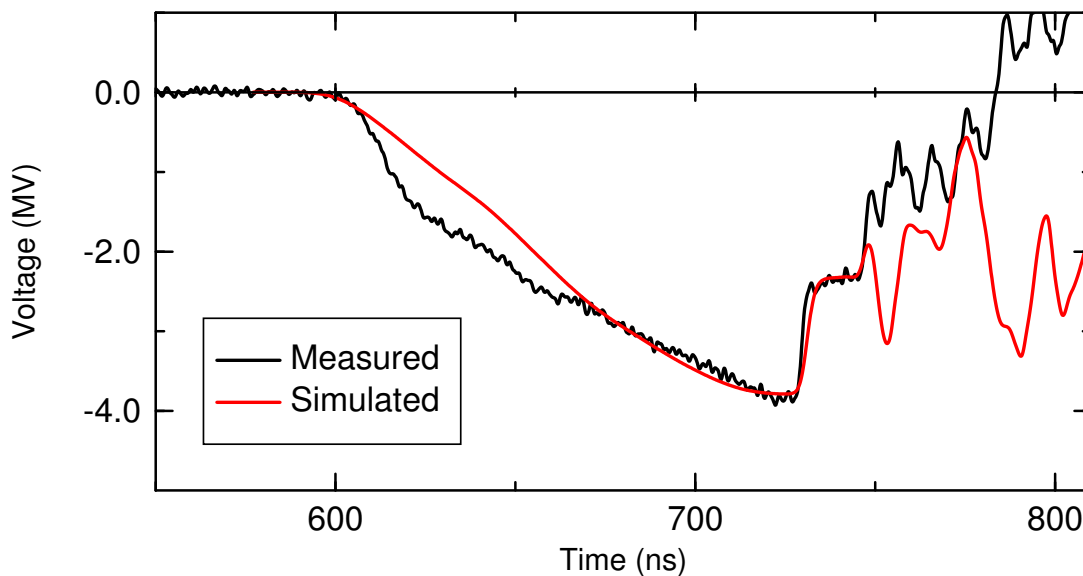


FIGURE 4.2: Data from shot 194 and simulation results of voltage at the output switch.

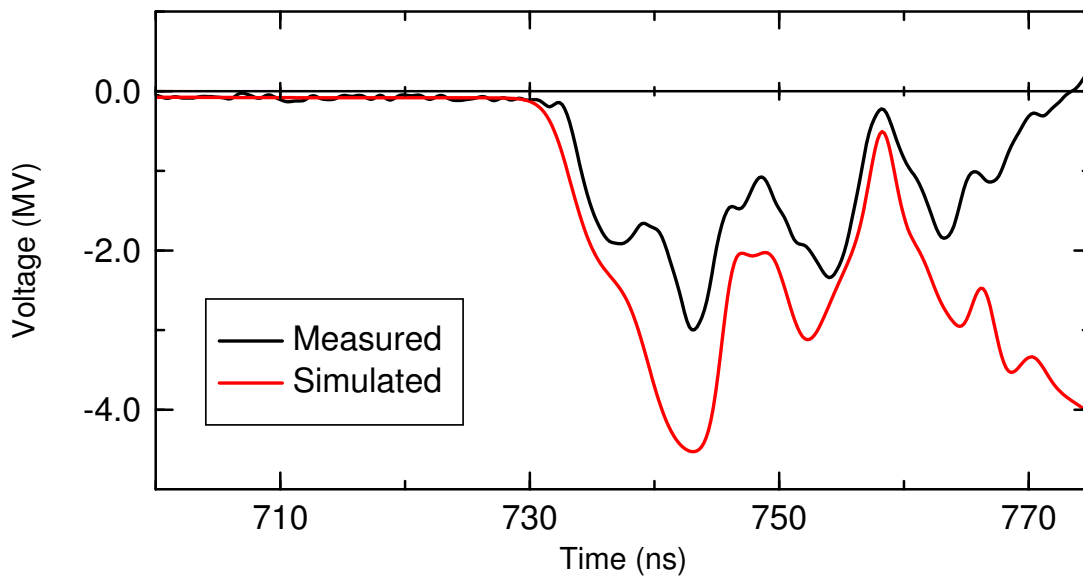


FIGURE 4.3: Data from shot 194 and simulation results of voltage at the sharpening switch.

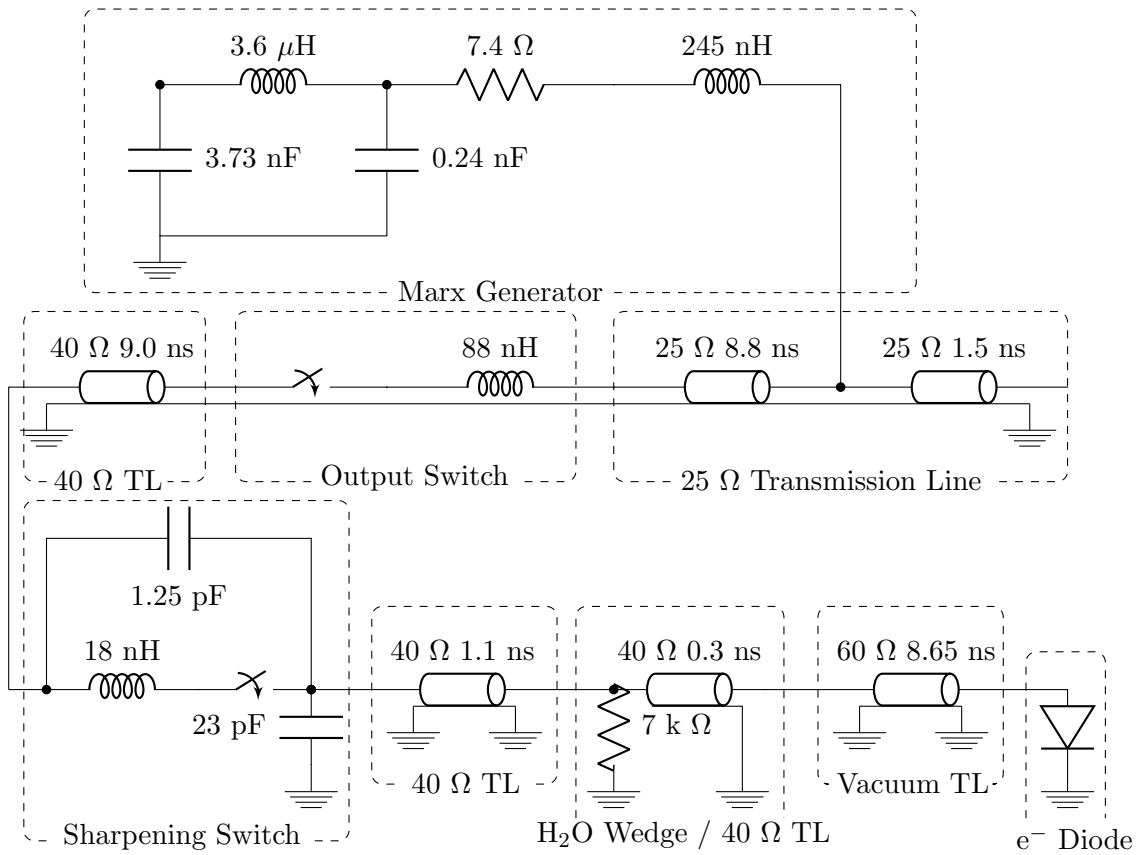


FIGURE 4.4: Simplified TriMeV circuit model showing the quantified components with the TriMeV parts labeled.

Chapter 5

Pathologies

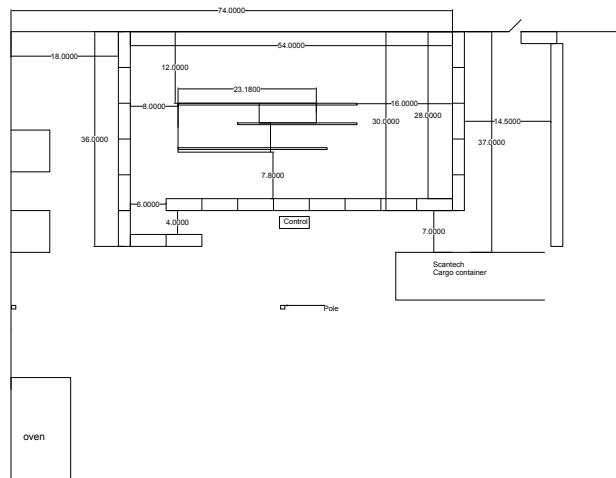
The TriMeV system is complex which means there are multiple modes of failure possible. The instruments used to take measurements add to the complexity and increase the possible modes of failure. Although not exhaustive this list includes failure modes that have been observed and what, in each case, was done to remedy the failure.

5.1 A-K gap variations

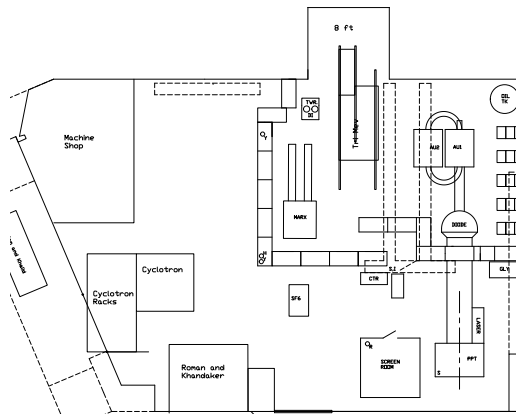
In general the proper sized gap between the anode and cathode depends on the characteristics of the running diode. This can be different for each diode design. Often the desired outcome is to maximize the power output of the diode in an effort to make the Bremsstrahlung source as bright as possible. Another possible objective is to maximize the electron beam extracted from the system. The intent of running at the ideal gap is to ensure the desired voltage/current balance for the intended purposes of the diode. When the gap is set too short the diode voltage may not reach the desired value and the desired electron energy will not be achieved resulting in lower x-ray energies.

5.2 TriMeV installations

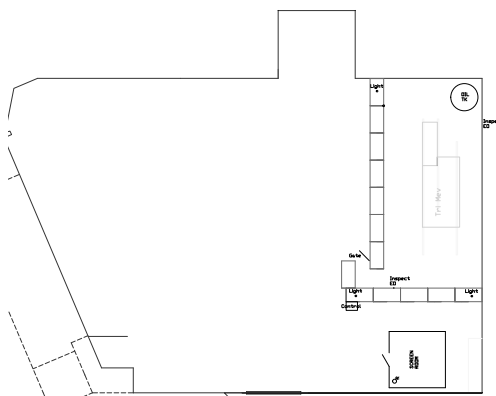
Initially there was little support available to set up the TriMeV system. The first requirement for setup was constructing appropriate shielding. After considering multiple options to install the shielding I obtained a forklift license and erected the TriMeV cell myself. After a year the cell was erected and the rails and oil tank were installed, and negotiations for electrical power were underway when events out of my control required that TriMeV be relocated. TriMeV was then installed over a period of five months and operational for 15 months. Unfortunately again due to circumstances beyond my control TriMeV had to be relocated a second time. TriMeV was then installed over a period of two months and has since been operational. The moves and time required to install the machine cut down the number of shots that I was able to perform.



(A) RISE layout



(B) IAC cell layout



(C) IAC highbay layout

FIGURE 5.1: TriMeV layouts

5.3 Missing parts

Throughout the life of TriMeV at ISU we have had to make replacements for missing parts of the system.

5.3.1 Data acquisition system

The data acquisition system is comprised of oscilloscopes and scanners to acquire the electronic data from the current and voltage diagnostics, x-ray PIN diodes, other electronic signal producing instrumentation, and radiographic data from phosphor screens. All of these components with the exception of the voltage and current diagnostics along the transmission line of the system had to be installed. Dose data from the OSLDs is also incorporated into the archived data. Stella software was chosen and installed to manage the data collection devices, store the data, and analyze the data.

5.3.2 Pump pallet

The pump system original to the system was used to pump oil from the Marx tank and oil filled sections of TriMeV to storage tanks in the event maintenance on the system required the oil be evacuated. The original pump featured a filter that cleaned the oil as it was pumped. A replacement pump was used to move oil between the TriMeV and the storage tank. Cleaning the oil in the Marx tank is an issue and our temporary solution is addressed in 5.11.

5.3.3 Hydraulic system support tray

The tray that supports the hydraulic pumps for raising and lowering the Marx generator was not included when TriMeV was delivered to ISU. a replacement support tray was fashioned from 3 equal lengths of iron C-channel and bolted to the frame of the system to support the hydraulic pump system used to raise and lower the Marx generator as well as the switch wash pump.

5.4 TG 80 discharge

On 20 January 2016 what sounded like a discharge was heard during a charging cycle in preparation to fire the system. Subsequent charging of the TG-80 resulted in a peak of

only 60 kV. Discharge was suspected of preventing the full charge voltage of 80 kV. When the TG-80 was removed from its casing the spark gap showed signs of use but nothing out of the ordinary. After dismantling the TG-80 signs of arcing along the charging resistor were located including carbon deposits and holes in the insulation sleeve between the charging resistor and the interior surface of the TG-80. Replacement parts from SLIA (TG-80 and charging resistor) were used to repair the system. The insulation sleeve was replaced from machined poly to match the part. After reassembly it was noted that the triggering of the system was not reliable but adjustments to the spark gap in the switch that connects the PT-55 and the TG-80 as well as the spark gap in the TG-80 seemed to restore the system's triggering reliability.

5.5 Output resistor

In February 2016 it was noted that the output voltage of the system was low. The output resistor which had not been refurbished was suspect. The salt water and the tubing was replaced in the resistor.

Ideally the output resistor is removed only after the Marx tank has been partially drained, as the resistor natively sits approximately 2 feet below the surface of the oil when the tank is full. Inconveniences in draining the Marx tank (particularly time constraints) often result in removing or installing the resistor without draining the tank at all. The resistor is removed by swinging the Marx assembly away from the pulse line section while simultaneously supporting the resistor. Failure to do so will result in the resistor sinking to the bottom of the tank. Needless to say the removal of the resistor is avoided unless absolutely necessary.

5.6 Insulator tracking

With use the vacuum insulator develops tracks in the surface of the acrylic which increase the probability of discharge from the pulse line to the grounded frame of the machine. During operation the potential is spread across the vacuum surface of the insulator. The insulator is made of a dielectric material and being a dielectric suggests that on the molecular level there is separation of charge in the material. It is thought that the electric field and the voltage together with the fact there's a mismatch in dielectric between the vacuum and the acrylic that energy is deposited in the surface of the acrylic sufficient to orient the molecules in a polarized way and fix those molecules in that orientation. Localized orientations can create conditions in the surface of the acrylic favorable for

ion channel formation lowering the energy threshold necessary for discharge across the vacuum insulator surface (flash over). Discharge across the insulator will result in a reduced voltage pulse, but more problematically is likely to damage the insulator. For these reasons the tracks must 1) be located by observing differences in reflection of bright light on the acrylic surface and 2) be polished out of the insulator surface on a regular basis. This is done with scratch-less Scotch-brite pads wetted with ethanol and copious amounts of hand buffing. The insulator tracking is invisible under normal ambient lighting and the variation in reflection due to these tracks is subtle making their identification difficult. Problematic also is the ability of the tracks to persist even after significant buffing making it necessary to buff, clean, and reinspect the insulator surface.

5.7 Log book centralization

It was suggested that we centralize the log books for the system. We wanted a solution that would allow remote access to the records. Multiple packages were considered and we decided to use Stefan Ritt's eelog program used at CERN [22]. Information Technology set up and maintains a server and installed the program. This program allows users to record information and can serve as a repository for system data and can allow access to data remotely.

5.8 Converter mounting

The converter needs to be mounted on the anode and affixed electrically. Methods to achieve this can be clamping, bolting, or epoxying. Silver epoxy is available, provides low electrical resistance, is easy to use, and provides a low out-gassing solution for vacuum applications. Its cure time is nominally one day but can be hastened by elevated temperatures.

5.9 System Trigger

The system trigger was observed to operate intermittently for a time then stopped working altogether. The signal from the operator console was not being sent to the PT-55 for triggering. It was discovered that the EMCO high voltage source in the operator console was not functioning and was replaced after which the trigger works as before the problem.

The trigger continues to exhibit some occasional misfires where the system will self trigger before the fire button is depressed. This can be problematic since most of the diagnostics channels are triggered from the fire signal to ensure synchronized timing between channels. Another way the system will occasionally misfire is where the fire button at the console is pressed but the system does not fire. Here too the collection of the diagnostics can be lost if the scopes are not re-armed before system triggering is again attempted.

5.10 Marx resistor replacements

The charging and triggering liquid resistors in the Marx generator were not operational on arrival. The water had evaporated from the salt water resistors. They were removed, the connectors refurbished, and the resistors reassembled with fresh copper-sulfate solution and new tubing.

Later air dissolved in the salt water came out of solution forming bubbles. The bubbles aggregate and reduce the liquid cross-section of the path the current can flow through. This causes wear in the resistors and affects machine performance. Subsequent refurbishment of the resistors involved an additional step of evacuating the air from the salt water by lowering the ambient pressure before the resistor was filled. This has reduced the bubbles forming in the resistors during use and has lengthened the lifetime of the resistors and improved the reliability of the Marx generator.

5.11 Oil fouling

When arcs close through oil, they damage the oil molecules leaving carbon particulates in the oil. The machine is equipped with a switch-wash pump which pumps oil from near the switches through a filter in an effort to reduce the concentration of said particulates. The original oil pump pallet was equipped with a filter so that when the Marx tank was drained the oil would be filtered. Because the original pump pallet was not included with the machine this benefit was not realized.

A temporary oil cleaning system was installed on the Marx tank which pumps oil from one end of the tank through a filter into the other end of the tank.

5.12 Grading ring creep

During shots the grading rings in the insulator stack experience forces parallel to the axis of the machine which cause them to creep forward in the direction of the vacuum environment out of the insulator stack over multiple shots. The rings (made of anodized aluminum) are held into the acrylic insulator by polyethelene set pins which seat into grooves in the insulator acrylic. This means that over time the pressure on the set pins causes the pins to swell and locks the threads of the set pins tightly enough that a hex wrench will strip the hex head of a pin before it can be removed from the grading ring. The set pins cannot be removed without difficulty, potential of damaging the insulator, and destruction of the set pin.

The grading rings are checked every ten shots and if they are out of alignment they are re-seated with a rubber mallet and the set pins tightened. Once within the course of ten shots one ring crept forward until the set pins pinned against the thinnest part of the acrylic in the insulator stack. This temporal pressure on the acrylic chipped the insulator in two different locations, required the grading ring to be re-seated, and the damaged set pins to be removed. To remove the set pins it was necessary heat a hex wrench and melt the wrench into the head of the pin. After the wrench and pin cooled only then could adequate torque be applied to remove the set pins. This heated wrench is dangerous when working near the acrylic insulator and required great care. New set pins were installed to replace the damaged set screws that were removed but many of the original pins continue to hold the grading rings. The chips were less than 1 cm in span, therefore it was suspected they would not cause a problem for the overall function of the system. They were sanded down to even out the sharp contours and then buffed to match the sheen of the insulator surface. Since this occurrence, grading ring creep of this magnitude has not been observed.

5.13 Trigger timing

The reliability of the timing of the system prevents experiments that would require precise timing of the voltage pulse. For instance, x-pinch back-lit experiments would require highly coordinated timing between the back light and the voltage pulse. The timing "jitter" of the machine makes such experiments possible only if they can be triggered by a diagnostic from the TriMeV system itself. The largest source of this timing inconsistency is suspected to be the oil-bathed self-closing switches along the pulse line. Improvement of this inconsistency might be obtained by installing gas-pressure

switches in lieu of the oil-bathed switches. These gas-pressure switches could be triggered externally improving the timing reliability of the system as a whole.

5.14 Output Switch D-dot

Occasionally and intermittently the signal from the output switch appears to be shorted in discreet time bundles, e.g., the signal will look like it is on and then go to zero over the lifetime of the pulse. Connections and cables between the diagnostic and the scope have been checked but no obvious problem has been noted. Unfortunately this inconsistency continues to be a problem. This issue occurs approximately one in 30 shots.

5.15 Scope trigger and timing

Timing of the data is critical when comparing one channel to another or performing operations between two channels. For instance one can compute the impedance of the diode from the voltage and current diagnostics from the diode, but only if they are both synchronized in time.

To ensure synchronized timing of data and diagnostic signals, dedicated oscilloscopes are triggered with a signal from the fire button of the operator console. This ensures that the channels of the dedicated oscilloscopes are synchronized in time. These channels monitor the voltage and current diagnostics as well as the silicon PIN diode signals. The voltage and current diagnostics are all synchronized because each of the associated channels are triggered from the same source and the cable length for all of the diagnostics is the same. PIN diodes and other accessory instrumentation at the source may have different cable lengths, but those lengths are known and at least one channel from each instrument is synchronized with the fire button. Knowing the length of the cable and velocity of the signal enables one to calculate the absolute timing of each signal.

5.16 Landauer OSLD system

The Landauer OSL system posed some challenges which all could have been avoided given additional financial resources.

5.16.1 Condition of the dosimeters

The dosimeters used for this work were chosen from the supply available. By the dates of the previous calibrations and of the user manual I estimate these OSLDs have been in use since 2002-2008. There is little information on the previous treatments of the OSLDs yet there appear to be some OSLDs that bleach more completely and exhibit a smaller standard deviation than others. The previous treatment of a particular OSLD is expected to have an effect on its ability to perform as a dose measuring device. It is recommended that future use of the inlight system begin with a calibration of the reader, and a survey of the available population to select particular OSLDs that exhibit desired characteristics (i.e. a small enough standard deviation requisite to the tolerances required by the future work, propensity for jamming, the efficacy and efficiency of the bleaching process, etc...)

Repeated use of the Landauer reader (particularly the cassette adapter for the dots) appears to suffer from wear. This wear is manifest in jamming of OSLDs in the reader and the often sporadic inability of the cassette and mechanical parts to effectively open the opaque case of the OSLD during the reading protocol. The most common mode of jamming for our reader can be remedied by sanding off the lower left hand corner of the case at a 45 degree angle so that there is no normal surface for the cassette floor to catch on when the OSL is mechanically returned to the cassette after reading. There is evidence that the case of the OSLD catches on itself manifest by another mode of jamming in the reader and failure of the cassette and associated mechanical parts in opening the case of the OSLD. These failures are likely due to warping of the case of the OSLD. Conditions suspect of leading to this behavior are repeated use and attempts to force a jammed OSLD, heating and cooling of the OSLD and the case, and the aging of the plastic case of the OSLD. Recommendations for these issues are to avoid prolonged exposure to heat (as during bleaching of the OSL chip), to refrain from forcing a jammed OSLD in the reader, and to consider altering the case by sanding the corner as mentioned previously.

5.16.2 Calibration of the OSLD system

Landauer can provide screened dots for calibration which are chosen to give a higher tolerance. Landauer claims the screened dots exhibit a standard deviation of 3% compared to 5% for standard dots. Landauer will also provide a set of calibrates which are pre-exposed to known doses.

5.16.3 Repeated readings and fade over time

Literature suggests [23] exposed dots will fade over time meaning the electrons in the trapped state have a lifetime and eventually will suffer a reduction in response to stimulation (due to environmental factors, possibly thermal effects). For this reason Landauer recommends calibrates be utilized only within one year of original exposure.

Repeated reading of the OSLDs will also reduce the population of defect trapped electrons and thereby reduce the response to stimulation. Landauer recommends only 20 readings be allowed for each calibrate dot.

These limitations of holding response over time and stimulation are expected to have little effect on this work as all of the readings of the OSLDs have taken place after only a small time (usually less than one hour and rarely more than one month) and the number of readings is limited (rarely more than 20 but usually less than 5).

5.17 Denoptix QST scanner

The Denoptix QST system is a phosphor screen based system designed for the dental industry to produce digital clinical x-ray images.

5.17.1 Data preconditioning

The Denoptix scanner does some preconditioning of the image to produce a better contrast for x-ray images in the context of a dental practice. The way in which the images are conditioned is a guarded and proprietary secret. The scanner software will give the option to request an image without preconditioning yet the scanner does not in all cases return an image after a scan. This suggests that the system is still not giving raw data relating to the image screen's response to the stimulating laser but rather some form a preconditioned data. Originally it was suspect that the scanner system would not return an image when the exposure on the phosphor screen was too high to produce a reasonable dental x-ray exposure but further experiments revealed that even after the screen is partially bleached it still will not yield an image and that images from shots that seem to have produced too little exposure have intermittent success in returning an image with this scanner system. The main problem with this uncertainty of how the image is preconditioned is that there doubt as to if the density of the x rays incident on the screen can be determined.

5.17.2 Drivers

The drivers for the QST scanner are not readily available so it became a problem when the computer used to run the scanner stopped working. Temporary drivers and Stella can be used to obtain images in the event that one cannot obtain the full version of the drivers (see appendix F for details).

5.18 Anode ablation and cathode tip wear

Ablation of the anode results in high-temperature splash back of anode material onto cathode surfaces and other surfaces in the vacuum chamber. While many of these surfaces are not harmed by this splash back, the cathode surface in particular (partly because of its close proximity to the anode and partly because of the soft nature of aluminum) becomes worn and rough. The splash back leaves deposits but also erodes away the anodized surface of cathode components. With no anodization and with field enhancements from the pitted wear, the cathode components fail to prevent electron emissions in those locations for subsequent shots. When sufficiently concentrated the energy deposited from the electron beam into the converter will cause vaporization of the anode. In the case of 0.020-inch-thick tantalum converter, the energy-deposition depth lies in the interior of that thickness so that the vaporization in the middle of this sheet of tantalum during a shot ruptures both surfaces (the cathode and anode facing surfaces) of the tantalum outward.

5.18.1 Cathode tip preconditioning

We wanted to ensure the uniform emission of electrons from the cathode terminus.

The cathode tips were conditioned by abrasion via sanding or bead blasting to provide micro field enhancements. While this appears to enhance the emission of electrons it is prone to problems. First, the uniformity of the conditioning is difficult to maintain (i.e. it is difficult to ensure equal density of scratches when sanding and equal density of micro pits resulting from bead blasting over the entire desired emission area. Next, the act of sanding or blasting can alter the overall shape of the cathode tip. Lastly, this preconditioning appears to increase ablation of the cathode tip during a shot.

It was found that the cathode tip could be painted with thinned conductive epoxy which appears to be as effective as the bead blasting. Distilled mineral spirits, ethanol, and acetone were tested as thinners. Acetone was the only thinner tested that resulted in a

smooth mixture free from aggregations of microbeads and is therefore the recommended thinner for future testing. The epoxy contains glass microbeads coated in Ag and the appearance of the bead blasted and epoxy painted tips are nearly identical. It was found that the painting of the tips greatly reduced the ablation of the Al from the cathode tips. The thinned epoxy was not always consistent in its performance particularly it did not always adhere well after the recommended curing conditions were satisfied and at times it was difficult to remove from a cathode tip post shot. The inconsistency in adhesion is likely due to variations in the concentration of the thinned epoxy. We found in most cases heat failure of the epoxy was the easiest mode of removal and was best at preserving the shape and condition of the Al substrate. It is suspected, due to the inconsistent adhesion and the consistent behavior of the cathode tips, that enduring adhesion was not necessary for our purposes. Dipping the cathode tip in an acetone thinned mixture of the epoxy base (the portion of the epoxy containing the microbeads) resulted in a consistent, smooth application of beads that is easy to remove post shot and reduces wear on the cathode tip. When choosing to forego the use of epoxy hardener care must be taken to obtain the appropriate concentration of microbeads for application and to ensure nothing touches the dipped portion before the shot. It appears that the microbead suspension can be used repeatedly by simply reconstituting the suspension with the appropriate amount of acetone prior to dipping the cathode tip. The tenuously applied microbeads are thought to maintain their location on the cathode due to their mass on the timescale of the shot so the microbeads are not suspected to effect the electron beam by populating the A-K gap on the timescale of a shot. Post shot, a portion of the beads are expected leave the cathode tip contaminating the vacuum chamber. Particularly contamination of microbeads on the vacuum insulator is a concern and underscores the need for regular cleaning and inspection of the vacuum chamber, pulse line, and insulator.

Chapter 6

Methods

6.1 Spot size measurement

Measurement of the physical extent of the radiographic spot is important if improvements to the FOM are to be made.

6.1.1 Tungsten rolled edge

With the tungsten rolled edge method of spot size measurement the rolled edge is placed between the radiographic source and the image plate with the apex of the rolled edge on axis with the x-ray beam. The rolled edge is oriented so that the radial direction of the curved surface is in the plane of the axis of the x-ray beam. The shadow from the source is cast upon the image plate. The physical extent of the radiographic source in the vertical direction will dictate the vertical size of the transition between unexposed and fully exposed on the image plate after accounting for the magnification of the setup. The correlated nature of the shadow and temporal extent of the source provides a way to indirectly measure the temporal extent of the source.

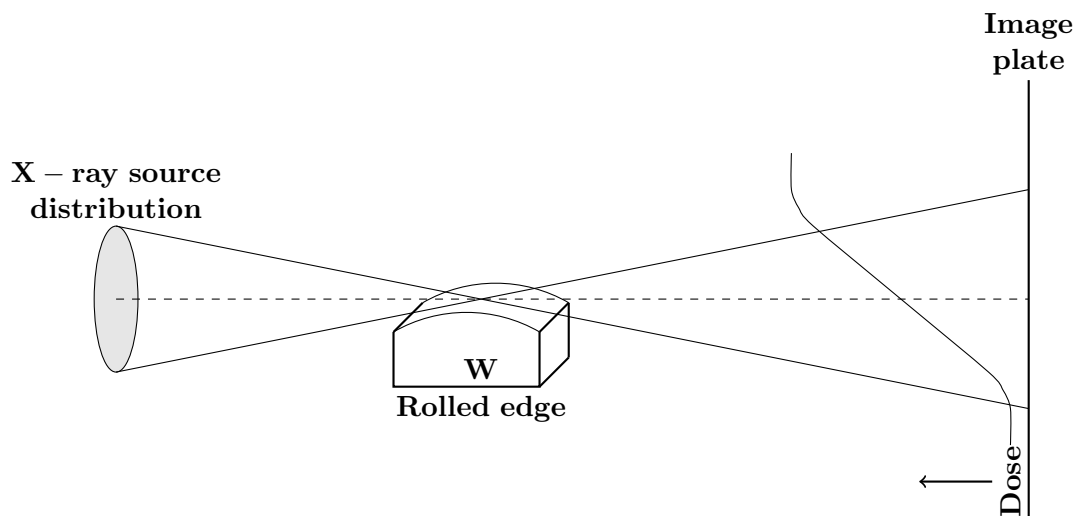


FIGURE 6.1: Schematic diagramming rolled edge set up.

In these experiments the phosphor plate is scanned by a Denoptix QST scanner or a FujiFilm BAS1800II phosphorimage bioanalyzer scanner.

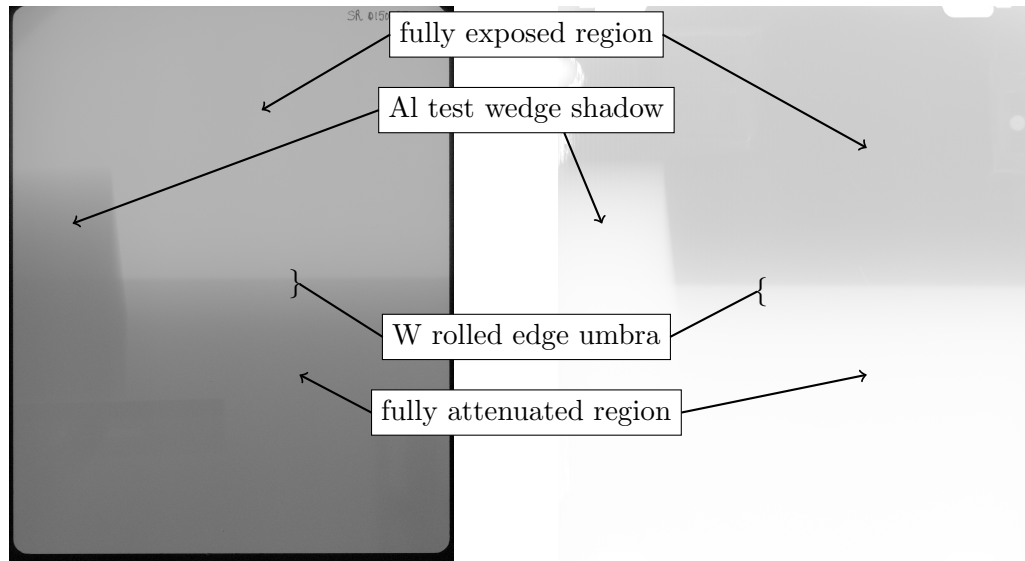


FIGURE 6.2: Radiographs showing rolled edge images from Shot 154 using FujiFilm BAS 1800II (left) and Denoptix QST (right) phosphor screen imaging systems.

The experimental setup described will result in an image similar to that shown in figure 6.2 and include an areas of full exposure and full attenuation separated by an umbra.

The data is analyzed in one of the two following ways.

1. Background subtraction method. This is in my opinion more accurately a description of the core of the spot. Here the line spread function (LSF) often shows a shape that would suggest an addition of two simple distributions—a wider distribution with a more narrow distribution added upon it. It is postulated that the narrower distribution is a description of the core of the spot. In this method we treat the data to subtract out the wider distribution and only consider the narrower distribution observed in the LSF. This method may be neglecting the full width of the spot.
2. Full data treatment. In this method the umbral data is treated in full without any attempt to subtract out any background. When using a rolled edge this method becomes intractable because of the elevated background in the image. The difficulty here is that the grayscale in the image rarely achieves a low enough gradient to confidently identify the grayscale associated with full attenuation of the source from the rolled edge. Alternatively when using an aperture the background in the image plane appears to be low enough that the full attenuation can be readily identified in the phosphor image.

6.1.2 Face plate contact film

During many of the experiments radiographic film was used to obtain a contact image of the flux through the faceplate.

Often the areal dose concentrations from the shots were out of the range of the film and thereby limited the conclusions that could be drawn from them.

Exposure on the film comes from two sources, electrons and x rays. The film only yields one image. The difficulty becomes how to determine what portion of the dose is due to x-ray and what portion of the dose is due to electron fluence, especially since the spectrum of the electron beam is not well known in the system. Therefore predicting the electron fluence through the exterior surface of the face plate becomes problematic.

6.2 Dose measurements

Dose measurements are necessary for the determination of the FOM. The following is a discussion of different aspects of and ways to measure dose.

6.2.1 Optically Stimulated Luminescence (OSL)

Dose measurements were taken using a Landaur OSLD at one meter from the source as measured along the axis when possible. For instance, in experiments where the source is imaged on axis using a pinhole camera the camera prevents full dose from progressing to a meter on axis, therefore the measurement is not possible in this type of experiment.

The dot consists of aluminum oxide crystals embedded in a polymer disk. Exposure to ionizing radiation promotes electrons of the crystal to the conduction band where they find their way to defects in the crystal and are trapped. Later the trapped electrons can be quantified by optical stimulation where a percentage of them are re-promoted to the conduction band and relax back to the original state releasing energy via florescence. The disk containing the crystals is protected from ambient light by an opaque plastic case to prevent bleaching of the electron population in the traps. The amount of photons yielded by florescence are commensurate with the radiation incident upon the dot and through calibration the dose can be calculated.

To calibrate the system I exposed dots to radiation from a 20 Ci Cs-137 source for a time which is calculated to deliver a known dose. The dots were then read by the Landauer reader and the results entered into the calibration settings. The Landauer

software calculates the calibration curves and with the right settings applies the resulting calibration factor to subsequent readings. See appendix B for more details on calibration.

6.2.2 PIN diode

When possible dose measurements were also taken using PIN diodes.

6.2.2.1 Calibration of PIN diodes

Shot 87 featured a 1" anodized aluminum ring diode, an anode-cathode gap of 2.2", two 0.010" sheets of Ta, and a 1/4" Al faceplate. Two pin diodes placed at 95" off center, with 200-V bias, and an OSL at 1m on axis were used to measure the x-ray pulse (Figure 6.5). For context below is a plot of the voltage, current, and calculated impedance at the diode (Figure 6.3) as well as a plot of the raw signal from the pin diode (Figure 6.4a).

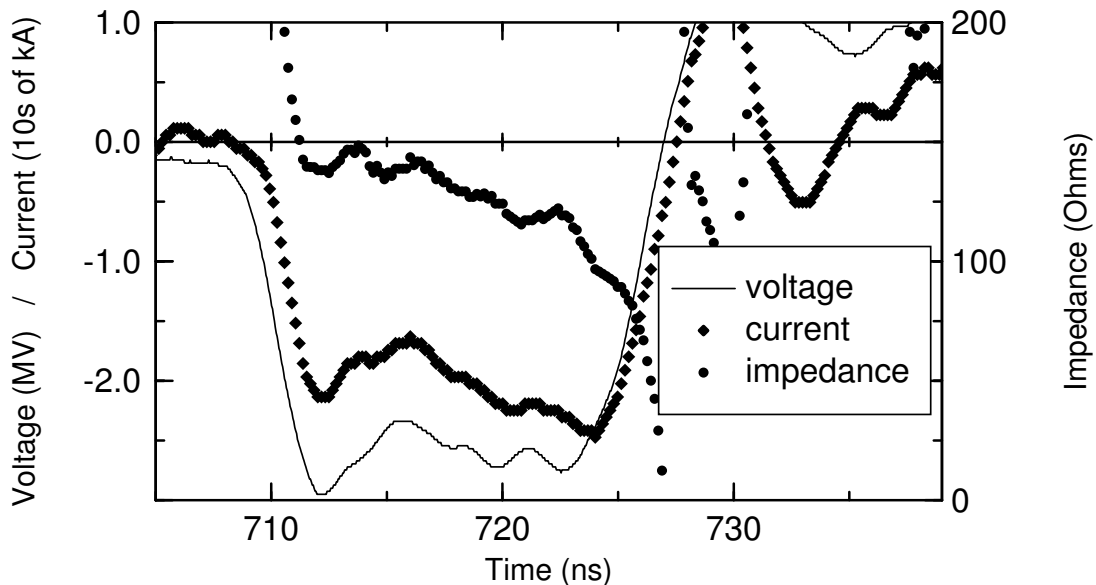


FIGURE 6.3: Voltage (measured), current (measured), and impedance (calculated from voltage and current) of the diode for the duration of shot 87.

The dose rate is calculated by performing the following steps.

1. The signal is corrected for the effects of the PIN diode setup. This includes effects of the cable and the bias T which is necessary for PIN diode operation.
2. The baseline is subtracted from the pin diode signal (see figure 6.4b).

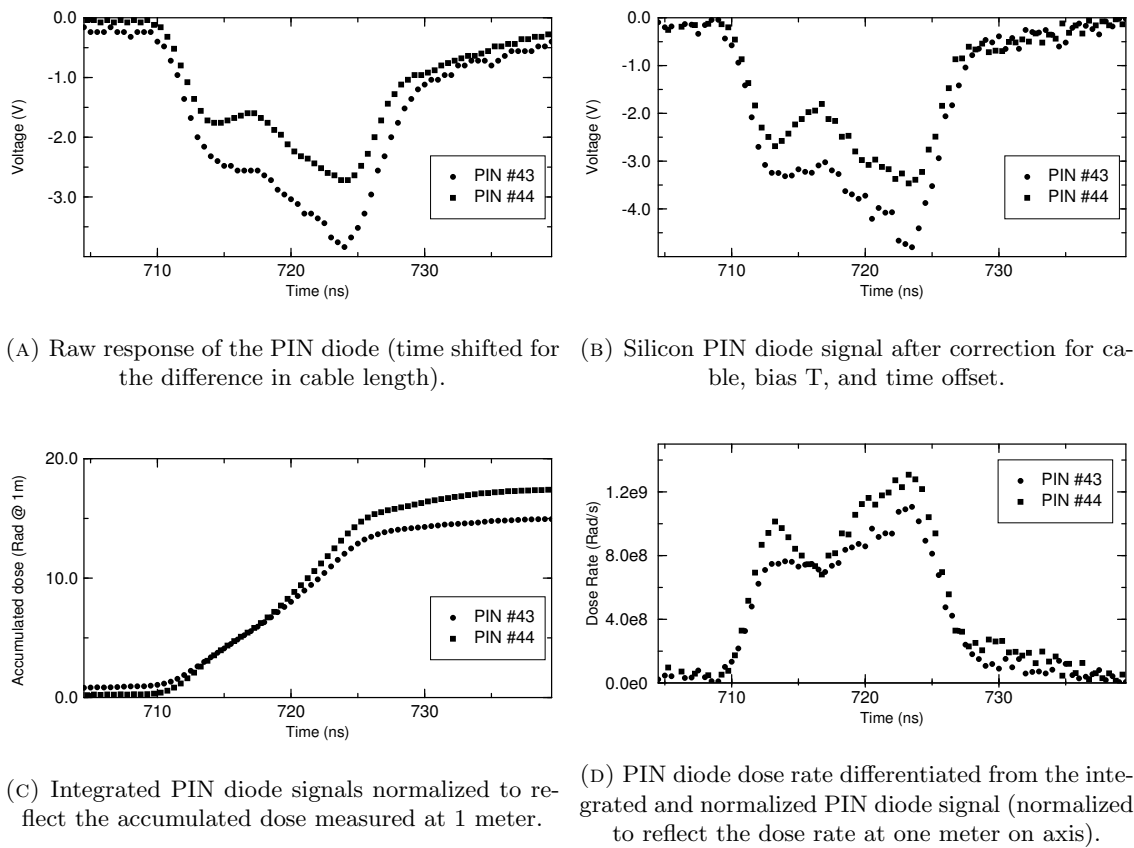


FIGURE 6.4: Silicon PIN diode signal evolution throughout the calibration process (shot 87 shown).

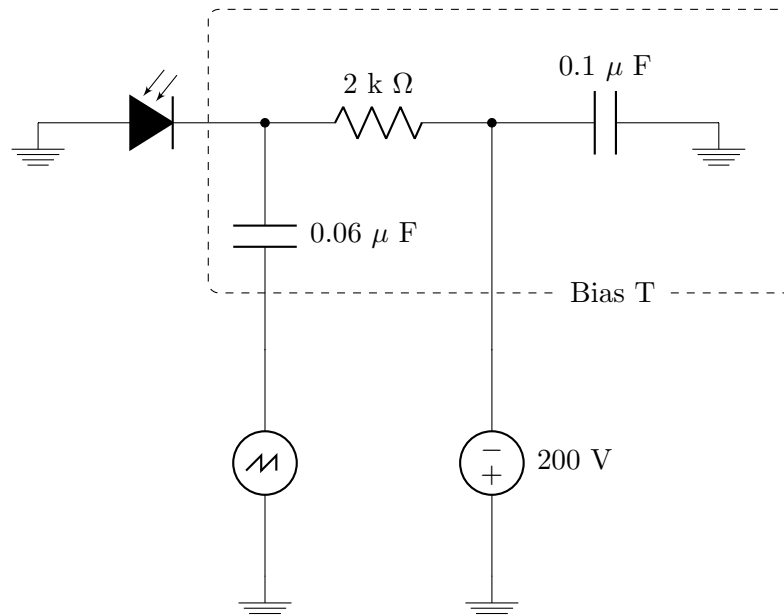


FIGURE 6.5: Schematic of the PIN diode set up to ensure operating voltage.

3. The trace is integrated over time to yield a signal proportionate to accumulated dose.

4. The trace is normalized to the dose observed at the location of interest. In this case (shot 87) the OSL at 1m on axis read 18.7 Rad (figure 6.4c).
5. Lastly the trace is differentiated with respect to time. The result is a dose rate description at one meter on axis for shot 87 (figure 6.4d).

The Stella macro performing this operation can be specified in this way (figure 6.6).

	En	Routine	Option	Trace	Result	a	b	Comment
2	<input checked="" type="checkbox"/>	Tr Param	Trace	PIN43	PIN43t	42e-9		time shift for pin44
3	<input checked="" type="checkbox"/>	Filter	Cbl cor	PIN43t	pin43c	RG223	127	R=2kOhm, C=0.06e-6F
4	<input checked="" type="checkbox"/>	Filter	RCCorr	pin43c	"	3e-6		corrections for coax cable effects
5	<input checked="" type="checkbox"/>	Bline Foot	LS fit	pin43c	pin43bl	"\st+50e-9	"\st	adjust for base line
6	<input checked="" type="checkbox"/>	Filter	Integr	pin43bl	pin43int			integrate trace
7	<input checked="" type="checkbox"/>	1TrMath	Norm	pin43int	pin43norm	-pin43int\mn/18.7	pin43int\mn/18.7	normalize for dose
8	<input checked="" type="checkbox"/>	Filter	Differ	pin43norm	DsRtPin43	0	Bin	differetiate for dose rate

FIGURE 6.6: Stella macro detail for PIN diode data processing.

Notice the OSL at 1m read 18.7 Rad for shot 87 and this value is hardcoded into the macro. I suggest for portability of the macro between shots that the dose recorded by the OSL be included in the Stella data set and called from the data set as opposed to hard coding the value in the macro.

The timing of the traces can be a problem. The images above imply that the signal from the pin diode is observed before the voltage pulse arrives at the diode. This is explained by the fact that the PIN diode signal travels a longer distance (the cable is longer) and the photons from the source must travel to the PIN diodes than the cable distance the voltage and current diagnostic signals must travel. These cable lengths and must be noted so the signals can be synchronized appropriately.

See Appendix C for further details on the calibration of the PIN diodes.

6.3 X-ray spectrum

An aluminum test wedge was placed between the radiographic source and the phosphor screen to cast a shadow with information on the penetrating nature of the x rays. While this may not be sufficient to determine the spectrum, the image will contain information about the spectrum sufficient to substantiate or disprove a hypothesized spectrum through attenuation/transmission simulations or calculations.

6.4 Current diagnostics

Essential to the understanding of the TriMeV system and its effects is a clear understanding of the current in the pulse line. This is achieved through the B-dot device.

6.4.1 B-dot

B-dots are the instruments used to measure current at the diode and through the vacuum line. When current flows through the vacuum line or the diode a magnetic field is generated and the coils of the B-dots are positioned to contain a portion of the subsequent magnetic flux. From the flux an EMF arises in the coil and the resulting current is monitored and recorded as the current of interest (after the calibration factor has been applied).

There is a concern that we may not know the current well. Two notable factors are at play here. One is that the B-dot only samples the magnetic field from the current at a discreet location. There is a possibility that for one reason or another that particular location is not characteristic of the magnetic field as a whole. The second is that the current in the A-K gap is not only from the motion of electrons but also arises from motion of ions in the gap. While the full current (from both electron and ion motion in the gap) is an appropriate description (because all gap current dictates the intensity of the Bennett pinch), if one is interested in using the current to calculate an effect dependent on the electron beam, it would be appropriate to scale the current to discount the current from ion motion.

6.5 Electron beam diode voltage

Together with the diode current, the voltage gives insight into the properties of the diode. For instance, one can calculate the power output of the diode by multiplying the voltage and the current. Additionally the relative dose can be calculated by multiplying the current by the voltage squared [24].

6.5.1 D-dot

D-dot devices detect the voltage on a complementary facing surface. The D-dot is an electrically isolated plate of metal that acts as one plate in a capacitative system. In this system, when charge is present on the complementary surface, i.e. the surface of

the pulse line, an amount of charge is induced on the plate in the D-dot. This presence of charge is detected and by applying a calibration factor the voltage at the pulse-line surface can be inferred.

Chapter 7

Cathode sleeve experiment

In this experiment we begin with a self magnetically pinched (SMP) diode with an aluminum cathode tip having a 1.25-cm outer diameter and a 1.00-cm inner diameter. The cathode tip is polished with the exception of the surface within 5 mm of the tip which is bead blasted to encourage electron emission. A polyethylene sleeve is slip fit to the cathode tip so that virtually any position of the sleeve along the cathode is possible. The sleeve is 7.6-cm long end-to-end with an outer diameter of 2.6 cm. The position of the sleeve is the variable for this set of experiments while the spot size and the dose are monitored to investigate the effect of the sleeve position on the spot size. The position of the sleeve along the cathode is specified by the reveal which is defined as the distance from the tip of the cathode to the tip of the sleeve. For instance a positive reveal means the cathode protrudes out from the sleeve into the A-K gap and for a negative reveal the sleeve extends further into the gap than the cathode tip. The A-K gap (the distance from the tip of the aluminum cathode to the converter mounted on the anode) is 3.3 cm.

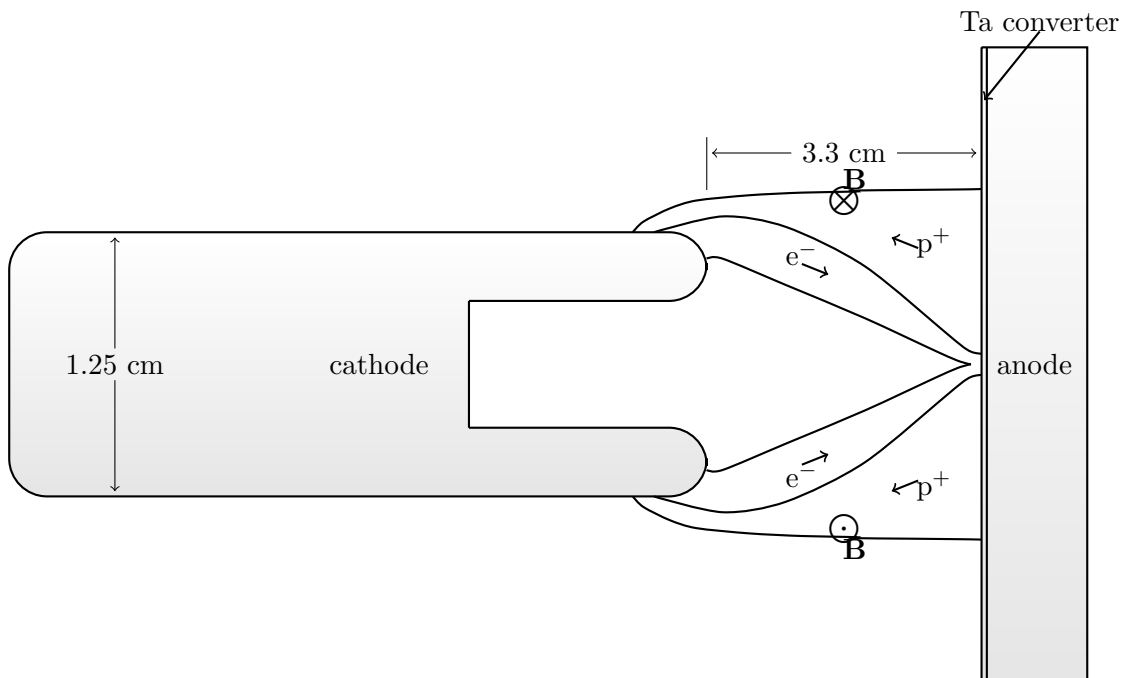


FIGURE 7.1: Sketch of expected electron and ion plasma for a SMP diode late in the shot after the diode has shorted out from the ion plume closing the A-K gap. The general shape of the electron beam is patterned from current distributions from PIC simulations in literature [2].

7.1 Cathode sleeve effects on the electron beam

It has been illustrated in literature that the 3-MV electron beam incident on surfaces in the vacuum chamber result in plasma expanding from the surface [10, 25]. Typically the anode plasma travels at a rate of 5 cm in a μs [26]. The ion plasma blowing off the surface of polyethylene structures is expected to contain hydrogen, carbon, and oxygen ions, in order of concentration. In this list I have accounted for polyethylene content, most hydrocarbon contaminants likely to be on the surface, and previously absorbed contaminants into the surface of the polyethylene (namely atmospheric nitrogen, oxygen, and water).

The presence of ion plasma within the negative reveal of the cathode sleeve will work to restrict and partially neutralize the electron beam coming from the cathode. This implies that sleeve has a limited effect in collimating the electron beam while reducing the diameter of the effectual emission area of the cathode. The more highly collimated electron beam shown in figure 7.2 is expected to reduce the illuminated anode area and may reduce the Bennett pinch effect near the anode due to a smaller plasma at the anode.

Due to the fact that the sleeve surface is in near proximity to the cathode the effect of plasma from the sleeve is likely to have an early onset in the life time of the shot since the plasma source is near the emitting cathode tip. Additionally the proximity of the sleeve contained plasma to the cathode tip does not short out the diode (at least not initially) so the high-density plasma persists near the cathode tip early in the shot while there yet remains time in the pulse before the diode will short out due to dense plasmas closing the A-K gap. In this way it appears that shorting of the diode due to ion plasma is avoided while maintaining the benefit of plasma-driven electron-beam collimation.

7.2 Cathode sleeve effects on the spot size

I wanted to investigate the effect of a cathode sleeve position on the radiographic source spot size and dose to see if the spot size could be reduced as a function of the polyethylene cathode sleeve position. In figure 7.3 is a plot of the spot size (blue for the FWHM of the LSF or red for the 25-75 % distance both read from the left axis) and the sleeve reveal (green read from the right axis) as a function of shot number. Shots 138-140 and 153 with the SMP diode (no cathode sleeve) and are included for comparison.

In an effort to characterize the SMP diode in terms of spot size I have calculated the deviation from the mean for shots 138-140 and 153. If my model of the plasma flowing

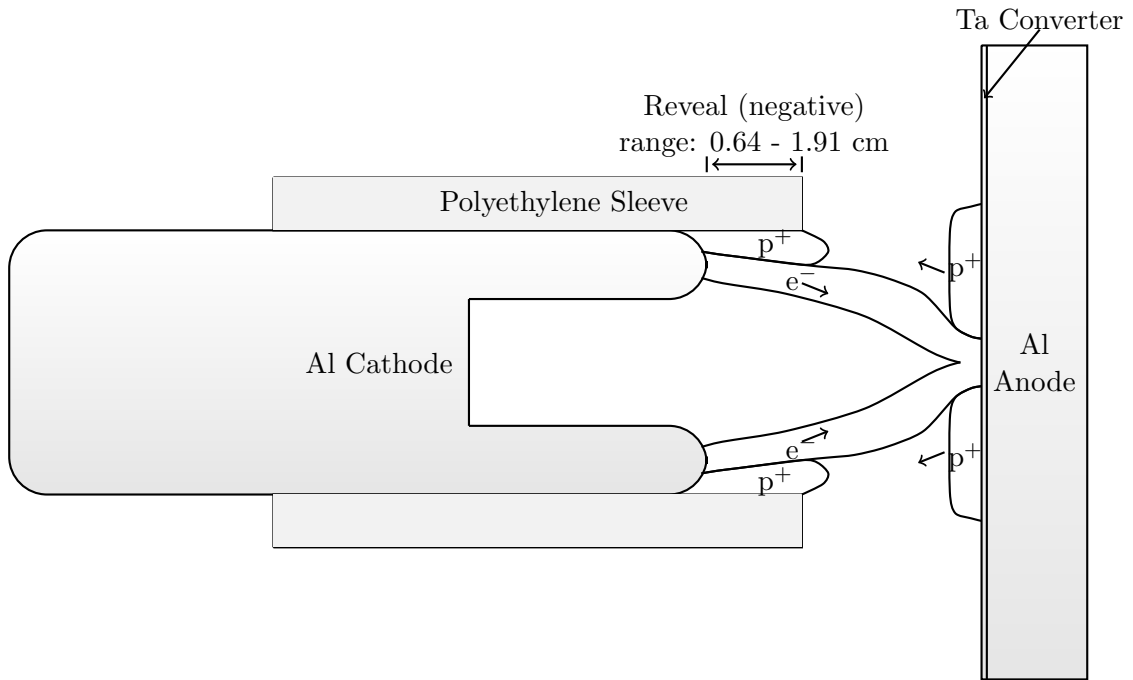


FIGURE 7.2: Sketch of hypothesized electron beam and plasmas for a SMP diode with a negative-reveal sleeve early in the shot before the plasma has shorted the diode.

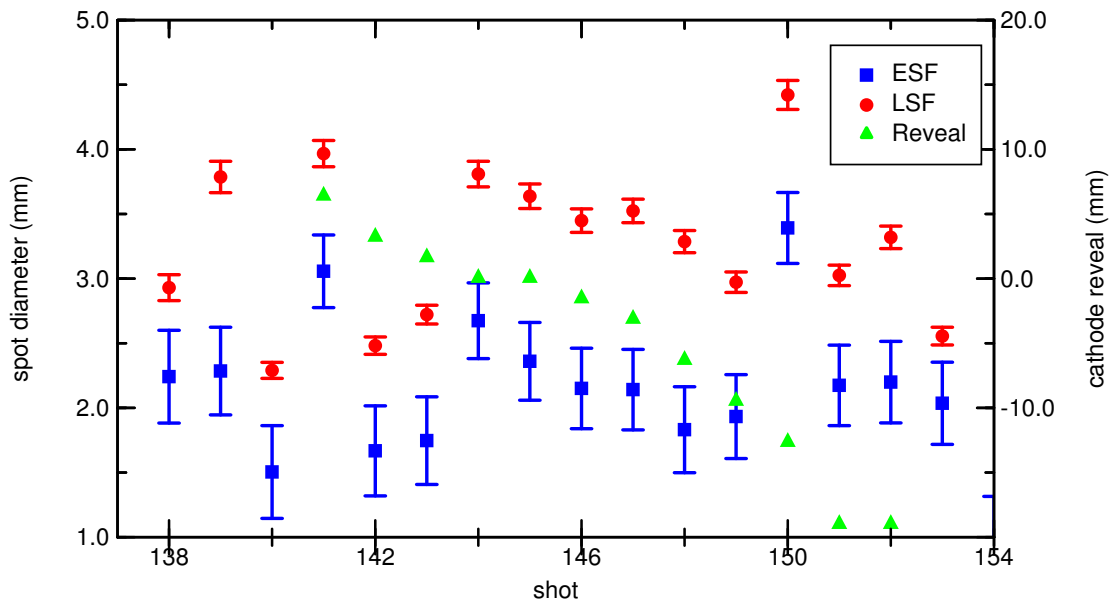


FIGURE 7.3: Spot size and cathode sleeve reveal by shot number.

off the interior surface of the cathode sleeve is the dominating factor in this series of experiments one would expect little difference in the behavior between the diode with no sleeve and the diode with a sleeve having a positive reveal since in the positive reveal configuration there is no interior sleeve surface exposed to the emitted electrons in the vicinity of the cathode tip that generates a plasma. I have also calculated the deviation from the mean for shots 141-143 as well as shots 138-143 and 153 together. Least square

TABLE 7.1: Statistics calculated on the LSF FWHM spot diameter vs reveal (P) for the cathode sleeve experiments.

Shot Range	Description	Mean Diameter (mm)	Standard Deviation (mm)
138-140, 153	no sleeve	2.89	0.565
141-143	$P > 0$	3.05	0.651
150-152	$P < -9.5$ mm	3.59	0.600
138-143, 150-153	no sleeve, $0 < P < -9.5$ mm	3.15	0.671
138-153	all shots	3.26	0.573
141-152	with sleeve	3.38	0.520
144-152	$P \leq 0$	3.49	0.414
144-149	$0 \geq P \geq -9.5$ mm	3.44	0.265
Shot Range	Description	R ² (mm)	Average Deviation from regression (mm)
144-149	$0 \geq P \geq -9.5$ mm	0.905	0.0000673
144-152	$0 \geq P$	0.063	0.00161
141-152	with sleeve	0.0007	0.00270

linear fits were calculated for the shot sets in the second part of table 7.1 by plotting the spot diameter vs the sleeve reveal. The respective R² value and average deviations from the fit are included. Similar treatment of other data sets are not included since the other data sets lack sleeve reveal which is needed as an independent variable when investigating correlation between sleeve reveal and spot size.

7.3 Conclusions on the spot diameter as a function of reveal

Drawing a conclusion about the effect of increasing negative reveals on the spot size diameter cannot be recommended without risk. More shots are needed to reveal the effect of shot to shot variations and diode hardware ablation on this experiment. However, this data leaves room to consider the following possibilities.

- The broad deviation and similar mean diameter values in shots without a cathode sleeve (138-140 and 153) suggest there is little effect on the spot size when the cathode sleeve is positioned with a positive reveal.
- The comparatively small deviation from the least squares fit for sleeve reveal between 0 and - 9.5 mm suggests the sleeve has an effect in reducing the variation in spot size within a range of sleeve reveals. If this is the true influence of the sleeve it could be used in future designs to reduce shot to shot variation in spot size.

- Continued reduction of negative sleeve reveals beyond -9.5 mm reintroduces the broad deviation in spot size similar to the deviations where the sleeve is in positive reveal or not present.
- Diodes with a prescribed sleeve reveal range may reduce instabilities in the plasmas associated with the shot.
- The return of a broad distribution of spot sizes with a reveal less than than -9.5 mm, similar to shots with little expected effect, suggests that there are competing effects that contribute to a less stable electron beam.
- There is a lower limit to the spot size that can be achieved with a certain sleeve reveal when applied to an SMP diode with a planar anode.
- A cathode sleeve alone is insufficient to reduce the size of the spot below the most focused shots without a sleeve as seen in the data that the shots with the sleeve have a higher average spot size than shots without.

The more highly collimated electron beam shown in figure 7.2 is expected to reduce the illuminated anode area and may reduce the Bennett pinch effect near the anode due to a smaller plasma at the anode, which is suggested by the fact that while the spot diameter is reduced with a decrease in sleeve reveal, smaller spot sizes are observed without any sleeve at all. The sleeve also prevents the early expansion of the electron beam from the cathode by collimation.

The presence of a plasma within the negative reveal of the cathode sleeve will work to restrict and partially neutralize the electron beam coming from the cathode but appears to have only a mild effect on the size of the source.

It is likely the position of the sleeve affects the focus of the electron beam in the A-K gap. So while these experiments were performed with the ideal gap width based on current and voltage diagnostics for the SMP diode without sleeve the ideal focal length may change with sleeve position meaning the a different A-K gap for each sleeve position may be needed to achieve the optimized spot size.

7.4 Dose effects

For the cathode sleeve series of experiments the dose was measured at one meter as inferred by x-ray PIN diodes and directly by OSLDs. The data from these measurements is plotted as a function of shot number in figure 7.4 as a function of shot number.

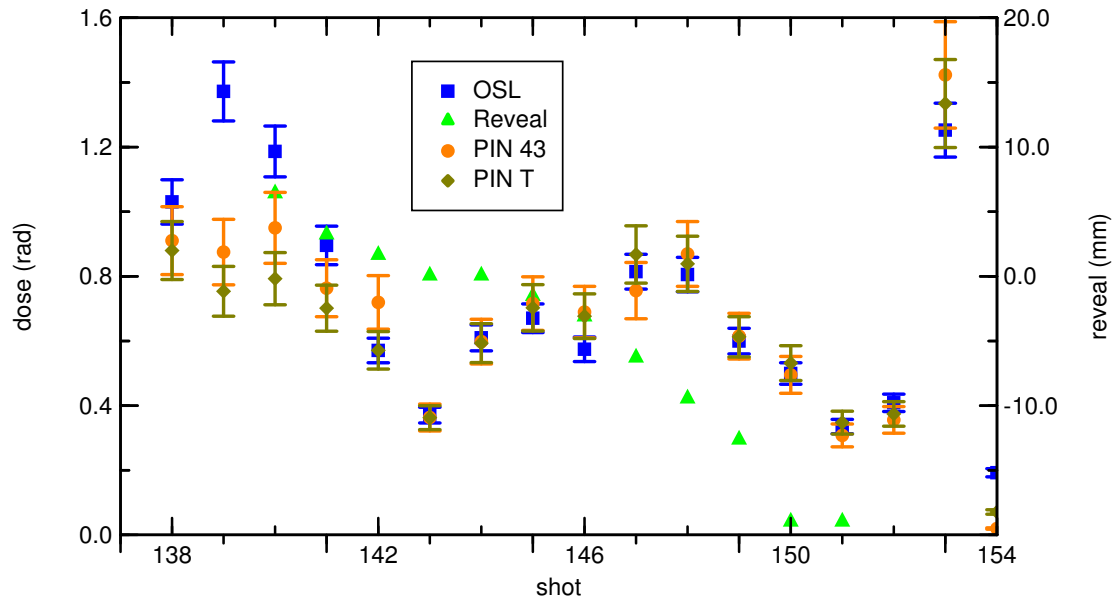


FIGURE 7.4: Dose and cathode sleeve reveal vs shot number.

TABLE 7.2: Statistics calculated on the dose measured on axis at 1 meter from the source, as inferred from PIN 43, as a function of reveal (P) for the cathode sleeve experiments.

Shot Range	Description	Mean Dose (rad)	Standard Deviation (rad)
138-153	all shots	0.713	0.267
138-140, 153	no sleeve	1.04	0.223
141-152	with sleeve	0.667	0.276
141-143	enlarged emission area	0.615	0.179
143-148	e-beam collimation	0.665	0.157
148-152	ion plume constriction/instabilities	0.528	0.202
Shot Range	Description	R^2	Average Deviation from regression line (rad)
141-152	with sleeve	0.369	0.0195
141-143	enlarged emission area	0.668	0.0107
143-148	e-beam collimation	0.736	0.00653
148-152	ion plume constriction/instabilities	0.929	0.00288

To characterize the dose for this series of SMP diode experiments I calculated the mean and standard deviations of groups of shots classified by diode behavior, namely by increase or decrease of dose, shown in table 7.3.

I issue the same caution with this dose data as with the spot size data in that concluding the dose increases with a decreasing reveal in the range of 0 to -9.5 mm cannot be recommended without risks. More experiments are needed to gain a sense of the effect

over shot to shot variations but as before, given the nature of the data, the following possibilities exist.

- For decreasing reveals between 0 and -9.5 mm the effective area of ion plume from the interior surface of the sleeve increases (so presumably also the ion population increases) yet the dose measured at 1 meter on axis increases. It is possible that the ions from the interior surface of the sleeve flow toward the cathode due to the electric field and increases the current near the cathode tip which should act to further focus the beam near the cathode tip as explained by the Bennett effect.
- Mismatch in dielectric between the vacuum and the polyethylene equates to a discontinuity in the normal component of the electric field at the boundary which increases the chance of arcing along the face of the sleeve. This enlarges the effective electron emission area reducing the brightness of the spot and thereby reducing the dose. The effect is magnified as the sleeve face is positioned over areas where greater numbers of electrons are emitted for a given area as seen in the decreased of dose as the reveal decreases from 6.35 to 1.59 mm in shots 141 to 143.
- When the sleeve face is no longer contiguous to the surface of the cathode (reveal ≤ 0) the probability of arcing along the sleeve face is greatly reduced.
- The collimation effect of the sleeve grows with decreasing reveals (from 1.59 to -6.38 mm) observed as an increase in dose for shots 143-148.
- For continued reduction of reveal (from -6.38 to -19.05 mm) the ion plume may work to constrict the electron beam and increase instabilities in the electron beam affecting its focus and thus affecting the dose measured. The fact that the dose increases for one range of reveals yet decreases for another range suggests competing effects and an ideal reveal to maximize dose.

7.5 Effect on figure of merit

Folding the dose and the spot size together in the figure of merit will yield a metric to quantify the effect on image quality potential as a function of sleeve reveal. Here I have taken the LSF FWHM for the spot size (s) and both the OSLD and the PIN 43 dose (D) measurements to calculate the figure of merit

$$FOM = \frac{D}{s^2}. \quad (7.1)$$

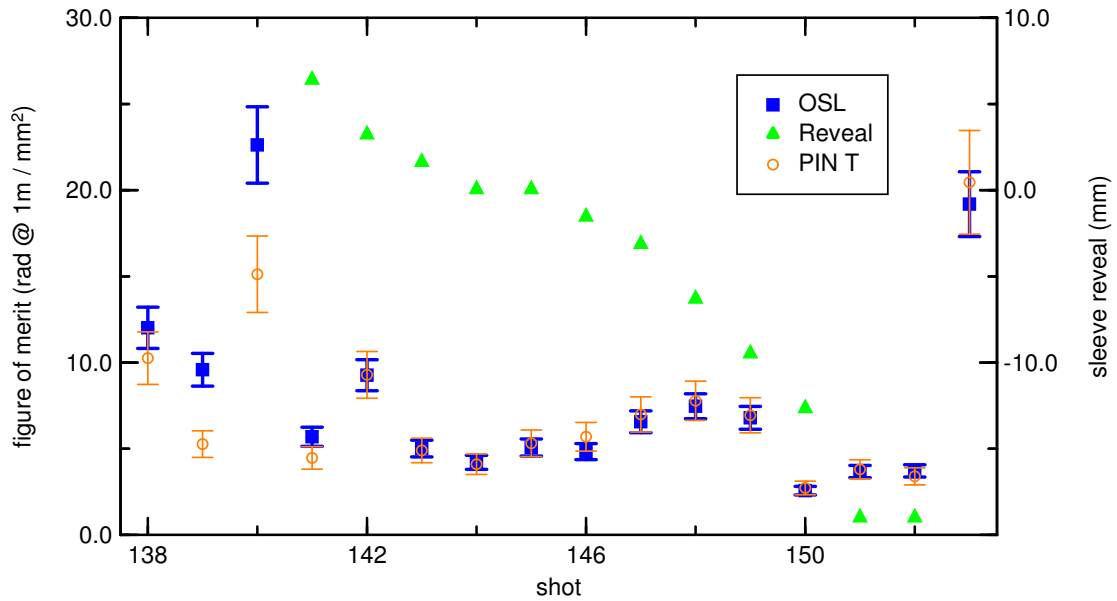


FIGURE 7.5: Figure of merit as calculated from OSL measured dose (squares) and from PIN T signal (open circles) and cathode sleeve reveal (triangles) by shot number. Here FOM is read from the left scale and the reveal from the right.

TABLE 7.3: Statistics calculated on the FOM calculated from dose, as inferred from PIN 43, and the LSF FWHM spot diameter for the cathode sleeve experiments.

Shot Range	Description	Mean FOM (rad@1m/mm ²)	Standard Deviation (rad@1m/mm ²)
138-153	all shots	17.5	13.0
138-140, 153	no sleeve	34.0	14.1
141-152	with sleeve	11.9	6.09

In effort to quantify the FOM data I have calculated the mean and standard deviation for groups of data points based on the distribution of FOM value.

The presentation of this data comes with a similar caution that more shots are needed to resolve the nature of the system above the shot to shot variation but possibilities which have not been ruled out by the nature of this data are listed below.

- The largest FOM is observed for a shot without a sleeve suggesting that the effect of the sleeve alone may not be sufficient to produce the highest possible FOM.
- The tighter distribution in FOM for shots 144 thru 153 in comparison all others suggest there is an ideal operating range in reveal when one desires a more predictable or maximized FOM with a sleeved SMP diode.

Chapter 8

Anode shroud experiment

These tests come in a series of experiments that featured a large (5 inch radius) planar Ta converter covered by a large (5 inch radius) planar shroud with a bore in the middle to expose the converter. The shroud and the converter are independently mounted in this first setup allowing the comparison between no shroud and with shroud configurations. The draw back is the large Ta converter that is required which at these energy densities is not expected to survive the shot. The cathode tip used was a 1 inch diameter anodize aluminum ring tip.

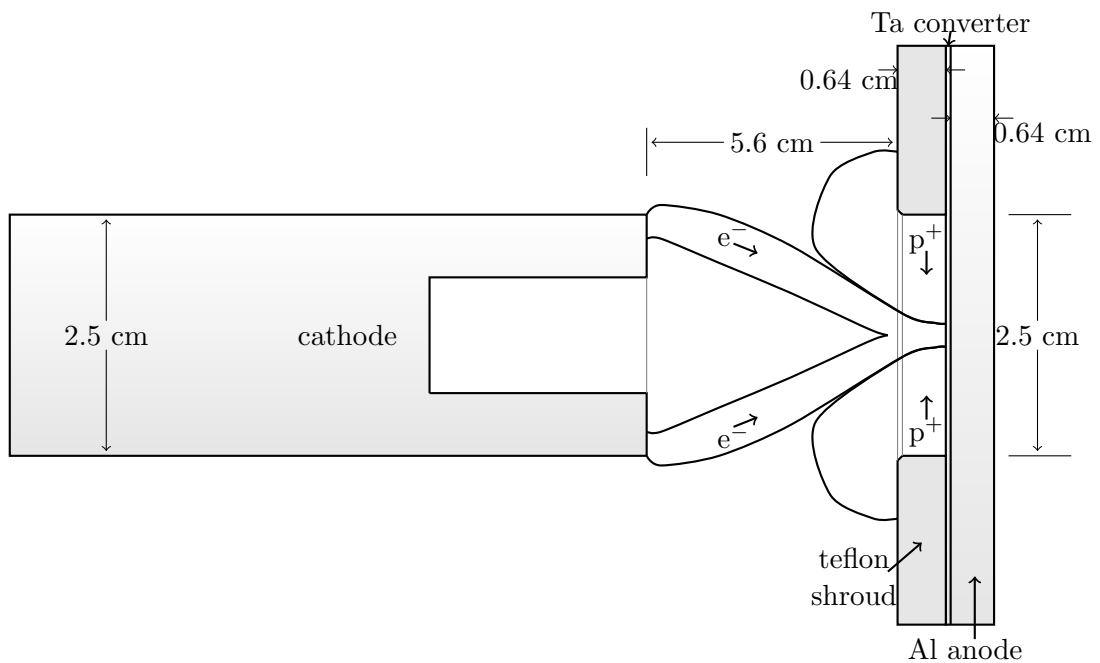


FIGURE 8.1: Sketch of planar anode shroud showing electron beam and expanding plasma for a 1 inch aluminum ring diode.

8.1 Anode shroud effects on the electron beam

The shape of the anode shroud gives a surface concentric to the axis of the diode from which plasma can be blown off to constrict the electron beam. The choice of material of the shroud also provides the possibility to change the main constituents of the ion plume.

8.2 Planar anode shroud experiments

8.2.1 Effect on the spot size

Originally it was suspected that the presence of an anode shroud would reduce the spot size. My objective was to quantify the effect. A 2-inch-thick lead aperture (1/2 inch diameter bore) was used to image the umbra cast from the source from which the source spot size can be inferred. I did not attempt to subtract background of any kind simply the radial ESF derived from the raw image and the resulting LSF were used to indirectly measure the spot size.

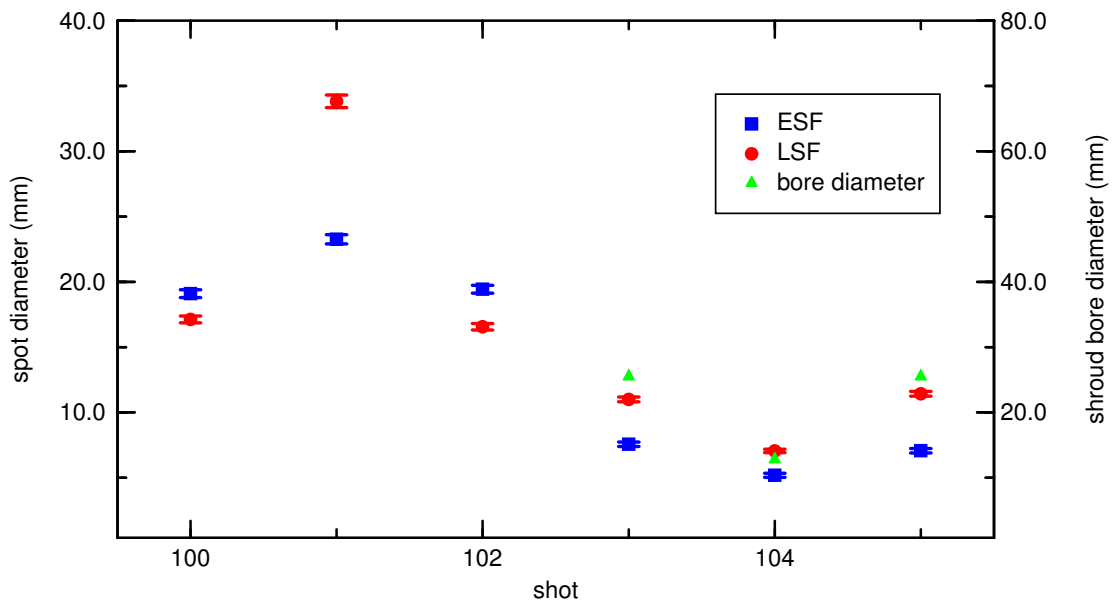


FIGURE 8.2: Spot size and shroud aperture diameter vs shot number.

Notably there was suggestion in the phosphor screen image from shot 101 that the phosphor screen may have been saturated which would give us no 100% exposure reference in the image which could skew the measurement. No such evidence was noted for any of the other shots. Shots 100-102 are without a shroud where shots 103 and 104 featured a 1/4 inch thick teflon shroud and 105 a 1/2 inch thick polyethylene shroud. The inside corners of the bores were chamfered to a depth of approximately 1 mm.

8.2.2 Suggestions from the spot diameter

More shots are needed to produce statistics on reliability and to determine the effect of shot to shot variation but the data suggests the following behavior.

TABLE 8.1: Statistics calculated on the LSF FWHM spot diameter for the anode shroud experiments.

Shot	Description	Spot Diameter LSF (mm)	Spot Diameter ESF (mm)
100	no shroud	19.1	17.1
101	no shroud	23.2	33.8
102	no shroud	19.4	16.6
103	teflon, 1 " diameter bore	7.55	11.0
104	teflon, 1/2 " diameter bore	5.17	7.04
105	Polyethylene, 1 " diameter bore	7.05	11.4

Shot(s)	Description	Mean Spot Diameter LSF/ESF(mm)	Mean Spot Diameter LSF/ESF(%)
100-102	no shroud	20.6/22.5	100/100
103-105	with shroud	6.59/9.81	32.0/43.6
103, 105	1" diameter bore	7.30/1.12	35.5/49.8
104	1/2 " diameter bore	5.17/7.04	25.1/31.3

- The x-ray spot size is reduced with the use of an anode shroud evidenced by the lower mean spot size for shots 103-105 compared to the mean spot size of shots 100-102.
- A reduction in spot size is observed for reduced anode shroud bore diameter as shown in the reduction of the spot size in shot 104 when compared to shots 103 and 105.
- The fact that reducing the bore diameter by half did not reduce the spot diameter by half suggests that the restriction of the electron beam is not solely dependent on the size of the bore diameter to dictate the restriction. It is likely the ion plume off the surface of the shroud plays a major role in the e-beam restriction.
- If the expanding plasma is the dominating factor I suspect there is a limit to the smallest time-integrated spot size possible by constriction of the beam via the use of an anode shroud. The size of the beam on the converter will be governed by the balance of forces at the electron beam-plasma interface. The force radially inward is a combination of the plasma pressure and the magnetic pressure and is balanced against the force radially outward described by the Coulomb repulsion. As these balanced forces become stronger (as in the case of increasingly smaller shroud aperture sizes) small anomalies will have a larger effect on the stability of the position of the electron beam on the converter. Additionally, increasing these balanced forces will have an effect on the inherent vibrational frequency of the interface and could spoil the positional stability of the electron beam at the converter preventing further reduction in the time-integrated spot size.

8.2.3 Planar shroud dose effects

In the planar anode shroud experiments the dose was measured by silicon pin diodes and OSLDs. I have plotted this data in figure 8.3 as a function of shot number and have included the diameter of the bore in the shroud. It should be noted during shot 102 problems with the PIN diode setup lead to unreliable dose data which brings the data point into question.

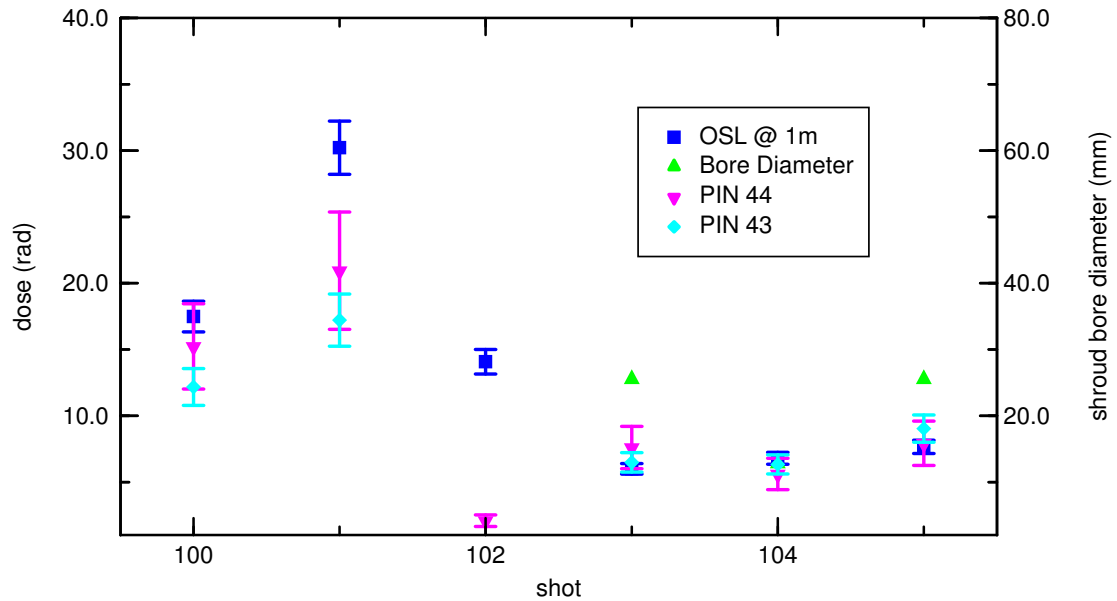


FIGURE 8.3: Dose and anode shroud aperture diameter as a function of shot number.

To characterize the dose for this series of planar anode shroud experiments I calculated the mean and standard deviations of shots grouped by shroud specifications shown in table 8.2.

Care must be taken when drawing any conclusion from this data due to the small sample size presented here. More shots are needed to characterize the effects of shot to shot variation and diode hardware oblation to better understand how these effects influence the data but given the nature of the data, the following possibilities exist.

- There is an appreciable decrease in dose (by approximately 1/2) with the addition of a planar anode shroud which is not surprising when considering the possible effects of the expanding plasma on the space charge near the electron beam.
- The dose, while decreased, appears to be more predictable given the reduction in standard deviation between the with shroud and without shroud data sets.
- The dose may not be noticeably reduced with a reduction in shroud bore diameter as seen by comparing the data for 1 inch and 1/2 inch bore diameters.

TABLE 8.2: Statistics calculated on the dose measured on axis at 1 meter from the source for the planar anode shroud experiments. Shot 102 PIN diode measurements classified as outliers (O) and not included in statistics.

Shot	Description	OSL Dose (rad)	PIN 43 Dose (rad)	PIN 44 Dose (rad)
100	no shroud	17.470	12.162	15.218
101	no shroud	30.200	17.203	20.932
102	no shroud	14.060	0.445 ^O	2.077 ^O
103	teflon, 1 " diameter bore	5.990	6.469	7.587
104	teflon, 1/2 " diameter bore	6.780	6.313	5.601
105	Polyethylene, 1 " diameter bore	7.650	9.015	7.917

Shot(s)	Description	OSL Mean/St Dev (rad)/(rad)	PIN 43 Mean/St Dev (rad)/(rad)	PIN 44 Mean/St Dev (rad)/(rad)
100-102	no shroud	20.577/6.946	14.682/2.521 ^O	18.075/2.857 ^O
103-105	with shroud	6.807/0.678	7.266/1.239	7.035/1.023
103,105	1" diameter bore	6.820/0.830	7.742/1.273	7.752/0.165
104	1/2 " diameter bore	6.780/ n/a	6.313/ n/a	5.601/ n/a

8.2.4 Effect on figure of merit

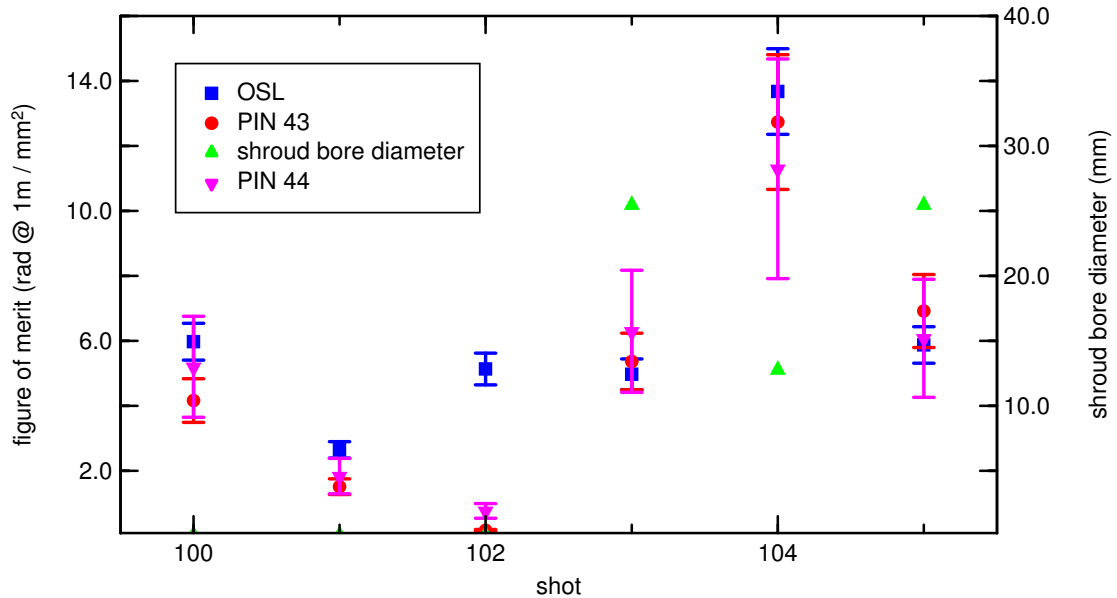


FIGURE 8.4: Figure of merit as calculated from OSL measured dose (squares), PIN 43 signal (circles), and PIN 44 output (down pointing triangles) with the planar anode shroud bore diameter (up pointing triangles) by shot number. I have used the LSF FWHM description of the spot size and FOM is read from the left scale and the shroud bore diameter from the right.

Here I have calculated and plotted (figure 8.4) the FOM as with the previous experiment to quantify improvement to the quality potential, in terms of radiography, that has been

TABLE 8.3: Statistics calculated on the FOM for the anode shroud experiments. The PIN diode determined dose data from shot 102 is a suspect outlier (^O). To exclude it from the mean and standard deviation calculations only the OSL based data has been used.

Shot	Description	OSL FOM (rad @ 1m / mm ²)	PIN 43 FOM (rad @ 1m / mm ²)
100	no shroud	5.97	4.16
101	no shroud	2.64	1.50
102	no shroud	5.13	0.162 ^O
103	teflon, 1" diameter bore	4.97	5.36
104	teflon, 1/2" diameter bore	13.7	12.7
105	polyethylene, 1" diameter bore	5.87	6.92

Shot(s)	Description	FOM Mean (rad @ 1m / mm ²)	FOM Std. Deviation (rad @ 1m / mm ²)
100-102	no shroud	4.58	1.41
103-105	with shroud	8.17	3.91
103, 105	with shroud, 1" diameter bore	5.42	0.45
104	with shroud, 1/2" diameter bore	13.7	

made with the addition of a planar anode shroud. The figures in table 8.3 are meant to characterize the FOM statistically in relation to the shroud used.

The sample population of this data is too small to claim a high confidence in the suggestions found in the data. More shots are needed to determine if the nature of the data is characteristic of these diode features or if variation from shot to shot is responsible for the nature of these measurements, nevertheless, I have included below a list of the possibilities this data seems to suggest.

- The FOM for shots with a shroud increases the figure of merit over shots without.
- The FOM increases dramatically as the shroud bore decreases. This means that the use of an anode shroud can improve the quality of radiographs produced by this system.

Chapter 9

Anode field enhancements

Field enhancements at the anode are possible when one is willing to abandon a planar anode which is not a new idea [2, 7, 27]. Limited experiments have been conducted on the TriMeV system at the Idaho Accelerator Center involving a non-planar anode. In fact, the smallest spot size observed at the Idaho Accelerator Center on TriMeV involved a anode with a 1 mm diameter copper pin protruding from the anode 2.5 mm.

The point of these tests was to investigate the ability of a conducting pin on the anode to restrict the source spot size. I expected the spot size to decrease and the dose observed at one meter to decrease. Each anode pin was fabricated from copper stock and machined to 1 mm in diameter and 2.5 mm in length with a full radiused tip while a button of the copper stock was left to enable an adequate electrical connection with the anode. The anode plate was fashioned with a recess which allows the button to pocket into the anode leaving the cathode facing surface of the button flush with the anode and the pin protruding out from the anode surface into the A-K gap. Additionally, this design had no high-Z material which equates to a Bremsstrahlung spectrum downshifted in energy and would result x-ray source spot lower in intensity after considering the attenuation of the vacuum plate. If a high-Z converter is needed in similar future experiments tantalum, gold, or lead foil applied to the tip of the anode pin could be attempted.

9.1 Anode field enhancement effects on the electron beam

The shape of the anode pin will allow a convergence of the majority of the electric field lines onto the tip of the pin. This should work to focus the electron beam from the beginning of the shot onto the tip of the anode pin earlier than in rod pinch diodes and with a more direct focusing mechanism that persists even when the shot begins. It is my opinion that the presence of plasma cannot be avoided as long as there is an electron beam incident upon a surface in the vacuum chamber with a sufficient energy. With the use of the anode pin, however, I believe the majority of the ion plume originates from the surface of the anode pin.

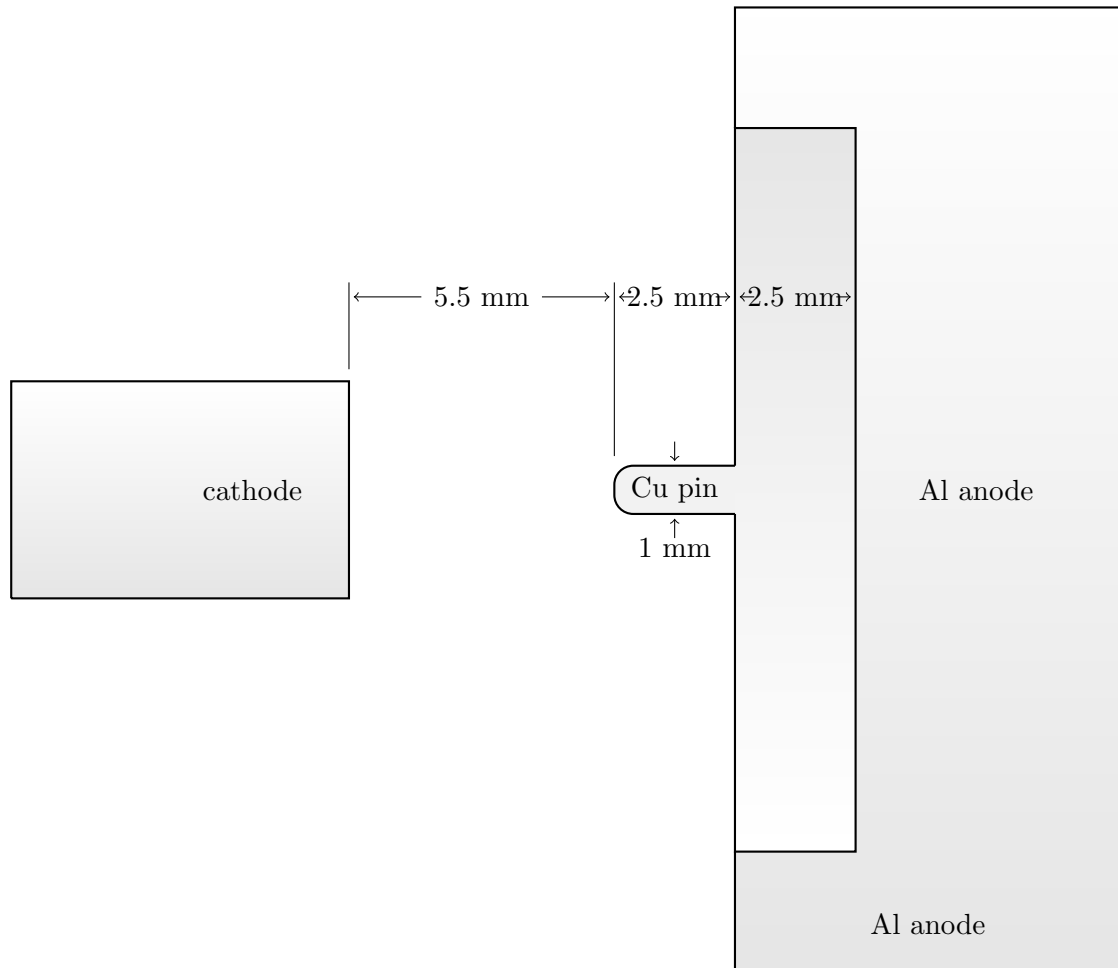


FIGURE 9.1: Sketch of the diode featuring an anode pin to induce field enhancements at the anode.

9.2 Anode field enhancement experiments

9.2.1 Effect on the spot size

For the measurement of the spot size a horizontal tungsten rolled edge was placed on axis with a phosphor screen positioned to capture the umbra cast onto the image plane from which the temporal extent of the source can be inferred.

9.2.2 Suggestions from the spot diameter

More shots are needed to produce statistics on reliability and to determine the effect of shot to shot variation but the data shows the smallest known radiographic spot size observed to date on the TriMeV system. The spot size ranges from 0.51 to 0.88 mm in diameter with a mean of 0.73 mm and a standard deviation of 0.1 mm when considering

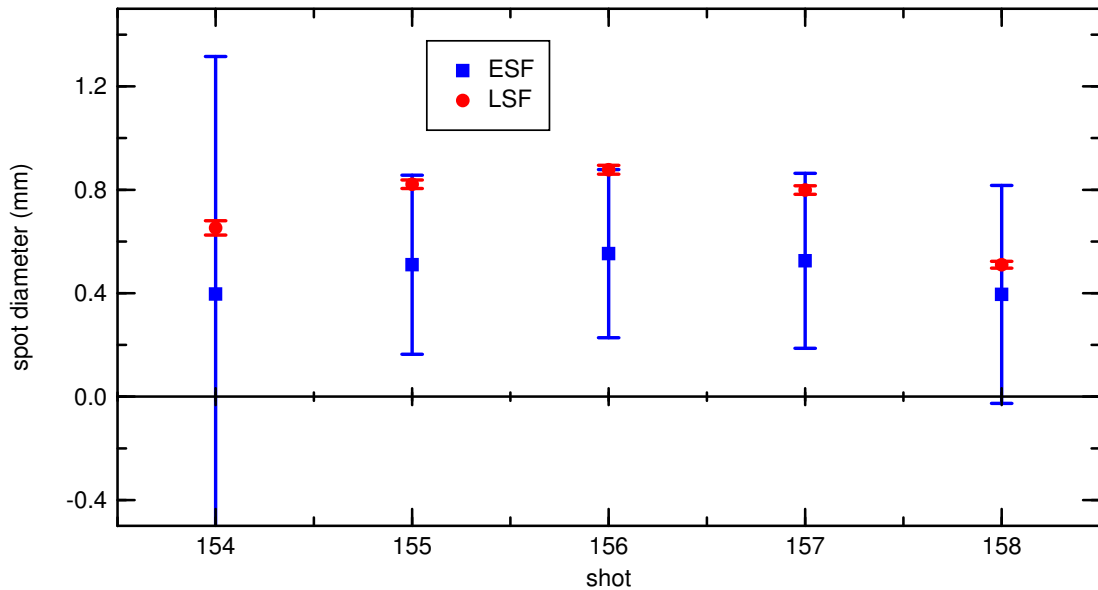


FIGURE 9.2: Spot size as a function of shot number for the anode field enhancement shots.

the FWHM LSF as the source diameter. Comparing this with a mean of 3.38 mm and a standard deviation of 0.52 mm in the shots with a cathode sleeve presented earlier, each of these deviations are approximately 15% of the mean, this suggests that the deviation in spot size shrinks proportionate to the decrease in mean spot size which will equate to a smaller deviation in figure of merit or quality potential.

9.2.3 Anode field enhancement dose effects

For the anode field enhancement experiments the dose was measured by silicon PIN diodes and OSLDs. In figure 9.3 I have plotted this data as a function of shot number.

To characterize the dose for this series of anode field enhancement experiments the mean and standard deviations of these five shots are 517 mrad at one meter and 186 mrad respectively when considering the OSLD data.

9.2.4 Effect on figure of merit

In (figure 9.4) I have calculated and plotted the FOM to quantify improvement to the quality potential, in terms of radiography, that has been made with the anode field enhancements. When considering the FOM calculated from the OSL dose at one meter and the FWHM of the LSF the anode field enhancements resulted in a mean FOM of 114 rad @ 1 m /mm² with a standard deviation of 86.7 rad @ 1 m /mm² compared to

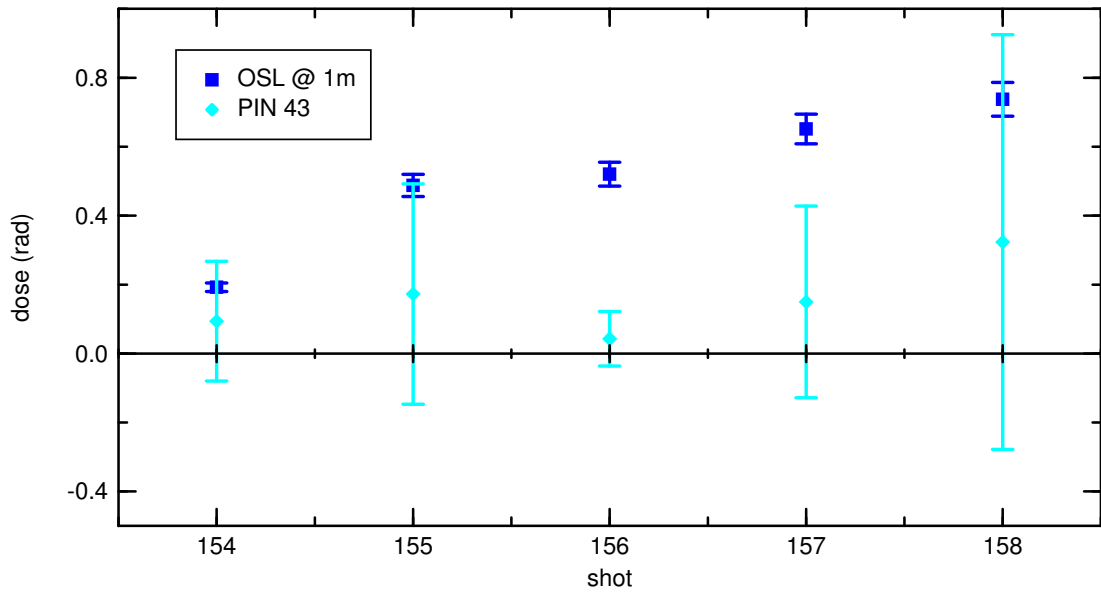


FIGURE 9.3: Dose with respect to shot number for the anode field enhancement experiments.

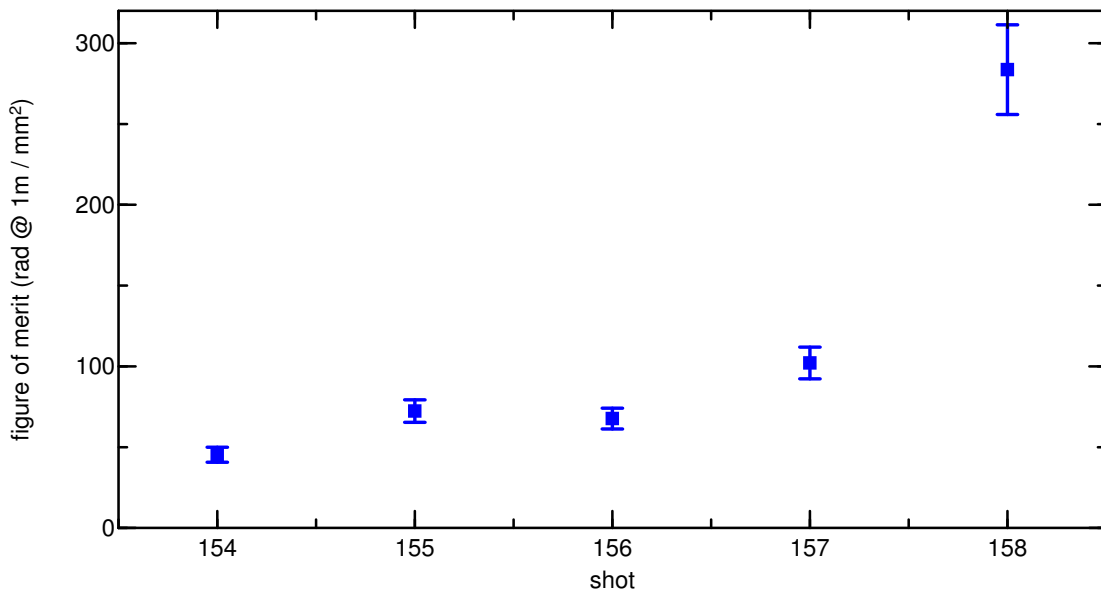


FIGURE 9.4: Figure of merit as calculated from OSL measured dose with anode field enhancements by shot number. The LSF FWHM description of the spot size was used.

a mean of $11.9 \text{ rad @ } 1 \text{ m / mm}^2$ with a standard deviation of $6.09 \text{ rad @ } 1 \text{ m / mm}^2$ for the cathode sleeve experiments.

It is interesting to note the continued increase in the FOM throughout the series of tests. The variable in this series of experiments is the width of the A-K gap which is displayed in table 9.1. This suggests that the ideal A-K gap for this system may not have been achieved. Additionally, the high current and collapsing voltage measured at the diode (see Figures 9.5 and 9.6) suggest this design exhibits an impedance below 60

TABLE 9.1: Shot and A-K gap width for anode field enhancement experiments.

Shot	A-K gap (mm)
154	5.5
155	6.5
156	6.5
157	7.5
158	8.5

ohms. Design changes to increase running impedance of this diode will be necessary to achieve the full voltage possible when using TriMeV.

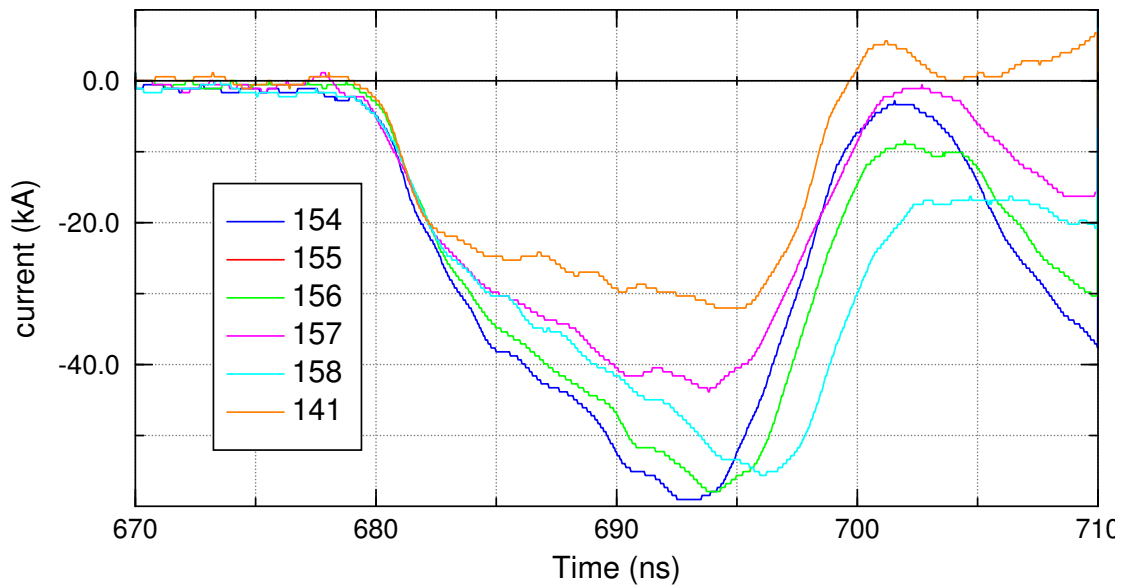


FIGURE 9.5: Diode current by shot as measured by a B-dot embedded in the vacuum chamber wall. Shot 141 included for comparison.

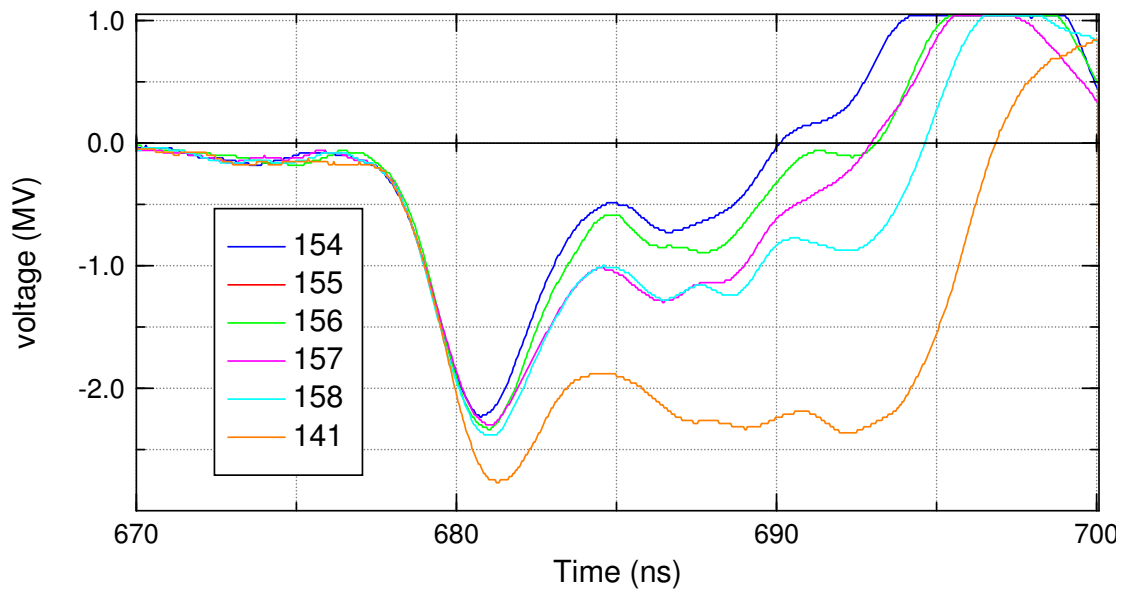


FIGURE 9.6: Diode voltage by shot as measured by a D-dot embedded in the vacuum chamber wall. Shot 141 included for comparison.

Chapter 10

Conclusion

10.1 Performance Summary

I have measured the dose and the spot size and calculated the figure of merit for three series of SMP diode experiments.

First, the cathode sleeve experiment shows that with the change in position (measured as the length of the reveal of the cathode tip in relation to the tip of the sleeve) the spot size decreases over the range of cathode reveal 0 to -9.5 mm from 3.81 ± 0.09 mm. Additionally the wide distribution of spot sizes without the sleeve ($\sigma = 0.565$ mm) and with a positive reveal ($\sigma = 0.651$ mm) were not observed in the reveal range of 0 to -9.5 mm ($\sigma = 0.265$ mm). This suggests the sleeve within the reveal range of 0 to -9.5 mm reduces the possibility of instabilities affecting spot focus and position at the converter.

The OSL dose measurements for the cathode sleeve experiments show as the sleeve reveal ranged from 0 to -6.3 mm the dose increased from 0.37 to 0.81 ± 0.05 rad at one meter on axis suggesting a collimating effect as the reveal decreases on this range. Also the OSL measured dose at one meter is reduced from 0.81 to 0.41 ± 0.05 rad as the reveal decreases from -6.3 to -19.05 cm which gives me the impression that there are competing effects.

Figure of merit for the cathode sleeve experiments when calculated from the FWHM of the LSF suggest the use of a cathode sleeve alone is insufficient to increase the radiograph quality potential of the system since the mean average FOM for shots with sleeve is 5.4 ± 0.2 rad @ $1\text{m}/\text{mm}^2$ compared to 15.8 ± 0.8 rad @ $1\text{m}/\text{mm}^2$ for shots without a cathode sleeve. It is notable that the standard deviation of the no sleeve shots is 14.1 rad @ $1\text{m}/\text{mm}^2$ compared to shots with sleeve at 6.09 rad @ $1\text{m}/\text{mm}^2$. Based upon FOM the "best" shots range from 22.6 ± 2.2 to 19.2 ± 1.9 rad @ $1\text{m}/\text{mm}^2$ all being shots without a cathode sleeve. The rest of the no-sleeve shots range from 12.0 ± 1.2 to 9.6 ± 1.0 rad @ $1\text{m}/\text{mm}^2$ and the shots with sleeve from 9.3 ± 0.9 to 2.6 ± 0.2 rad @ $1\text{m}/\text{mm}^2$.

Next, for the planar shroud experiments the spot size is reduced to approximately 1/3 the spot size over comparable shots without a shroud where the shroud bore and the ring cathode diameters are the same and when choosing to define the spot size as the FWHM of the LSF. The spot size is further reduced to 1/4 in shots with an anode shroud bore diameter 1/2 the ring cathode diameter.

Considering the OSL derived measurements the mean dose 20.6 ± 0.8 rad at 1 m for shots without an anode shroud and was reduced by more than half (6.8 ± 0.3 rad at 1 m) for shots featuring a shroud with a cathode sized bore but changed little (6.8 ± 0.5 rad at 1 m) when the shroud bore diameter was half the cathode diameter.

We note a modest improvement in the FOM in shots with a 25.4 mm bored shroud (5.42 ± 0.37 rad @ $1\text{m}/\text{mm}^2$) over those without a shroud (4.58 ± 0.26 rad @ $1\text{m}/\text{mm}^2$) but a significant improvement for 12.7 mm bored shroud (13.7 ± 1.32 rad @ $1\text{m}/\text{mm}^2$). This data suggests that the quality of the radiographic source can be improved by the use of a shroud with an appropriately sized bore.

Improvements in radiographic spot size and FOM were observed with the use of anode field enhancements. Here the limit of these improvements in relation to the A-K gap was not observed and the rising current and voltage collapse observed at the diode all suggest that the performance of the diode could be improved by using a wider A-K gap. When ranging the A-K gap from 5.5 mm to 8.5 mm the mean spot size was 0.73 mm \pm 0.1 mm and an average of 114 rad @ 1 m/ mm^2 \pm less than 86.7 rad @ 1 m/ mm^2 .

10.2 Future work

Given the brevity of the data set presented in this thesis, more experiments are needed to characterize the effects of shot to shot variation in order to build statistically significant data sets with respect to the sleeve and shroud experiments.

10.2.1 Sleeve and shroud combined diode

Given the shroud's ability to concentrate the electron beam on the converter and the observed reliability in spot size of the sleeve equipped cathode, a combination of the two may have the potential to yield a diode with a small and reliable spot size.

10.2.2 Cathode sleeve effects

The content of the ion plasmas surely has an effect on the plasma sheath's ability to shape the electron beam. Time and resources did not allow for experiments that would allow insights into the effect. Experiments comparing the effect of otherwise identical cathode sleeves made of polyethylene, graphite, ceramic, may provide information on the effect of electron beam shaping efficacy of the plasmas based on their ion content.

10.2.3 Anode field enhancements

One difficulty with the anode pin is to ensure an adequate electrical connection between it and the grounded anode. The design must ensure a good electrical connection to allow a small spot size consistently among shots. One solution is to fabricate from 1/2 inch diameter copper stock a pin protruding from a 1/2 inch diameter copper button that is then epoxied (with conductive silver microbead epoxy) into a pocket hole in the anode plate. The large surface area along with the conductive epoxy of the button against the anode plate allows an adequate electrical connection. This design is problematic in that the copper is not very high Z for efficient Bremsstrahlung conversion and that the thickness of copper and aluminum needed for mechanical reasons attenuates the x-ray signal.

Attempts with a brass electrical discharge machining (EDM) tube anode pin have been made but ensuring an adequate electrical connection has been elusive. The motivation stems from the hope that the plasma along the walls of the pin along with the Bennett force would constrict the electron beam to a smaller spot on a small converter behind the EDM tip. Soldering was tried but without success since soldering to a large aluminum plate is difficult. Conductive epoxy, while providing a good mechanical grip, could not seem to provide a favorable electrical connection given the small surface area available. Soldering to conductive copper tape was tried with a good mechanical grip but did not provide a good enough electrical connection.

Recommendations for future mounting efforts include using a buried collet at the anode similar to the cathode-buried collet used in past TriMeV experiments not performed at the Idaho Accelerator Center. The collet allows the EDM pin to be held tightly and is expected to give an adequate electrical connection because of the way the aluminum teeth of the collet are expected to bite into the EDM pin. This set up also allows a converter behind the collet and a configuration where the only attenuation of the signal is by a nominal thickness of the converter and the anode plate holding back vacuum.

10.2.4 Silicon diode arrays

The signal from a silicon PIN diode can give dose information as a function of time over the lifetime of the shot. A silicon PIN diode array across the umbral edge cast by the rolled edge could be used to gain information about how the spot size varies as a function of time over the shot.

10.2.5 Perpendicular rolled edges

One of the difficulties in calculating the FOM stems from the variability in the definition of the spot size. One reasonable solution could be to refrain from measuring the spot size and instead reconstruct the distribution of the source. In my experiments I have measured the spot size using the rolled edge which can give information about the spot distribution in one dimension. But to reconstruct a two dimensional spot distribution a second rolled edge, perpendicular to the first, is required [28].

10.2.6 Flat field radiographs

The radiographic field observed in the radiographic images does not have a flat field. This is noted in the manifestation of a non-uniform density in the portions of the image plane that are, by definition of the experimental setup, areas of full attenuation or full exposure. It is recommended in future experiments to correct the raw images to account for spacial non-linearity in sensitivity and radiation bleed through. Alternatively a graduated collimator could be fashioned to flatten the field but this option could require separate collimators for each radiographic setup.

10.2.6.1 Flat fielding method

Flat fielding is simply adjusting the raw image to account for the non-linear spacial sensitivity and the radiation bleed through and dark count that give rise to the background [29]. The correction requires the measurement of a dark field where the image is collected with the source blocked, the flat field where the converter is uniformly illuminated, and the raw image from the radiographic setup. The corrected image is obtained by calculating the ratio of the raw image and the flat field each corrected for dark field effects.

$$I_{corrected} = \frac{I_{raw} - f_{dark}}{f_{flat} - f_{dark}} \quad (10.1)$$

10.2.6.2 Radiographic source collimator

The addition of a radiographic collimator is expected to reduce the background field observed in the radiograph. From the gas filled diode design the expected collimator will be a total of 11 cm thick Pb. Additionally the shape of an optimized collimator is

potentially different between varying diode setups making the solution inconvenient and expensive when experimenting with different diodes.

10.2.6.3 Shielding

Efforts were made to reduce the x-ray background observed early on in this work by using a 2-inch-thick Pb covering the outside of the grounded vacuum chamber plate, but did not appear to flatten the radiographic background.

10.2.7 Rogowski coils

Rogowski coils are inexpensive and easy to produce. They have the benefit of measuring in aggregate the curling magnetic field at all points azimuthally about a current flux. The B-dots used in the research for this thesis measure the magnetic field in only one localized position, so a Rogowski coil may have advantages particularly when anomalies arise in the magnetic field. Also, the Rogowski coil could give another data point on current measurements. A Rogowski coil could be incorporated into the interior surface of the anode plate on the vacuum chamber to give an additional current measurement for the diode in use. Here care would have to be taken to shield the coil from the electrons emitted from the diode. A Rogowski coil could be used on the exterior of the anode plate to monitor electron flux which could be particularly helpful as a diagnostic for electron flux thru the anode plate for instance when near x-ray dose measurements are desired and a thin anode plate is in use or when extracting the electron beam from TriMeV thru a vacuum window.

10.2.8 Transmission line gas switching

The current use of self closing switches in the TriMeV system introduces variability in the timing between the activation of the fire button and the arrival of the voltage pulse at the diode. The time for the voltage at the diode to reach -1 kV (when the scope was triggered from the fire button signal) was on average 650.3 ns with a standard deviation of 80.0 ns when sampling shots 50-194. This variation in timing limits the systems ability to be timed to another event such as lasers or back light set up in the vacuum chamber. This variability could be reduced by improving the timing reliability of the switches in the system by installing pressurized gas switches or laser induced switches.

10.2.9 Plasma diagnostics

An interferometry setup to monitor the A-K gap could quantify the density of the plasma found there. Additionally a Schlieren imaging system could provide qualitative gradient information on the plasma density.

10.2.10 Spectrum determination

It would be useful in characterizing TriMeV as a radiographic device to know the energy spectrum of the source or the electron beam. This information could illuminate limitations and possible applications of the system.

10.2.10.1 Dose depth profile

In the dose depth profile measurement the electron beam is incident on a split block of aluminum with radiochromic film sandwiched between the two halves of the block. The electrons penetrate the block then scatter and provide dose to the film at the penetration level so the dose observed on the sandwiched film contains information on the penetration of the electron beam. The penetration is dependant on the energy of the electrons so the profile contains electron beam spectrum information. Knowing the electron beam spectrum and the converter and the anode plate material and thickness one could estimate, by calculation, the spectrum of the radiographic source.

10.2.10.2 Laser Compton scattering

In laser Compton scattering monochromatic laser light is scattered from accelerated electrons. The scattered photons at each angle from the interaction site will have wavelengths shifted from the incident ray dependent upon the energy spectrum of the electron beam. In this way it is possible to determine the spectrum of the electron beam.

10.2.10.3 Geant4 simulations

Modeling of the electron beam and the photons from the beam on the converter could provide spectrum predictions for both the electron beam and the x-ray spectrum. The models, once programmed, could give insights into valuable variations in electron diode design variations.

10.2.10.4 Diode voltage and current estimations

Calculations involving the current and the voltage at the diode could be used to estimate the spectrum of the electron beam since the acceleration of the electrons is commensurate with the voltage and the number of electrons related to the current across the A-K gap.

10.2.10.5 Aluminum test wedge

The attenuation of the dose as a function of thickness through aluminum is dependent upon the spectrum of the incident photons. The use of an aluminum test wedge set up between the phosphor screen and the source can provide spectrum dependant attenuation profiles as a function of thickness and will give a way to gauge the plausibility of postulated x-ray spectra [9] and may provide a way to suggest possible spectra from each shot.

10.2.11 Summary

These future work recommendations are limited to improvements that would enable further investigation into the effects of ion plumes on the electron beam in the diode which is at the heart of controlling the radiographic spot size. Further, these improvements would add spectrum information and yield a more complete characterization of TriMeV as a radiographic source. It is my opinion that these recommendations, together with larger data sample sizes, will expeditiously advance the inferences noted in the data to reliable and comprehensive descriptions of this radiographic source.

Bibliography

- [1] G. Cunningham and C. Morris, “The development of flash radiography,” report LA-UR-03-5305 28, Los Alamos National Lab, Los Alamos, NM, 2003.
- [2] S. B. Swanekamp, G. Cooperstein, J. W. Schumer, D. Mosher, F. C. Young, P. F. Ottinger, and R. J. Commisso, “Evaluation of self-magnetically pinched diodes up to 10 mv as high-resolution flash x-ray sources,” *IEEE Transactions on Plasma Science*, vol. 32, pp. 2004–2016, Oct 2004.
- [3] R. B. Spielman and Y. Gryazin, “Screamer: A optimized pulsed-power circuit-analysis tool,” in *2016 IEEE International Power Modulator and High Voltage Conference (IPMHVC)*, pp. 269–274, July 2016.
- [4] C. L. Morris, E. Ables, K. R. Alrick, M. B. Aufderheide, P. D. B. Jr., K. L. Buescher, D. J. Cagliostro, D. A. Clark, D. J. Clark, C. J. Espinoza, E. N. Ferm, R. A. Gallegos, S. D. Gardner, J. J. Gomez, G. A. Greene, A. Hanson, E. P. Hartouni, G. E. Hogan, N. S. P. King, K. Kwiatkowski, R. P. Liljestrand, F. G. Mariam, F. E. Merrill, D. V. Morgan, K. B. Morley, C. T. Mottershead, M. M. Murray, P. D. Pazuchanics, J. E. Pearson, J. S. Sarracino, A. Saunders, J. Scaduto, A. E. S. von Wittenau, R. A. Soltz, S. Sterbenz, R. T. Thompson, K. Vixie, M. D. Wilke, D. M. Wright, and J. D. Zumbro, “Flash radiography with 24 gev/c protons,” *Journal of Applied Physics*, vol. 109, no. 10, p. 104905, 2011.
- [5] C. Ekdahl, “Modern electron accelerators for radiography,” *IEEE Transactions on Plasma Science*, vol. 30, no. 1, pp. 254–261, 2002.
- [6] P. R. Menge, J. Gustwiller, D. L. Johnson, J. E. Maenchen, I. Molina, D. C. Rovang, R. Shear, S. Cordova, D. Droemer, E. Hunt, E. Ormand, L. Woo, R. J. Commisso, G. Cooperstein, S. B. Swanekamp, B. V. Oliver, D. V. Rose, and D. R. Welch, “Experimental development of radiographic sources on trimev,” in *ICOPS 2000. IEEE Conference Record - Abstracts. 27th IEEE International Conference on Plasma Science (Cat. No.00CH37087)*, pp. 232–, June 2000.
- [7] P. R. Menge, D. L. Johnson, J. E. Maenchen, C. L. Olson, D. C. Rovang, D. Droemer, E. Hunt, B. V. Oliver, D. V. Rose, and D. R. Welch, “Experimental comparison of 2-3mv x-ray sources for flash radiography,” report sand2002-0082, Sandia National Laboratories, Albuquerque, NM 87185, Livermore, CA 94550, 2002.
- [8] E. Hunt, G. MacLeod, L. Wood, D. Droemer, B. Oliver, D. Welch, C. Eichenberger, P. Spence, I. Smith, and V. Bailey, “The trimev accelerator for pulsed power driven radiography experiments,” 01 1999.

-
- [9] B. V. Weber, R. J. Allen, R. J. Commisso, G. Cooperstein, D. D. Hinshelwood, D. Mosher, D. P. Murphy, P. F. Ottinger, D. G. Phipps, J. W. Schumer, S. J. Stephanakis, S. B. Swanekamp, S. C. Pope, J. R. Threadgold, L. A. Biddle, S. G. Clough, A. Jones, M. A. Sinclair, D. Swatton, T. Carden, and B. V. Oliver, "Radiographic properties of plasma-filled rod-pinch diodes," *IEEE Transactions on Plasma Science*, vol. 36, pp. 443–456, April 2008.
- [10] K. Hahn, N. Bruner, S. R. Cordova, I. Crotch, M. D. Johnston, J. J. Leckbee, I. Molina, B. V. Oliver, S. Portillo, J. Threadgold, T. J. Webb, D. R. Welch, and D. Ziska, "Status of self-magnetic pinch diode investigations on rits-6," in *2009 IEEE Pulsed Power Conference*, pp. 34–39, June 2009.
- [11] R. J. Commisso, G. Cooperstein, D. D. Hinshelwood, D. Mosher, P. F. Ottinger, S. J. Stephanakis, S. B. Swanekamp, B. V. Weber, and F. C. Young, "Experimental evaluation of a megavolt rod-pinch diode as a radiography source," *IEEE Transactions on Plasma Science*, vol. 30, pp. 338–351, Feb 2002.
- [12] B. V. Weber, R. J. Allen, R. J. Commisso, G. Cooperstein, D. D. Hinshelwood, D. Mosher, D. P. Murphy, P. F. Ottinger, D. G. Phipps, J. W. Schumer, S. J. Stephanakis, S. B. Swanekamp, S. Pope, J. Threadgold, L. Biddle, S. Clough, A. Jones, M. Sinclair, D. Swatton, T. Carden, and B. V. Oliver, "Plasma-filled rod-pinch diode research on gamble ii," in *2007 IEEE 34th International Conference on Plasma Science (ICOPS)*, pp. 440–440, June 2007.
- [13] B. V. Oliver, K. Hahn, M. Johnston, and S. Portillo, "Advances in high intensity e-beam diode development for flash x-ray radiography," report sand2008-5761c, Sandia National Laboratories, Albuquerque, NM 87185, Livermore, CA 94550, 2008.
- [14] N. Bruner, D. R. Welch, M. D. Johnston, and B. V. Oliver, "3d simulations of the self-magnetic-pinch diode," in *2011 IEEE Pulsed Power Conference*, pp. 1057–1062, June 2011.
- [15] G. Cooperstein, J. R. Boller, R. J. Commisso, D. D. Hinshelwood, D. Mosher, P. F. Ottinger, J. W. Schumer, S. J. Stephanakis, S. B. Swanekamp, B. V. Weber, and F. C. Young, "Theoretical modeling and experimental characterization of a rod-pinch diode," *Physics of Plasmas*, vol. 8, no. 10, pp. 4618–4636, 2001.
- [16] N. Bennett, M. D. Crain, D. W. Droemer, R. E. Gignac, G. Lare, I. Molina, R. Obregon, C. C. Smith, F. L. Wilkins, D. R. Welch, S. Cordova, M. L. Gallegos, M. D. Johnston, M. L. Kiefer, J. J. Leckbee, M. G. Mazarakis, D. Nielsen, T. J. Renk, T. Romero, T. J. Webb, and D. Ziska, "Shot reproducibility of the self-magnetic-pinch diode at 4.5 mv," *Phys. Rev. ST Accel. Beams*, vol. 17, p. 050401, May 2014.

-
- [17] J. D. Jackson, *Classical Electrodynamics*. New York, NY: John Wiley and Sons, Inc., 1999.
- [18] M. Vogel, “Electricity and magnetism, 2nd ed., by Edward Purcell,” *Contemporary Physics*, vol. 53, no. 3, pp. 287–288, 2012.
- [19] J. C. Martin, “Aids to estimating the quality of flash radiographs,” report ss-wa/jcm/788/266, Atomic Weapons Research Establishment, Aldermaston, England, 1978.
- [20] R. Spielman, “Technical notebook,” January 2018. Private Communication.
- [21] C. G. P. Persephonis, K. Vlachos and J. Parthenios, “The inductance of the discharge in a spark gap,” *Journal of Applied Physics*, vol. 71, pp. 4755–4762, June 1992.
- [22] M. Barlund, “Usability study of shift logbooks in physics experiments at CERN,” Master’s thesis, HELSINKI UNIVERSITY OF TECHNOLOGY, Otaniemi, Finland, November 2008.
- [23] B. Hu, *Optically stimulated luminescence (OSL) and its applications in radiation therapy dosimetry*. PhD thesis, School of Engineering Physics, University of Wollongong, New South Wales, Australia, October 2010.
- [24] T. Sanford, J. A. Halbleib, C. E. Heath, R. Mock, and J. W. Poukey, “Dose-voltage dependence for Helix/Hermes III bremsstrahlung diodes,” 01 1987.
- [25] M. J. B.V. Oliver, K. Hahn and S. Portillo, “Advances in high intensity e-beam diode development for flash x-ray radiography,” *ACTA PHYSICA POLONICA A*, vol. 115, pp. 1044–1046, June 2009.
- [26] A. E. Blaugrund, G. Cooperstein, and S. A. Goldstein, “Relativistic electron beam pinch formation processes in low impedance diodes,” *The Physics of Fluids*, vol. 20, no. 7, pp. 1185–1194, 1977.
- [27] J. S. Luce, H. L. Sahlin, and T. R. Crites, “Collective acceleration of intense ion beams in vacuum,” *IEEE Transactions on Nuclear Science*, vol. 20, pp. 336–341, June 1973.
- [28] G. Barnea, “Penumbra imaging made easy,” *Review of Scientific Instruments*, vol. 65, no. 6, pp. 1949–1953, 1994.
- [29] C. Ekdahl, “Characterizing flash-radiography source spots,” *J. Opt. Soc. Am. A*, vol. 28, pp. 2501–2509, Dec 2011.
- [30] R. Spielman, “Isu screamer web page.”

-
- [31] C. J. Yahnke, “Calibrating the microstar.”
- [32] D. Hinshelwood, *Stella*. U.S. Naval Research Laboratory, 2016. Stella software user manual.
- [33] Fuji Photo Film Co., Ltd., *Bio-imaging Analyzer BAS 1800II Operation Manual*, first edition ed., 1995.
- [34] H. N. Udupa, P. Mah, S. B. Dove, and W. D. McDavid, “Evaluation of image quality parameters of representative intraoral digital radiographic systems,” *Oral surgery, oral medicine, oral pathology and oral radiology*, vol. 116 6, pp. 774–83, 2013.

Appendix A

Screamer

A.1 Introduction

Screamer is a circuitry modeling code for single module accelerators.

It simulates the time evolution of an electrical system based on system component characteristics and initial parameters.

Series elements and their configurations are defined by the user to model the system of interest.

The basic element of Screamer is the single node block (two nodes shown in figure A.1 for illustration of the common series configuration).

Screamer software then calculates the voltage at each node during each time step.

Due to the conservation of charge we can relate the currents in and out of the node.

$$\begin{aligned}
 I_{i-1} &= I_i + I_{bi} + I_{Cs} + I_{Rs} \\
 I_{i-1} &= I_i + I_{bi} + \frac{V_i}{R_i} + \frac{\partial}{\partial t}(C_i V_i)
 \end{aligned}
 \tag{A.1}$$

Where we have I_{i-1} as the current flowing into node i , I_i as the current flowing out of node i and through the resistor and inductor R_i and L_i , I_{bi} as the current flowing out

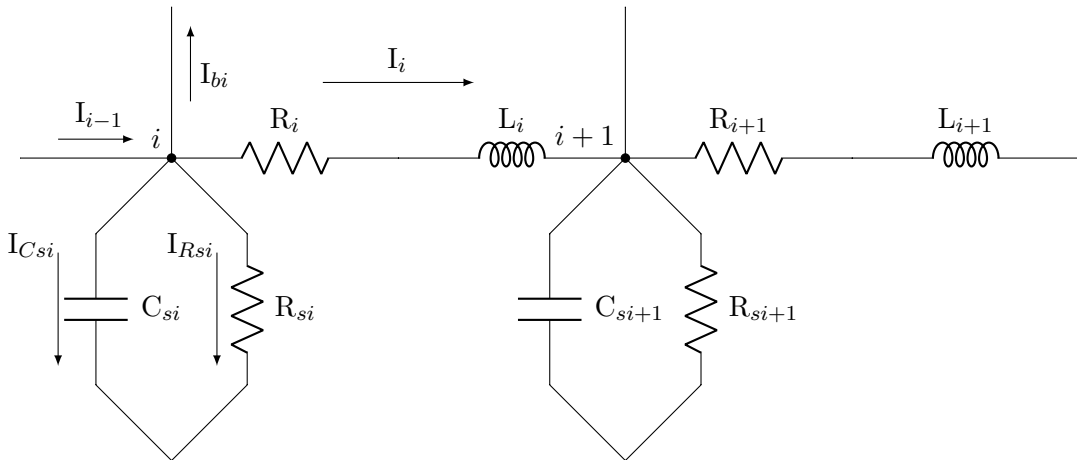


FIGURE A.1: Two screamer elements connected in series [3].

of node i into the top branch, I_{Cs} as the effective current flowing out node i and across the shunt capacitor, and I_{Rs} as the current flowing out of node i and across the shunt resistor.

A similar statement of voltage can be constructed.

$$\begin{aligned} V_i - V_{i+1} &= V_{Ri} + V_{Li} \\ V_i - V_{i+1} &= R_i I_i + \frac{\partial}{\partial t} (L_i I_i) \end{aligned} \quad (\text{A.2})$$

With V_i as the voltage at node i , V_{i+1} as the voltage at node $i + 1$, V_{Ri} as the voltage drop across the resistor R_i , and V_{Li} as the voltage drop across the inductor L_i .

If we allow the system to evolve through time in discrete time steps half way through the times step we know the following

$$\begin{aligned} V_i &= 0.5(V_i^n + V_i^o) \\ I_i &= 0.5(I_i^n + I_i^o) \\ I_{bi} &= 0.5(I_{bi}^n + I_{bi}^o) \\ \frac{\partial}{\partial t} (C_i V_i) &= C \left(\frac{V_i^n - V_i^o}{\nabla t} \right) \\ \frac{\partial}{\partial t} (L_i I_i) &= L \left(\frac{I_i^n - I_i^o}{\nabla t} \right) \end{aligned} \quad (\text{A.3})$$

A.2 Motivation

Our motivation in using screamer to model the circuitry is twofold: to provide a platform wherein the effect of alterations to the system can be investigated and to gain a better understanding of the components of the system and their effects.

A.3 Installation notes

When memory available is less than the memory needed to run the Screamer program the execution file will result in a segmentation fault error even before the user's run deck has been accessed. The reason being Fortran allocates memory needed for the program prior to running the program and if the Fortran program tries to allocate a memory

block larger than the available block the user will be notified by way of a segmentation fault. The allocated memory (and consequently the number of nodes the user is allowed in the run deck) can be reduced to avoid the segmentation fault. This is achieved by editing the maximum number of nodes specified in the `zdemmax.h` file and recompiling the binary.

A.3.1 Windows

A.3.2 Linux

The Linux instance for this installation was set up on a Sandisk 3.0 16GB flash drive from which a Dell Inspiron N5050 PC (Intel i3-2370M CPU 2.4GHz, 6GB RAM, 64-bit) was booted which allowed the existing Windows installation to remain untouched and somewhat independent. This protocol was followed to set up the Linux instance.

1. An installation CD was prepared containing Ubuntu 16.04.4 LTS (see <https://tutorials.ubuntu.com/tutorial/tutorial-burn-a-dvd-on-windows> for more information) and the system with formatted flash drive inserted was booted from the CD.
2. Choose the try Ubuntu option.
3. Launch the Ubuntu installation by clicking the desktop icon. Before the installation you should ensure stable internet and power connections and adequate drive space.
4. Activate "download updates while installing" and "install third-party software" and click continue.
5. Choose the "something else" option and click continue and I chose to unmount the devices so to allow partitioning.
6. Set the device for the boot loader installation to the flash drive to be configured.
7. Locate the device in the device list window that corresponds to the flash drive (this should be displayed as "free space" in the list—if not you will need to unmount the device to allow partitioning), click to highlight and add a new partition by clicking the plus button.
8. Designate the partition as primary, set the location to the beginning of this space, use as swap area, set the size to 6GB, and click OK.

9. Again highlight free space and set up another partition with size set to the remaining space on the drive, a primary type partition at the beginning of this space, use as EXT4 journaling file system and specify the mount point as the root location. Ensure that there are no other swap spaces in the system. The Ubuntu installation on the flash drive will seek to use other swap partitions in the system so if there are other swap spaces in the system set them to "do not use this partition".
10. Click "Install Now" and ensure the summary includes all the features you require and click continue.
11. Set the name of the user and computer and specify a password for the user. Allow the system to install Ubuntu.
12. Restart the system and boot from the USB drive.

After the system is booted into Ubuntu the following commands (adapted from installation notes [30]) from the terminal window will enable Screamer simulations.

1. Launch the terminal window (ctrl-alt-t).
2. Ensure the latest versions of gcc, gfortran and build-essential are installed. The version of these programs can be displayed by entering "`<program name> -v`". If they need to be installed execute the "`sudo apt-get install <program name>`" in the terminal window.
3. Download the zip file for the Screamer version desired by executing "`wget http://iac.isu.edu/zips/release_<version>.tar.gz`" where `<version>` is the screamer version number.
4. Unzip the download with "`tar -xvzf release_<version>.tar.gz`". At this stage of the process running the binary file is likely to result in a "cannot execute binary file" error because we have not yet compiled the binary on this system.
5. Compile the binary files using "`./screamer64.bat`" from the `~/<version>/src` folder which will run the commands specified in the batch file. Prior to compilation the paths in the batch file will likely need to be adjusted for the specific system on which it is being compiled. If the paths are unknown use the file browser in Ubuntu to locate the `libgcc.a`, `libgfortran.a`, and `libgquadmath.a` files. One can check the file was actually compiled by checking the time stamp on the binary file (`screamer64`) by executing the "`ls -l`" command.
6. The new binary file can be run with "`./screamer64`" or "`./screamer64 <run deck>`" in the terminal command line where `<run deck>` is the input file for the simulation.

During the simulation screamer will print to the screen the status of the simulation and end with a statement of the run time and write a *.log file which contains the details of the simulation and a data output file (if specified in the run deck).

A.4 Code

A.4.1 Run Deck For Simplified TriMeV Screamer Simulation

```

TriMeV-150908
!
Time-step 0.001e-9
Resolution-time 0.01e-9
End-time 1.5e-6
Number-prints 5
Execute-cycles all
Grids no
Echo-setup no
Max-points 40001
!
!This is a simplified partial model for TriMeV including:
! 1 Marx generator scaled as single capacitor
! 30 stages, 7 caps per bank, 2 banks per stage
! caps: 44 kV charge, 32 nF each, 1 m Ohm(est), 28 nH(est)
! switches: 2.5 Ohms(est), 1.2 uH, 4 mm midplane to electrode, 29 PSIG SF6
! 2 pulse line with d-dot 6 inches from end of pulse line
! 25.5 Ohm, 8.8 ns Marx to OS, 1.5 ns Marx to stub end
! 3 capacitance, inductance, and impedance of the open output switch included
! 13 pF(est), 88 nH(est), 1e12 Ohms(est)
! switch time:163 ns, gap: 4.7 cm, pressure(depth): 1.04 atm
! 4 transmission line with d-dot 6 inches from end of transmission line
! 40 Ohm, 9.0 ns OS to SS
!
BRANCH
!
!===== Marx =====
!
!Enter the pisection block and set the initial voltage on C1.
!      R1      C1      R2      L2      R3      C3
PISECTION 20e+3 3.73e-9 1.0e6 3.6e-6 20e+3 0.24e-9
INITIAL VC1 -2.64e6 !44e6 V/cap bank * 60 cap banks = -2.64e+6
VARIABLE R2 DECAY-MODEL
!Ropen Rclose tswitch t
1e6 15 0.0e-9 0.5e-9 !144ns data average -8.8ns length Marx to switch
!VARIABLE R2 SWITCH_MODEL
!dielectric switchtime gaplength pressure nswitches nchannels
!SF6      0.0e-9      0.004      1.97      60      1
!
!      R1      L1
RLSERIES 7.5 245e-9
!
!===== Pulse Line (Marx->Crowbar) =====

```

```

!
!Crowbar end of pulse line divides from the main line of power flow here.
!
ENDBRANCH
!
!===== Pulse Line (Marx->Output Switch) =====
!
!pulse line Marx to D-dot
!   Zvar  t      Zin Zout tres
TRLINE LINEAR 6.8e-9 25 25 0.1e-9
!
!D-dot monitor
csv VOUT
$VOS(V)
!
!pulse line monitor to switch
!   Zvar  t      Zin Zout tres
TRLINE LINEAR 3.0e-9 25 25 0.01e-9
!
!===== Output Switch =====
!
RLSERIES 1e6 80e-9
VARIABLE R2 DECAY-MODEL
!Ropen Rclose tswitch t
1e6 0 143e-9 0.75e-9 !144ns data average -8.8ns length Marx to switch
!
!VARIABLE R2 SWITCH_MODEL
!dielectric switchtime gaplength pressure nswitches nchannels
!OIL 138e-9 0.047 1.0 1 1
!
!make a top branch to put in the capacitance between the two lines at the switch
TOPBRANCH
!
!===== Pulse Line (Output->Sharpening Switch) =====
!
!pulse line output switch to D-dot
!   Zvar  t      Zin Zout tres
TRLINE LINEAR 6.0e-9 40.0 40.0 0.1e-9
!
!D-dot monitor
csv VOUT
$VSS(V)
!
!pulse line D-dot to sharpening switch
!   Zvar  t      Zin Zout tres
TRLINE LINEAR 3.0e-9 40.0 40.0 0.1e-9
!
!===== Sharpening Switch =====
!
RLSERIES 1.0e6 18e-9
!
VARIABLE R2 DECAY-MODEL
!Ropen Rclose tswitch t
1e12 0 154e-9 0.5e-9
!

```

```

!VARIABLE R2 SWITCH_MODEL
!dielectric switchtime gaplength pressure nswitches nchannels
!OIL      154e-9  0.103  1.0  1  5
!
TOPBRANCH
!
RCGROUND 1e+12 23e-12
!
!===== Pulse Line (Sharpening Switch->H2O Wedge) =====
!
!      Zvar  t      Zin Zout tres
TRLINE LINEAR 1.1e-9 40 40 0.1e-9
!
!===== H2O Wedge =====
!
RCGROUND 7e+3 23e-12
!
!===== Pulse Line (H2O Wedge->Vacuum) =====
!
!      Zvar  t      Zin Zout tres
TRLINE LINEAR 0.3e-9 40 40 0.01e-9
!
!===== Pulse Line (H2O Wedge->Diode) =====
!
!      Zvar  t      Zin Zout tres
TRLINE LINEAR 1.0e-9 60 60 0.1e-9
!
! vacuum section voltage diagnostic
csv VOUT
$VVac(V)
!
! vacuum section current diagnostic
csv IOUT
$IVac(A)
!
!      Zvar  t      Zin Zout tres
TRLINE LINEAR 6.65e-9 60 60 0.1e-9
!
! voltage output
csv VOUT
$VDiode(V)
!
! current output
csv IOUT
$IDiode(A)
!
!      Zvar  t      Zin Zout tres
TRLINE LINEAR 1.0e-9 60 60 0.1e-9
!
!===== Diode =====
!
RCG 1e12 0
!
!Variable R1 EDiode_model
!3 0.062 149e-9 1.0e8 0 4.4e-4 0.025 2.9e8 0.001 2.0e-3

```

```
!  
Variable R1 Diode_model  
162.85e-9 1.0e8 0 4.4e-4 0.025 2.9e8 0.001 2.0e-3  
!t Rmax Rmin Area G v Gmin Pmratio  
!  
! End of main branch  
!  
!=====  
Pulse Line (Marx->Crowbar)  
=====  
!  
! Crowbar end of pulse line  
!  
BRANCH  
!  
! Zvar t Zin Zout tres  
TRLINE LINEAR 1.5e-9 25 25 0.1e-9  
!  
! End of this branch  
!  
!=====  
Output Switch  
=====  
!  
!Capacitance over the gap of the output switch  
!  
BRANCH  
!  
RCGOUND 1e6 5.0e-12  
!  
!End of this branch  
!  
!=====  
Sharpening Switch  
=====  
!  
! Capacitance over the gap of the sharpening switch  
!  
Branch  
!  
RCGOUND 1e6 1.25e-12  
!  
! End of this branch  
!  


---


```

Appendix B

OSL calibration

B.1 Introduction

Landauer's OSLD features a plastic disk containing embedded $\text{Al}_2\text{O}_3:\text{C}$ (see figure B.1).

The deposition of energy into the crystal promotes valence electrons to the conduction band where the electrons are free to move about the volume of the crystal. These now conduction electrons are often captured by defects in the crystal which exhibit a lower potential energy. These states have a long lifetime so they are considered metastable yet possess a higher energy than the valence band from which the promoted electrons originated. The ionizing radiation is understood in a simplified way by one of the following mechanisms: photoelectric effect, Compton scattering, or pair production with

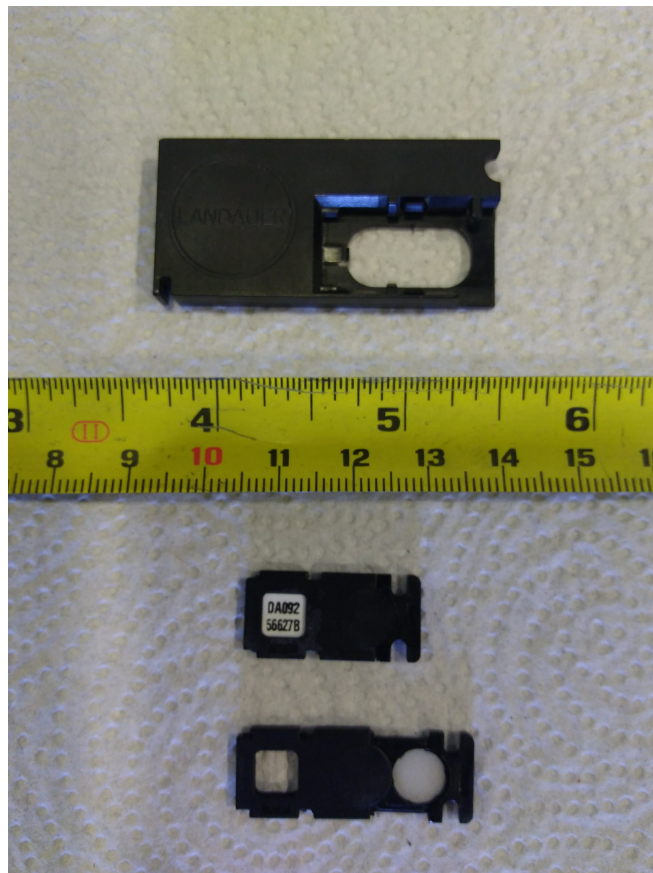


FIGURE B.1: Landauer's dot adapter cassette and dot dosimeter (with $\text{Al}_2\text{O}_3:\text{C}$ embedded disk concealed and exposed).

the probabilities of each dependent upon the energy of the photon introduced during x-ray exposure.

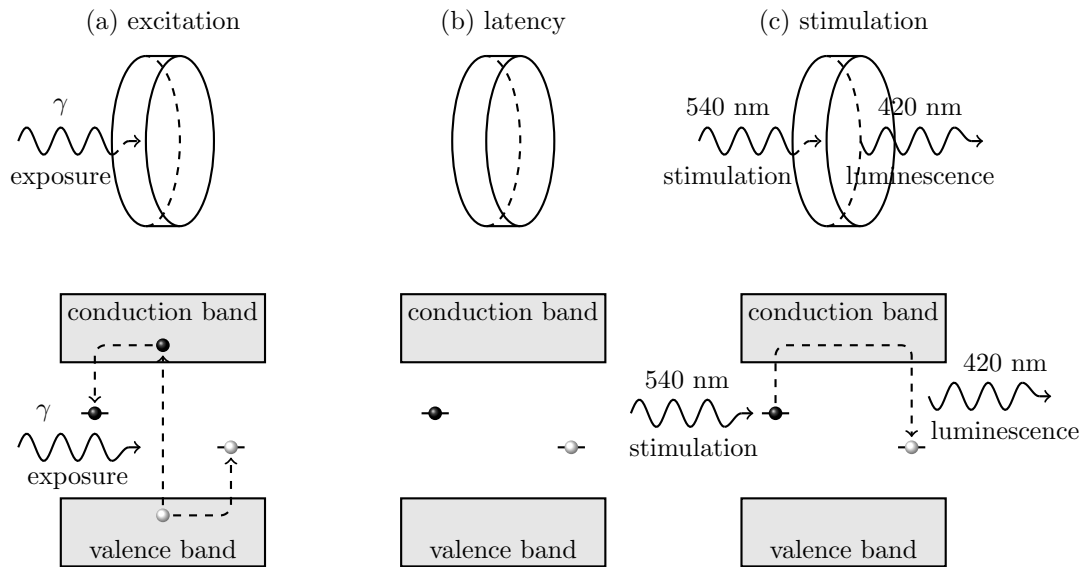


FIGURE B.2: The OSL mechanisms that enable the measurement of exposure. Exposure involves the separation and promotion of the electron to the conduction band where it moves freely throughout the crystal until being captured by a crystal defect leaving the electron in a higher energy state (a). The long lifetime of the captured electrons allows a "memory" of the exposure (b). Optical stimulation of the electron promotes the electron back to the conduction band where there exists a probability that the electron will recombine with the hole left during exposure (c).

The $\text{Al}_2\text{O}_3:\text{C}$ crystal responds to x-ray exposure in three ways by radio luminescence (RL), OSL, and thermo luminescence (TL). The difference in these types of luminescence is simply the conditions under which the luminescence takes place.

With RL the luminescence is observed during the exposure. Here the possibility exists to take the dose measurement in a different way. It is possible that time information about the dose could be obtained by using the OSLD disk as a scintillator.

For OSL the deposition of energy into the crystal promotes valence electrons to the conduction band where the electrons are free to move about the volume of the crystal. These now conduction electrons have a probability of being captured by defects in the crystal which exhibit a lower potential energy. These energy states at the defect sites have such a long lifetime they are considered metastable yet possess a higher energy than the valence band from which the promoted electrons originated. The luminescence is later induced by optical stimulation where the defect trapped electrons are promoted back to the conduction band where they are again free to travel throughout the volume of the crystal. There is a probability these now conduction electrons will combine with the hole left from the earlier x-ray exposure. This capture will result in a luminescent photon which can then be detected.

In TL the energy threshold to allow luminescence is overcome by thermal energy.

The ionizing radiation is understood in a simplified way by one of the following mechanisms: photoelectric effect, Compton scattering, or pair production with the probabilities of each dependent upon the energy of the photon introduced during x-ray exposure.

This process can be simplified into mathematical language to determine some of the processes characteristics. Let p be the probability of a trapped electron to fall into the hole under stimulation and n be the number of electrons trapped in the lattice defects. Then we can mathematically express the rate at which the trapped electrons escape the lattice defects.

$$\frac{dn}{dt} = -np \quad (\text{B.1})$$

Where I have assumed no probability of retrapping and t is the time accumulated time of stimulation.

$$\ln\left(\frac{n}{n_0}\right) = -pt \quad (\text{B.2})$$

The solution to this differential equation indicates an exponential decay of the number of trapped electrons during stimulation.

$$n = n_0 e^{-pt} \quad (\text{B.3})$$

Here n_0 is the number of trapped electrons before stimulation.

The intensity of the luminescence (I) is proportional to the number of the electrons escaping the crystal defects.

$$I = \left| \frac{dn}{dt} \right| = n_0 p e^{-pt} \quad (\text{B.4})$$

Conclusions drawn from these statements can reveal characteristics of the OSL process (reference here). First, the intensity of the luminescence observed and the ionizing radiation exposure of the OSLD are proportional. Next, the dose from ionizing radiation incident on the OSLD can be determined by optical stimulation within a factor of proportionality. Finally, the population of trapped electrons can be depleted by optical stimulation or rather the memory of previous exposures can be eliminated to allow the reuse of the OSLDs.

JLS SHEPHERD *and Associates*

740 Salem Street, Glendale, California 91203 • 213/245-0187

Irradiation & Calibration Equipment • Lead Shielding • Nuclear Applications

CALIBRATION CERTIFICATE

TO: E G & G Idaho, Inc. P.O.# C84225638

SOURCE: 20Ci Cs-137, Amersham Type X60/1 Capsule, S.N. 00090EZ

MOUNTING: J.L. Shepherd & Associates Model 81-8B Irradiator
S.N. 7019

INSTRUMENT: All calibration is done with MDH Industries, Model 2025 X-Ray Monitor, S.N. 2127, with 180cc Probe, S.N. 6105 and 3cc Probe, S.N. 4126. This meter is calibrated by MDH Industries, Inc. using a Model 10X5-6 modified 3-terminal Ion Chamber, S.N. X2, National Bureau of Standards Report #DG 7856/82.

POSITION: Centered in Beam Port

DISTANCE: 100cm 200cm 50cm 30cm

OUTPUT: 7.243R/hr 1.812R/hr 29.147R/hr 83.8R/hr

Dose Rate Symmetry - 15 Centimeters by 15 centimeters field
Centered in Beam Port
1.0 meters source distance
+0% -1.5%

DATE: June 25, 1984


J.L. SHEPHERD

MANUFACTURERS

ENGINEERS

CONSULTANTS

FIGURE B.3: 20 Ci Shepherd source documentation.

B.1.1 Dosimeter preparation

Dosimeters were prepared by exposure to the 20 Ci Cs137 source described by the documentation shown in figure B.3.

Five sets of dosimeters were prepared by bleaching prior metastable electron states

TABLE B.1: Activities of the 20 Ci source based upon the numbers reported by Shepherd and associates.

Dose rate	Distance from source	Calculated activity for June 25, 1984
1.812 R/h	200 cm	21.96 Ci
7.243 R/h	100 cm	21.95 Ci
29.147 R/h	50 cm	22.08 Ci
83.8 R/h	30 cm	22.85 Ci

using exposure to strong white florescent light. Next, dosimeters were mounted on a flat styrofoam board with the cluster of dosimeters centered in the beam path of the source at the predetermined distance and Each set of dosimeters were then exposed to the Cs 137 source. The distance from the source to the calibration dosimeters was maximized ensure minimal variation in exposure delivered to each of the dosimeters within each group.

The dose experienced by each set of dosimeters was calculated.

We begin by calculating the activity (A) of the Cs 137 source.

$$A_0 = \frac{Rd^2}{\Gamma} \quad (\text{B.5})$$

$$A_0 = \frac{(7.243 \text{ R/h})(1 \text{ m})^2}{(0.33 \text{ R/h/Ci})} = 21.95 \text{ Ci}$$

Where I have used R , d , and Γ as the dose rate, distance from the source, and the gamma factor respectively and have calculated the activity of the source on June 25, 1984 from the dose rate measured at a meter.

Next find the activity of the source on the day utilized.

$$A(t) = A_0 e^{-\lambda t} \quad (\text{B.6})$$

$$A(\text{June25, 2017}) = (21.94 \text{ Ci}) e^{-\frac{\ln 2}{(30 \text{ years})}(33 \text{ years})} = 10.24 \text{ Ci}$$

Here $\lambda = \frac{\ln 2}{\tau}$ is the probability of a decay event with τ as the half life and the original activity (A_0) is the activity observed at a meter on June 25, 1984 listed in table B.1.

Now the absorbed dose in air delivered to each set of dosimeters can be calculated.

TABLE B.2: Dosimeter sets prepared for calibration of MicroStar reader.

Dose in air (mrad)	Mean (counts)	Std. deviation (counts)	Confidence value
0	200.078	17.430	0.087
545	9163.961	455.555	0.050
1111	not used	not used	not used
5339	89410.039	3225.494	0.036
169138	218971	9919.742	0.045

$$D = \frac{\Gamma AtC}{d^2} \tag{B.7}$$

$$D_{25 \text{ cm}, 447.157 \text{ min}} = \frac{(0.33 \text{ R/hr/Ci})(10.24 \text{ Ci})(7.452617 \text{ hr})(0.877 \text{ rad/R})}{(0.36 \text{ m})^2} = 169.138 \text{ rad}$$

Where C is the conversion from R to rad in air or in other words the dose delivered to air when 1 R of exposure is applied is 0.877 rad.

B.2 Calibration Procedure

The prepared calibrates are read into the Landauer reader. Ten calibrates from each dose level are read into the reader under the calibration tab of the Landauer Microstar software program. Only three calibrates from each dose level were chosen to calculate the calibration curve due to the manufacturer recommendation that the tolerance on the read calibrates be within X

Some crystal defects give rise to deep centers where the electrons trapped in them cannot be promoted to the conduction band by the stimulating laser for one reason or another, which means the population of available electrons for OSL specific processes is altered when you use the chip repeatedly. This can cause problems with the tolerances by increasing the variance of the response of the chip to larger than the recommended tolerances. (reference here)

Originally eleven calibrates were prepared at each dose level with the hope that a larger sample size would produce and more consistent and accurate result. However, it was discovered that the variation among calibrate sets was too large to satisfy the manufacturers recommended tolerance for the calibration. To bring the tolerances back within the manufacturers specs, it became necessary to use only three calibrates for each dose level. The calibrates were choose by median status (e.g. discarding the four highest and four lowest calibrate readings and including only the three median values from each set).

TABLE B.3: Calibrate readings for validation of the microStar reader.

calibrate	dose (mrad)	calibrate	dose (mrad)	calibrate	dose (mrad)
DA09249197D	8	DA08122877F	599	DA09254184N	1031
	9		577		1032
	9		574		997
	10		571		1022
	10		581		1020
DA08122358P	10	DA08121661X	589	DA09265622K	1014
	10		591		988
	10		583		990
	8		578		1006
	9		580		976
DA08120483W	10	DA09249315L	510	DA08120578L	1161
	9		504		1171
	11		500		1155
	10		497		1132
	9		506		1153

This treatment allowed a calibration curve with calibrate sets that fall within Landauer's allowable variance.

B.3 Validation

For validation 9 calibrates were reserved which were not used for calibration and each of these were read 5 times. The average was taken for all 15 measurements from each dose level and compared to the median value which is expected to fall within 6% [31].

Appendix C

Solid state diode calibration

C.1 Introduction

Using a solid state diode gives another method for measuring the dose delivered. A second method for measuring dose allows the investigator another data point, obtained independently, to substantiate the results of the measurement. The two different methods of measuring the dose allow the investigator to compare the readings and corroborate them. If they do not align properly, this tells the investigator that at least one technology is not performing properly and fix it.

Theoretically the dose measurement from this method is not time integrated over the life of the flash radiography shot and thereby may give information about the function of dose versus time for the shot. Another reason why solid state diode measurements are desirable is that the handling of the raw data from the diode can be automated and thereby yields the result of the data more quickly than OSL or TLD measurements. The signal from the diode goes directly to an oscilloscope and into the server where the data is kept. A macro can be written to apply data processing and calibration factors and have the dose reading virtually instantly.

A solid state diode is a sandwich device that results in a depletion region that prevents the flow of current. When exposed to ionizing radiation, the resultant electrons in the depletion region allow the conveyance of charge across the depletion region and result in a signal of current which is measured as the response of the diode to exposure.

C.2 Method

The calibration is specific to the location of the diode relative to the source. The diode is placed in a location that can be maintained for the series of shots without impeding what is being tested by the shot series. What is being tested in a shot series will dictate where the diode is placed. There is an art to the placement. The diode signal is fed into an oscilloscope as a voltage, so one wants to resolve the voltage, which means the scope is set to a certain scale. But if for some reason the shot is stronger than expected it will put the voltage over the scale the scope is set to handle. On the other hand, if the scale of the scope is set too low then the appropriate resolution cannot be captured for the signal, thereby losing information. Therefore an educated balancing act is needed to set

the distance between the source and the diode commensurate to the scale of the voltage setting in the scope.

C.3 Signal Processing

The signal from the diode is processed by first subtracting the baseline of the signal then eliminating the effects of the time decay. Every system has a decay and the time constant of that decay depends on the characteristics of the system. One determines the time constant of the system by sending a pulse through the system and measuring the decay rate of the signal after it has passed through the system. Then one takes that time constant and processes the signal (as described following) to subtract out the decay introduced in the signal by the effects of the system (e.g. the cable that connects the diode to the scope, the way the diode is biased so that the electrons that appear in the depletion region will sweep across the region to work) to find the native signal from the diode itself. Finally the area under the curve of the voltage signal will be proportional to the dose delivered to the depletion region. So the voltage signal simply needs to be integrated and multiplied by the calibration factor to resolve the dose at the diode. These calculations are performed through a macro written in the Stella software (see Appendix D).

To calibrate the diode, the diode is set up at the predetermined location with an alternate instrument to measure the dose at the location of the diode (OSL, film stick, TLD, etc.). Then the pair is exposed (the diode and the alternate instrument), the baseline subtracted from the diode signal, effects of electrical decay are removed, and the signal is integrated. Then the alternate instrument measurement of dose is read, this number is divided by the result of the integral and the calibration factor is generated. Then provided the diode is placed in the same location relative to the source, the dose at the diode can be known by processing the diode signal and applying the calibration factor.

Appendix D

Stella

D.1 Introduction

Stella can configure and operate devices for data acquisition, including oscilloscopes and other remote computer systems by methods which include but are not limited to GPIB, Enet, and USB interfacing. It archives data and allows organization, annotation, visualization, and conversion of data files. It includes data processing of scalar, waveform, matrix, and image data formats. Analysis operations include arithmetic, fast Fourier transforms, curve fitting, filtering, and image transformations [32].

D.2 Motivation

Stella allows the management of data acquisition devices, data archiving, data analysis, and visualization all in one piece of software. Specifically Stella allows the user to remotely set a scope and configure the scope (including trigger, voltage scaling, time scaling, trigger placement in time domain) and set these settings in all the other channels solely from user interface with Stella software. All scopes and all channels in the whole system can be set back to their original configuration with a single click in the Stella interface allowing the user to ensure consistent initial set up of the scopes for every shot. Not all scopes are supported in Stella software. One can "trick" Stella into acquiring data from an unsupported scope, but some features (in particular setting a scope remotely with Stella) do not work with unsupported scopes. In the current TriMeV data acquisition system the scopes are unsupported and therefore cannot be managed remotely via Stella. While the current system does enable all the functionality of the software, Stella still provides utility in that it can acquire and archive data, allow data processing and analysis, and visualization of multiple data forms for the system in one software package.

D.3 Installation notes

For Windows: 1. Obtain the .zip file from Sandia National Laboratory (see David Hinshelwood). 2. Extract the file, this should result in the creation of a program file

typically at C:/users/username/appdata/local/Stella on Windows systems. It will also generate a data file location typically at C:/user/username/documents/experiments.

D.4 Macros

Stella provides an environment in which macros can be written. Macros allow a user to program multiple functions into one executable configuration. This way users can program repetitive tasks that involve multiple analysis steps into one program that can be executed with one click. For instance, one can write a macro that will take the silicon diode signal, baseline the signal (subtract the effects of the time dependent decay), integrate the result, and apply a calibration factor (as done for the solid state diode dose reading described in Appendix C). This creates efficiency because the user doesn't have to manage each individual step and results can be seen more quickly. Where all the steps are automated the possibility of user error is reduced. Macros also provide a way for common processes of multiple operations to be documented and repeated without variation by other users.

Appendix E

BAS 1800 II

E.1 Introduction

The BAS 1800 II scanner consists of conveyor belt that moves the phosphor screen in one direction, and stimulating laser that rasters perpendicular to the motion of the screen, and a wave guide with accessories needed to acquire and process the signal. The scanner stimulates the crystals in the phosphor screen and photons are released commensurate with the exposure in each particular location.

E.2 Installation notes

The system used was installed on a computer equipped with an Intel Celeron CPU (2.6 GHz and 1.0 GB RAM) running Windows XP Professional, Version 2002, Service pack 3. An Adaptec AHA-2940AU SCSI card was installed to enable interface with the scanner.

E.3 Operation notes

In its current state the scanner does not pass its self check during the power up sequence. Through experimentation it was found that the signal voltage to a solenoid that controlled a baffle to the scanning laser beam did not have adequate voltage to actuate the baffle and allow the laser to scan the phosphor screen. The cause of this discrepant voltage was not identified but would be key to restoring the scanner to its original operational procedure. Because the source of the voltage discrepancy was not identified the system requires procedures¹ that deviate from the methods documented in the BAS-1800II user manual[33] to ensure the capture of an image from the phosphor screen.

E.3.1 Procedural description for BAS-1800 II scanner

1. With the scanner powered off and the ambient lights dimmed, open the main cover of the scanner, disengage solenoid 1 and replace the cover as shown in figure E.1¹.

¹This is an "off label" procedure in that it deviates from the methods outlined in the BAS-1800II user manual.

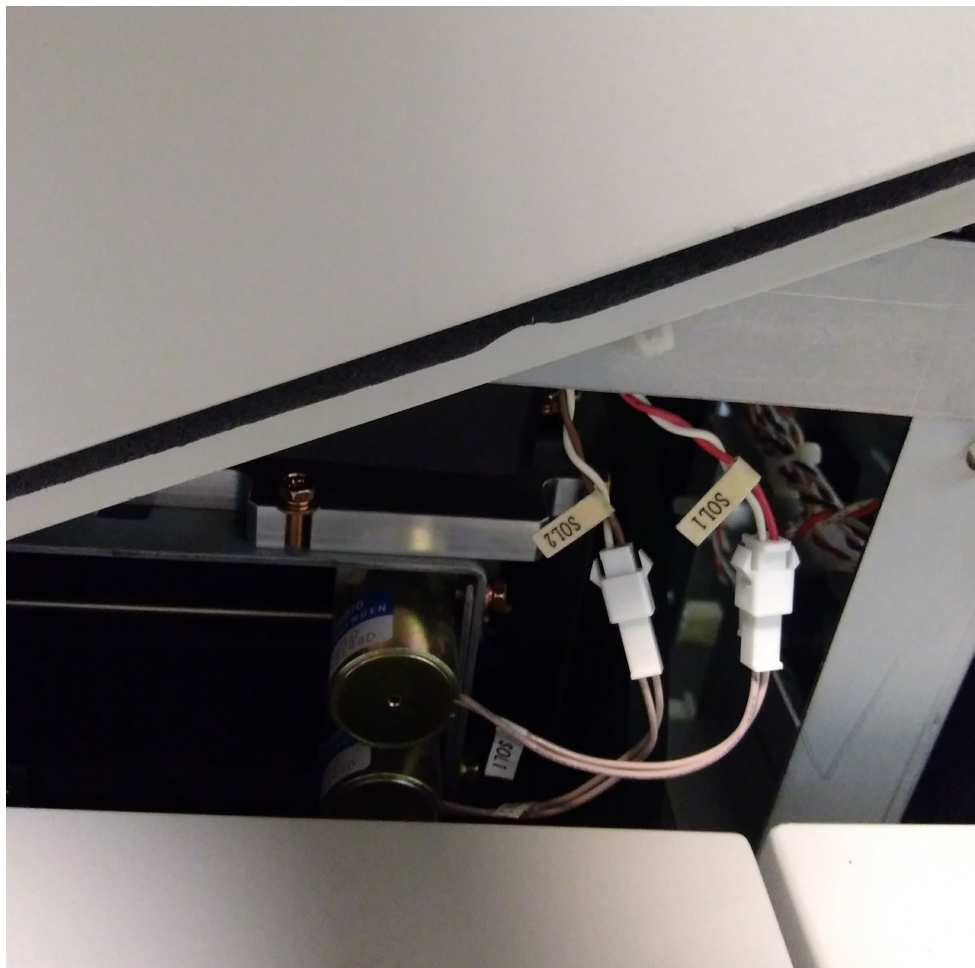


FIGURE E.1: Lifted lid of the BAS-1800II image plate reader exposing the solenoids that actuate the stimulation laser baffle.

Important: Proceed with the needed precautions to guard against laser beam exposure and possible high voltage conditions present inside the scanner. Even with the scanner off high voltage conditions may persist inside the scanner.

2. Power on the image reader.
3. Restart the computer.
4. Log onto the computer.
5. Launch the Image Reader BAS-1800II V1.8 software.

Browse to the start up menu for the FujiFilm folder and click the Image Reader BAS-1800II.

After initialization you will find the control console displayed in figure E.2.

6. Configure the scan.

Specify each of the settings for the desired scan.

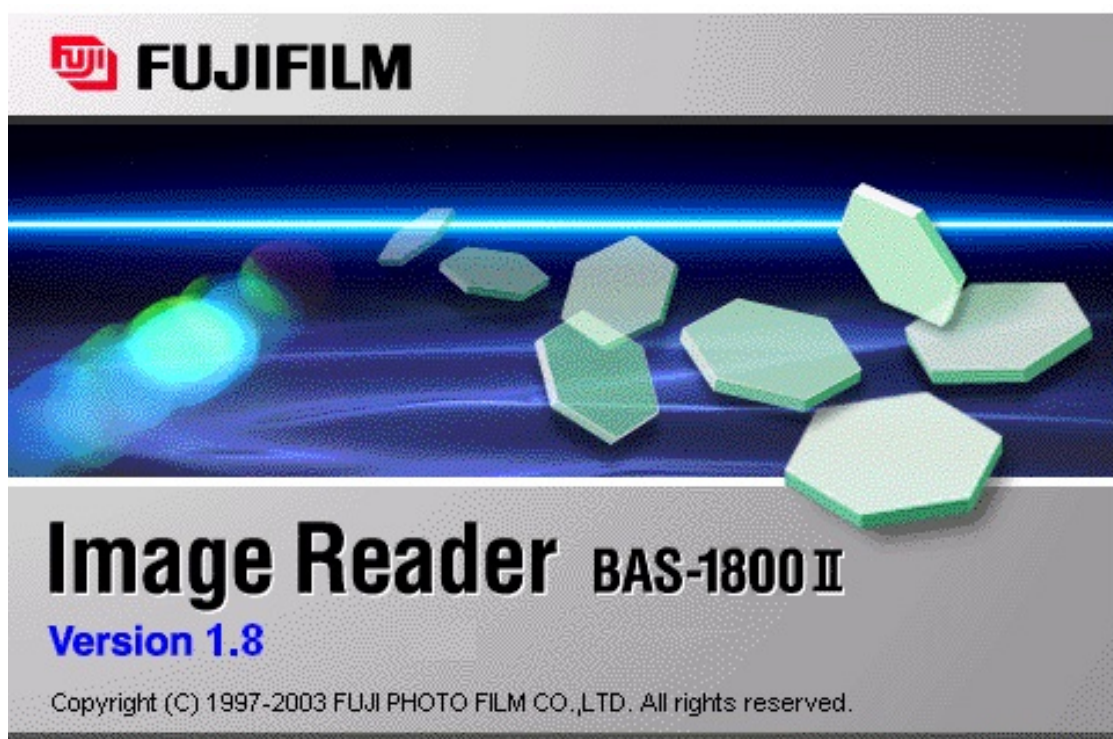


FIGURE E.2: Splash screen for Image Reader software.

- File Name: Enter the name you like for your image file.
 - Comment:
 - Gradation:
 - Resolution:
 - Latitude:
 - Sensitivity:
 - Sampling Area:
 - Selected Size:
 - File Size:
7. Lift the main cover and re-engage solenoid 1¹.
- Important: Again, precautions must be taken to guard against laser beam exposure and possible high voltage conditions present inside the scanner.
8. Place the plate in the scanner. The photosensitive (white) side must be facing up with the angled corner should be in the upper left. The pressure sensor and the lid closure sensor must both be triggered before the system will allow a scan to be initiated.

Appendix F

Denoptix

F.1 Introduction

Literature suggests the resolution of the Denoptix QST phosphor screen system is limited to 7 lines/mm [34] which equates to a resolution of 0.14 mm.

F.2 Installation notes

The scanner system was operated using a Dell N5050 running Windows 7 Home Premium edition. Which is a 64-bit operating system with 6 GB of RAM and an Intel Core i3-2370M CPU at 2.4 GHz

To install the Denoptix scanner system the GxPicture 3.1.1 software must be downloaded from the Gendex website (see <http://www.gendex.com/software-drivers>). Installation of this software will fail since the Gendex prerequisite software has not yet been installed but in the process of attempting to install GxPicture 3.1.1 the GxTwain driver will be installed. With the GxTwain driver Stella can temporarily be used to acquire the images from the phosphor plate scanner.

F.3 Operational notes

To acquire an image follow these steps.

- Interface the computer and the scanner with the USB cable.
- Ensure the scanner is powered on.
- Under dimmed lighting conditions transfer the exposed phosphor screen to the carousel and install it on the spindle of the scanner. Note the carousel door to the scanner will only open when prompted by the connected computer but the latch is easily opened by pushing back the tapered latch tip. This is done by inserting a stiff card (credit card) into the gap between the frame of the scanner and the door near the latch and sliding the card into the tapered latch tip. While the card is holding back the latch simply lift the lid of the scanner. Note also that care

must be taken to ensure the correct carousel settings and the correct seating of the clips when using the cephalographic phosphor plate. Incorrect setting of the carousel counterbalance will result in an imbalanced carousel while it spins and if the phosphor screen clips are not tightly seated the phosphor plate can come loose and damage the phosphor screen.

- Open an instance of Stella.
- From the tools pull down menu select Twain select and choose the GxTwain driver as the source.
- From the tools pull down menu select Twain acquire which will open a GUI interface window which will allow the configuration of the scanner and acquisition of the radiographic image.